UNIVERSIDAD
NACIONAL
DE COLOMBIA

Analysis of the Kelvin-Helmholtz instability in seagrass-oscillatory flow interaction

Alejandro Cáceres Euse

Universidad Nacional de Colombia Faculty of Mines,
Departament of Geoscience and Environment
Medellín, Colombia
2019

Analysis of the Kelvin-Helmholtz instability in seagrass-oscillatory flow interaction

Alejandro Cáceres Euse

A dissertation submitted in partial satisfaction of the:
Doctorate in Marine Science

Advisor:
(Ph.D.) Francisco Mauricio Toro Botero

Co-Advisor:
(Ph.D.) Alejandro Orfila Foster

Universidad Nacional de Colombia Faculty of Mines,
Departament of Geoscience and Environment
Medellín, Colombia
2019

To my wonderful mother, I won't be able to give you back all the love, sacrifice, time, support and patient from the day I was born until this day. Thank you Mami, I hope you feel as proud of me as I am of you. Also to my brother, because you are the strongest man I know.

Contents

List of Figures

List of Tables

Acknowledgments

I am indebted to Universidad Nacional de Colombia, such a great institution. Since I was an undergraduate student, La NACHO was the place that let me find all the answer to my questions. I hope I can contribute in the future to the new generations like my professors made it with me.

Many thanks to my partners and professors from El PARH, the Ocenánicos research group and all the people who contributed from the beginning to my process, when I was introduced to the "*passion for waves*". I am going to list a few group of people who shared their dreams and helped me to get better day by day; however, the list is so big that I could spend all the pages just on that. To them, I'm so sorry. Thank you Eli, Lafurcade, Richy, Guerrero, Uran, Sebas, Carlos, Coy, ML, Alejo H, Eileen, El negro, El chupi, Juan O., Luna, Lination, Maria, Alex and Diana, your love, the good and bad moments that We shared together let me see you guys as brothers that I chose.

I want to thank to the scholarship 647 from COLCIENCIAS, Universidad Nacional de Colombia - Medellín campus and the University of California - Berkeley for the huge help providing the infrastructure to develop this thesis. The Prof. Philip L.-F. Liu and Prof. Shih-Chun Hsiao who provided the experimental data used in the second chapter of this research; additionally, special thanks to Lily Cohen and Bianca Acosta for the valuable assistance in the experimental work to validate the developed model in chapter 3, and the professor Marco Ghisalberti who provided the experimental data used in chapter 4.

Special thanks to professor Evan Variano from UC Berkeley. He generously shared his many and considerable talents and unconditional support that was so valuable for me during my PhD process.

Finally, thanks to Alejandro Orfila and Andrés Osorio for all the support and help; and specially to professor Mauricio Toro, my mentor since I started this scientific path.

Chapter 1

Introduction

1.1 Introduction

The aquatic vegetation is ubiquitous worldwide, from low temperature areas to tropical shallow coastal zones (Van Der Heide et al., 2007). These ecosystems provide a productive life cyle being the habitat for many marine animal species (Marion et al., 2014).

At the coastal region, the aquatic vegetation (seagrass) attenuates the currents, dissipates the wave height and stabilises the coastlines (Maxwell et al., 2017; Pinsky et al., 2013) being considered as a soft system to reduce the risk of flooding and erosion under sea level rise and extreme wave events (Ondiviela et al., 2014). Based on the above described services, estimations of economical annual values provided by the aquatic vegetations is over $10 trillion (Nepf, 2013).

Control field studies such as those by Schanz et al. (2002); Schanz and Asmus (2003) demonstrate the interdependence between the hydrodynamic and biological processes, since there is a cascading effect in which for a specific flow conditions, different species can live and proliferate within the seagrass meadows or be washed away, depending on the energetic wave conditions and seagrass density.

Regarding the interaction between the submerged seagrass and the surrounding flow, it is well known that the presence of the seagrass canopies attenuate the momentum by the work done on the flow by the stems (Finnigan, 2000). The effects in the velocity field can be differentiated and thus studied in terms of scales; 1) processes with spatial scales of the order of the stem diameter or spacing between stems; and 2) processes with scales of the order of the drag length scale. The turbulent structures at the scale of the stems are called wake scales and are produced by the shadow zone downstream the stems (Nepf, 2012; Zhang et al., 2018). Turbulent processes at the drag length scale are governed by the density of the canopy and the flow dynamics (Nepf, 2012). These processes modulate the water renewal between the water inside and above the canopy and the amount of suspended sediments along the water column (Luhar and Nepf, 2013).

The turbulent processes at the drag length scale can be analysed as a plane mixing layer by two co-flowing streams that present a shear layer at the top of the canopy (Raupach et al., 1996). This shear-layer-flow is characterized by an inflexion point in the velocity profile (two water bodies moving at different velocities), responsible for the vertical mass exchange at the top of the canopy (Ghisalberti and Nepf, 2009). The shear layer facilitates the generation of Kelvin-Helmholtz instability type vortex (Ghisalberti and Nepf, 2002).

The Kelvin-Helmholtz type vortex has been widely studied in steady flows (Raupach et al., 1996; Finnigan, 2000; Ghisalberti and Nepf, 2002; Nepf, 2012; Mandel et al., 2017), characterizing its effect on the seagrass movement, the Reynolds stresses, the sediment distribution, the vertical mixing and the free surface. However, the formation and effect of Kelvin-Helmholtz type vortices in the wave oscillatory flow is still far to be completly understood. Indeed, it is still not clear which are the dominant terms in the Navier-Stokes equations for the oscillatory-seagrass-flow interaction. Ghisalberti and Schlosser (2013) reported some "'necessary" conditions in the flow in order to produce Kelvin-Helmholtz instabilities; Abdolahpour et al. (2017) analysed a steady current released by the presence of the shear layer and its relation with the shear layer magnitude and Abdolahpour et al. (2018) used the seagrass-steady-flow interaction formulation of Ghisalberti and Nepf (2002) to estimate the Kelvin-Helmholtz frequency range in oscillatory flows.

The evolution of vortices downstream submerged structures in oscillatory dominant flows is assumed to be dissipated by the viscosity and the effects on the wave breaking process have not been yet analysed. Indeed, a theoretical model to solve the Kelvin-Helmholtz instability modes as a function of the free surface and a general characterization of the turbulent spectra is an open question that will provide new insights in order to improve models and simulations of relevant hydrodynamic processes at coastal scale.

The aim of this Thesis is to understand the relation between the free surface frequency and the Kelvin-Helmtholtz instability modes in seagrass-oscillatory-flow interaction. For this, I will first analyze the effects of a vortex by an isolated submerged stem interacting with a surface wave. Then, I develop an analytical model to determine the dominant terms in the momentum equation in seagrass-oscillatory-flow interaction. Finally I close the scientific question by solving the Kelvin-Helmholtz instability modes in seagrass-oscillatory flow interaction as a function of the free surface wave applying the Piecewise method to a simplified velocity profile.

This thesis is structured as follows. Chapter 2 analyses the effects of backwards wave breaking process induced by a strong transport of mass in a vortex produced by an isolated submerged stem. In chapter 3, a simplified seagrass-oscillatory-flow model is developed by dimensional analysis of the Navier-Stokes equation. Here, some reference variables are defined according to the free surface wave parameters . The vali-

dation of the simplified model is performed against experimental data from a flap type wavemaker system and a random seagrass distribution. Finally, chapter 4 presents a theoretical model for the Kelvin-Helmholtz instability modes as a function of the incoming free surface wave. The model applies the piecewise linear method to the Rayleigh's equation in an ideliazed vertical velocity profile.

It is important to remark that this thesis is composed by three papers: Chapter 2 has been published in the *Ocean Engineering Journal*, Chapter 3 is in final revision for the *Experiments in Fluids Journal* and Chapter 4 is under review for the *Journal of Fluid Mechanics*.

Chapter 2

Vortex formation in wave-submerged structure interaction

Abstract

Long wave-structure interaction is studied numerically. The Rayleigh and Goring wave generation theories with a solitary wave with two nonlinearity factors and three discretization schemes for the advective terms for the wave propagation are evaluated. Results show good agreement for the main wave peak and for the wave decay rate. The model captures the trailing waves and some differences on the wave decay rates are observed.

Analysis of monochromatic and solitary wave cases passing over submerged structure is then studied. For the monochromatic scenario, the model agrees very well with the free surface experimental data, and a "Linear fluid structure interaction mechanism" can be observed based on the structure geometry and the absence of adverse pressure gradient in the flow. For the solitary wave case interacting with a slender column, the numerical model agrees very well with the measurements, showing that an adverse pressure gradient in the flow is presented and the vortex in the flow induces a wave breaking process, not by the bottom friction, nor by water depth reduction but by a strong transport of mass from upstream to downstream side of the vortex; this turbulent structure is the dominant process, even when the wave breaking is present.

2.1 Introduction

Understanding wave propagation and its interaction with submerged structures is crucial when studying hydrodynamic processes, specially in coastal areas where the large interaction occurs between man-made or natural structures and the sea. In this area, there are three main topics of research: a) the wave transformation along the submerged structure, b) vortex generation by adverse pressure gradient and c) the wave breaking due to a water depth reduction on the submerged structure. The physical processes present in wave-submerged structure interactions are: reflection, transmission and dissipation of the incident wave Losada et al. (1996); Christou et al. (2008); Zhou et al. (2014).

Regarding the physical wave processes along the submerged structure (with no breaking due to bottom effects), two main phenomena are present: a) the generation of higher harmonics from the incident wave frequency by the increment on the wave non-linearity when the wave is over the obstacle (Grue, 1992; Huang and Dong, 1999) and b) the vortex formation in the flow at the upstream and downstream side of the structure, if the structure geometry and wave properties satisfy some specific conditions, producing the crest-crest exchange and backward wave breaking (Cooker et al., 1990). These complex flow behaviour (vortex formation) have been the focus of different works on the last decades, because of the inclusion of viscous stresses in the hydrodynamic flow solutions, finding that these flow modifications or secondary flows can strongly modify the wave free surface profile, wave loads and structure stability (Huang and Dong, 1999; Chang et al., 2005; Wu et al., 2012). Nevertheless, the entire vortex evolution on a wave environment and its effect on the backward wave breaking process is still not completely understood.

Related to the wave scenarios, the solitary waves have been frequently employed for decades to determine the characteristics of tsunamis and strong surges (Zhang et al., 2012) or to describe waves in the surf zone (Dean and Dalrymple, 1991); additionally, the study of solitary wave transformation around marine breakwaters is a critical problem when evaluating the effects produced by these extreme waves in coastal areas (Wu et al., 2012). Also, for monochromatic waves, different authors study the wave transformation and its dissipation when an immersed obstacle is presented (Iwata et al., 1996; Kawasaki and Iwata, 1998; Dong and Huang, 2001; Shen and Chan, 2008; Higuera et al., 2013; Chen et al., 2014).

Concerning the use of CFD tools for wave generation and propagation and the understanding of different physical processes in wave-structure interaction scenarios, those who solve the Navier-Stokes equations are the most appropriate, due to the inclusion of viscosity effects in the wave field (Iwata et al., 1996; Huang and Dong, 1999; Lin and Liu, 1999; Chang et al., 2001; Shen and Chan, 2008). The usual approach for wave generation, since it presents the lower computational cost, uses a fixed mesh for the whole computational domain, generating waves either by using the mass conserva-

tion equation a in specific region known as the mass source or source region (Ohyama and Nadaoka, 1991; Iwata et al., 1996; Kawasaki and Iwata, 1998; Lin and Liu, 1999; Lara et al., 2006; Chen and Hsiao, 2016) or by specifying the free surface, on an open boundary, according to the desired wave characteristics and advecting them using the wave equations (Amini Afshar, 2010; Lambert, 2012; Jacobsen et al., 2012; Higuera et al., 2013; Chen et al., 2014). All these method applied a relaxation or sponge-like layer zone in the computational domain, in order to avoid unwanted reflected waves by open boundaries or internally in the computational domain (Lara et al., 2006; Jacobsen et al., 2012; Chen and Hsiao, 2016). However, wave generation in fixed meshes presents limitations, since implicit signals produced in laboratory are not recreated. In particular, the trailing waves as the result of the wave theory used in the solitary wave generation paddle movement is not simulated by these models, inducing higher uncertainties since the differences between the model and the experimental data are the result of the wave boundary conditions. A second approach for the wave generation is the use of dynamical computational mesh whose displacement is obtained by the solution of a specific equation at the boundary, describing the wave generator movement (Dong and Huang, 2001; Oliveira et al., 2009; Elangovan and Sahoo, 2010; Xi-zeng et al., 2010; Wu et al., 2014; Higuera et al., 2015).

In the present work, the dynamic mesh approach is used following the piston-type wave generator concept, in order to include the trailing waves in the wave propagation. For the solution of the dynamic mesh generation problem, the library `dynamicInkJetFvMesh` (Weller et al., 1998; Jasak and Tukovic, 2006) is used and the wave generation theory is applied as a modulating function. For the wave propagation, the discretization scheme for the advective terms in the momentum equation (Jasak et al., 1999; Ferziger and Peric, 2002) is evaluated; minimizing the numerical damping and the wave decay along the flume.

This paper is structured as follows. First, the dynamic mesh description and the long wave and monochromatic wave generation theories are presented followed by the modulating function for the wave governing equations at the moving boundary. Secondly, a detailed analysis of the numerical discretization of the advective terms in the transport equation is described; and the numerical solution studied for the slip and non slip boundary conditions. Finally the model is validated and used to describe two wave-structure interaction scenarios.

2.2 Methodology

In this section, a review of the wave generation and propagation theories is briefly summarized. The piston-type wave generator concept is described using the governing equations for a variable volume domain (Jasak, 2009); then, several discretization schemes are tested to accurately solve the advective terms in the Navier-Stokes equa-

tions (Jasak et al., 1999).

2.2.1 Dynamic Mesh

In dynamic mesh computations, two motions can be distinguished: the motions at the boundary and the motions in the interior of the domain. Motions at the boundary are specified by a given governing equation representing the boundary displacement while the interior points have to accommodate to the prescribed boundary motion preserving the mesh validity and quality. By following this procedure, errors in the results can be only assigned to the mesh discretization (Jasak and Tukovic, 2010).

The moving mesh in the finite volume discretization is based on the integral form of the mass conservation law over an arbitrary moving volume V, bounded by a closed surface, M. For a general tensor property ψ, the following equation has to be satisfied (Jasak and Tukovic, 2010)

$$\frac{\partial}{\partial t}\int_V \rho\psi dV + \oint_M \rho\vec{n}\cdot(\vec{v}-\vec{v_M})\psi dM - \oint_M \rho\gamma_\psi(\vec{n}\cdot\bigtriangledown\psi dM) = \int_V M_\psi dV \tag{2.1}$$

where ρ is the fluid density, $\vec{n}$ is a unit normal vector to the surface M, $\vec{v}$ is the fluid velocity, $\vec{v_M}$ is velocity at the boundary, γ_ψ is a diffusive coefficient and M_ψ is a source term. Now, the relationship between the change of volume and the boundary velocity is defined by the space conservation law,

$$\frac{\partial}{\partial t}\int_V dV + \oint_M \vec{n}\cdot(\vec{v_M})dM = 0 \tag{2.2}$$

In this work, Equations (2.1) and (2.2) are part of the CFD solver and the wave generator is a modification of the native equation in the dynamic mesh movement directory (`interDyMFOAM`) of OpenFOAM©.

This solver considers an incompressible, transient, newtonian fluid in a two phase flow together with the dynamic mesh algorithm with no topological changes in the mesh (Greenshields, 2015). The pseudo-algorithm presented here uses the `dynamicInkJetFvMesh` library solver to simulate dynamic mesh phenomena, where the mesh behaviour is represented as a linear spring and is part of the different solvers available for non-topological dynamic mesh changes using an explicit equation. This library allows the definition of a dynamic and fixed regions by using a pivot at a specified location on the domain, so the dynamic region is used for the wave generation (wave Generation zone) and the fixed one for wave propagation and wave-structure interaction (wave Propagation Zone). The utility of the fixed or static region in the numerical wave flume, permits to study wave interacting with any kind of fixed structures without inducing cell deformations in the structures by the mesh movement (see Fig. 4.1).

2.2.2 Wave maker theory

The challenge in the generation of solitary waves in wave flumes is to minimize the spurious waves generated after the main wave that degrades the target wave (Goring and Raichlen, 1980; Katell and Eric, 2002; Wu et al., 2014). For monochromatic waves, the objective is to obtain the desired wave height and period for a specific depth (Frigaard et al., 1993).

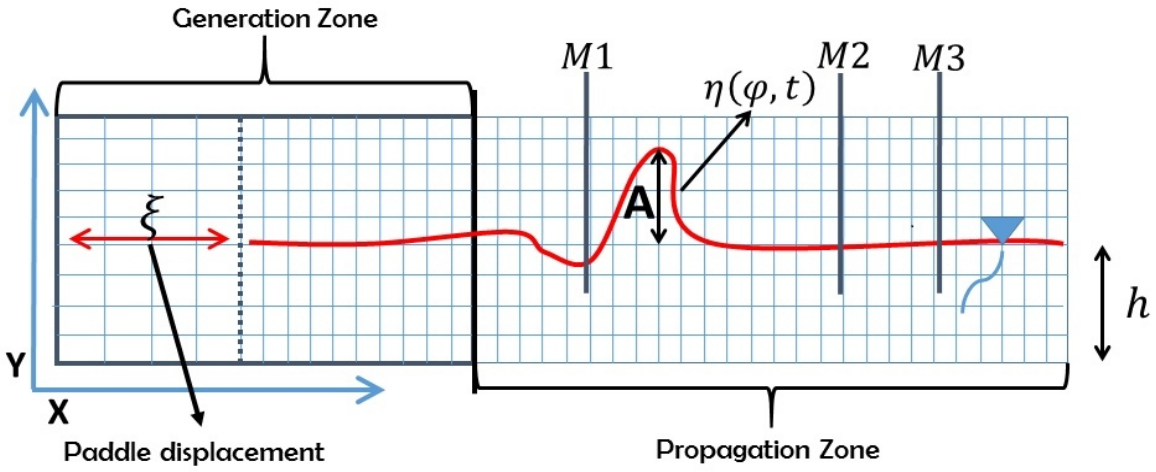

Figure 2.1: Wave generation scheme and paddle displacement with mesh adjustment. M1 is at 6.5, M2 at 9 and M3 at 11.5 meters from the paddle.

Long Wave Generation

For long waves, a transfer function relates the horizontal velocity of the wave generator with the vertical average of the horizontal velocity component, $\bar{u}$ as (see Fig 4.1),

$$\frac{d\xi}{dt} = \bar{u}(\xi, t) = \frac{c\eta(\xi, t)}{h + \eta(\xi, t)} \tag{2.3}$$

where c is the wave celerity and η the free surface. The left hand side (LHS) of Equation (2.3) represents the speed of the moving paddle and the right hand side (RHS) represents the depth integrated horizontal velocity. If η has the shape of any harmonic function for the paddle position, $\xi(t)$, Equation (2.3) implies:

$$\eta(\xi, t) = Af[k(ct - \xi(t))] \tag{2.4}$$

where k is the wave number. By defining $\varphi = k(ct - \xi)$ for a solitary wave, Equation (2.4) can be expressed as (Katell and Eric, 2002):

$$\eta(\xi, t) = A \operatorname{sech}^2\left(\frac{\beta\varphi}{2}\right), \tag{2.5}$$

$$\xi(t) = \frac{2A}{h\beta} \tanh\left(\frac{\beta\varphi}{2}\right) \tag{2.6}$$

where A is the amplitude of the solitary wave, h the still water depth, β is a decay coefficient, $S = (4A)/(h\beta)$ is the stroke of the paddle and the duration of the stroke is,

$$\tau = (4/\beta c)\left[\operatorname{arctanh}(0.999) + A/h\right]$$

Two different approximations for the solitary wave generator have been implemented: the solution of the Boussinesq equation presented by Goring and Raichlen (1980) and the solution of the Rayleigh equation presented by Katell and Eric (2002). Hereinafter, the sub-index G will denote the Goring and Raichlen constant and the R the Rayleigh constant.

Goring and Raichlen approximation Based on the simplified solution of the Boussinesq equation with $\bar{u}(\xi, t) = \bar{u}(0, t)$, Equation (2.6) can be expressed as (Katell and Eric, 2002):

$$\xi(t) = S_G \tanh\left[\left(\sqrt{\frac{3A}{4h^3}}\right)\varphi\right] \tag{2.7}$$

with $S_G = 4\sqrt{Ah/3}$.

Rayleigh Approximation In the Rayleigh approximation, the position of the paddle can be expressed as (Katell and Eric, 2002),

$$\xi(t) = S_R \frac{h \tanh(\beta_R c_R t/2)}{h + A[1 - \tanh^2(\beta_R c_R t/2)]} \tag{2.8}$$

with $S_R = 4\sqrt{A(A+h)/3}$. Since the stroke of the paddle defined by Equations (2.7) and (2.8) represents the displacements from -S_G to +S_G (or from -S_R to +S_R), a translation is applied to transform it from 0 to +2S_G (or from 0 to +2S_R) to prevent convergence problems of the numerical solution due to the rapid change of the boundary as well as to guarantee the reduction of the simulation time.

Wave Train Generation

The wave train generation uses the `Biésel Function`, which relates the wave amplitude with the paddle displacement (Frigaard et al., 1993). This procedure starts from

the mass conservation equation and a harmonic boundary condition that mimics the wavemaker. The wave hight-stroke relation (H/S) is a mathematical expression for the monochromatic wave generation, see Equation (2.9), and the expression for the paddle displacement, including the effect of the second order terms, is given by Equation (2.10):

$$\frac{H}{S} = \frac{4\sinh^2(kh)}{\sinh(2kh) + 2kh} = m_1 \tag{2.9}$$

$$\xi(t) = \frac{H\sin(wt))}{2m_1} + \frac{H^2}{32\left(1 - \frac{h}{2(h+L)}\right)}\left(\frac{3\cosh(kh)}{\sinh^3(kh)} - \frac{2}{m_1}\right)\sin(2wt) \tag{2.10}$$

where m_1 is the first order wave hight-stroke relation, w is the angular frequency and L is the wavelength of the desired wave satisfying the dispersion relation. This formula is valid for Ursel number up to 26.32 (Steven A., 1993).

2.3 Mesh Behavior

In the dynamic grid approach, we need to define three regions: i) the displacement area for the wave generator, ii) the region where the computational cell faces move proportional to the distance to the moving boundary (spring type region) and iii) a fixed or static sub-domain, where the wave propagation and wave-structure interactions will be studied. To do so, an equation emulating a linear spring is defined in the generation zone (see Fig 4.1). The equation resulting for the grid that satisfies the above conditions is Equation (2.11) (Jasak, 2009):

$$X_{new} = X_{old} \cdot (1 + position\,(-X_{old} - ref) \cdot SCF) \tag{2.11}$$

where X_{new} is the position of the cell faces at a given time, including the boundary; X_{old} is the position of the cell faces at a previous time; ref is the pivot location where the dynamic and fixed regions match each other and SCF is a function that modulates the boundary displacement corresponding, in our case, to the solitary or monochromatic wave generation functions previously defined. The objective for the wave generation is to apply the native OpenFOAM© equation (Equation (2.11)) for wave propagation modifying the modulating function by the wavemaker theory. This is achieved using a pivot position according to wave generation and combining a dynamic region for the wave
generation with a fixed region for wave propagation in order to mimics wave-fixed structure interaction scenarios.

Special care is taken in the wave propagation zone (see Fig 4.1) where a static grid is defined since the grid resolution changes and some problems related to numerical diffusion can arise in the limit between the generation and propagation zones. To overcome this issue, we defined the cell size in the static zone to be the same as the

neighbouring cells when the SCF parameter is maximum.

Regarding the vertical direction, the cell discretization ratio, $\Delta x/\Delta y$, must have a moderate value, which is related to the wave steepness as:

$$\frac{\Delta x}{\Delta y} \backsim 2 \tag{2.12}$$

$$\frac{\Delta y}{\Delta x} = \frac{H}{L}; \qquad \Delta y = \frac{H}{n} \tag{2.13}$$

where n is the number of cell divisions of the wave height.

2.3.1 Governing equations

Wave propagation is computed by solving the Navier-Stokes equations for an incompressible fluid in a Cartesian coordinate system

$$\nabla \cdot \vec{U} = 0 \tag{2.14}$$

$$\frac{\partial(\vec{U})}{\partial t} + (\vec{U} \cdot \nabla)\vec{U} = -\frac{\nabla P}{\rho} + \nu\nabla^2\vec{U} + \vec{g} + \frac{1}{\rho}\vec{F}_s \tag{2.15}$$

where ρ is the fluid density, $\vec{g}$ is acceleration due to gravity, ν the kinematic viscosity, $\vec{U}$ the velocity field, P the dynamic pressure and $\vec{F}_s$ is a vector force due to surface tension. To resolve the location of the free surface, the volume of fluid (VOF) technique uses a transport equation for the fraction of the liquid volume γ (Hirt and Nichols, 1981):

$$\frac{\partial\gamma}{\partial t} + \bigtriangledown \cdot \left(\gamma\vec{U}\right) + \bigtriangledown \cdot \left(\gamma\left(1-\gamma\right)\vec{U}_r\right) = 0 \tag{2.16}$$

where γ is the liquid fraction and $\vec{U}_r$ is an artificial velocity factor that allows a correction of the velocity of the water and air near their interface (Higuera et al., 2013). The surface term and the properties of the fluids are defined below, where σ is the Surface tension and $\vec{n}$ its curvature:

$$\gamma = \begin{cases} \gamma = 0 & \text{for} \quad \text{air} \\ \gamma = 1 & \text{for} \quad \text{water} \\ 0 < \gamma < 1 & \text{for} \quad \text{free surface} \end{cases} \tag{2.17}$$

$$F_s = \sigma\vec{n} \tag{2.18}$$

$$\vec{n} = \frac{\bigtriangledown\gamma}{|\bigtriangledown\gamma|} \tag{2.19}$$

$$\rho = \gamma\rho_{water} + (1-\gamma)\rho_{air} \tag{2.20}$$

$$\mu = \gamma\mu_{water} + (1-\gamma)\mu_{air} \tag{2.21}$$

Equations (2.14) to (2.21) are solved numerically using `interDyMFOAM` in the finite volume (FV) approximation transforming the above set of partial differential equations in a set of integral equations over a differential control volume (CV). The total computational domain is arranged in a computational mesh conformed by small CVs computing the velocity field and the scalar variables at the center of the cell (Ferziger and Peric, 2002), as shown in Fig 4.2.

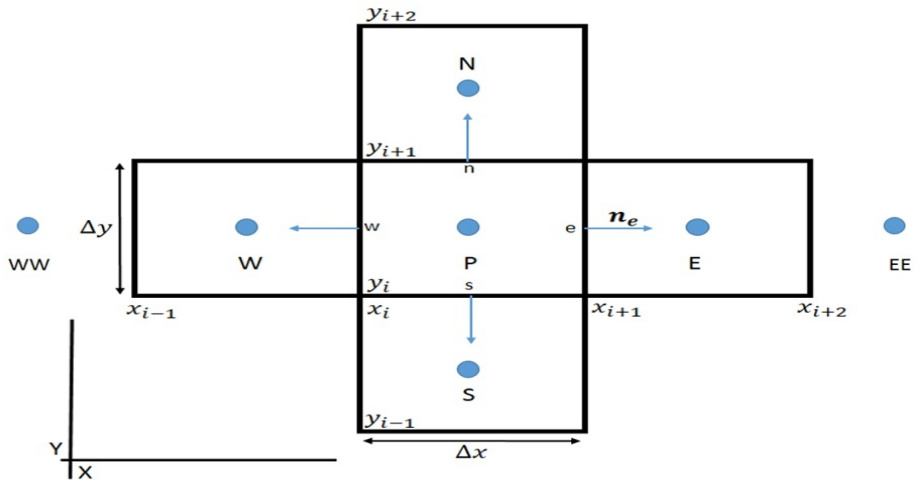

Figure 2.2: A typical CV notation in 2D for Cartesian Coordinates.

To transform this set of PDEs into a set of integral equations, the Gauss first theorem is applied to the advective terms and the transient terms integrated over the CV in time.
The mentioned transformation applied to Equation (2.15) leads to:

$$\int_{\Delta t}\left(\frac{\partial}{\partial t}\int_{CV}\rho\vec{U}dV\right)dt+\int_{\Delta t}\int_{M}\rho\vec{n}\cdot\vec{U}\left(\vec{U}\right)dMdt=$$
$$\int_{\Delta t}\int_{M}\vec{n}.\left(\mu\nabla^{2}\vec{U}\right)dM+\int_{\Delta t}\int_{CV}\rho\vec{g}dVdt-\int_{\Delta t}\int_{CV}\nabla PdVdt+\int_{\Delta t}\vec{F}_{s}dVdt. \quad (2.22)$$

For the pressure term, OpenFOAM© uses the SIMPLE (Semi-Implicit Method for Pressure-Linked Equations) and PISO (Pressure Implicit Splitting Operator) methods, a non-hydrostatic approximation formulation, and an iterative solution by coupling the velocity field and the pressure with the mass conservation equation (Ferziger and Peric, 2002; Versteeg and Malalasekera, 2007).

2.3.2 Discretization Schemes

Several tests are performed to evaluate the effect of different discretization schemes of the convective terms on the solution. Defining $\vec{a}$ as the vector field in the convective

terms, Equation (2.22) is solved assuming that the integral is approximated using the midpoint rule and the integral of the flux over the infinitesimal surface $d\vec{M}$ is approximated as:

$$\int_M \vec{a} d\vec{M} \approx \sum_e \bar{a}_e M_e \approx \sum_e a_e M_e \tag{2.23}$$

Considering that Equation (2.23) is applied on the CV surface and the values of the hydrodynamic variables are available at the CV center node, different methods can be used to interpolate the values from the nodes to the surfaces. This procedure can be done if the variables are function of the values at the node, which can be accomp The style file: apalike.bst I couldn't open database file Chapter2/Reference.biblished by applying some interpolating procedures, i.e. the UPWIND (UD), the Quadratic upwind interpolation for convective kinetics (QUICK) and the Total Variation diminishing (van Leer) interpolation.

The UD interpolation scheme uses the value of the variable at the surface depending on the flow direction, UD is a diffusive scheme, thus a very fine mesh is required to obtain accurate results (Ferziger and Peric, 2002). The value of a_e, following Fig 4.2, is:

$$a_e = \left\{ \begin{array}{l} a_P \text{ if } \vec{U} \cdot \vec{n} > 0 \\ a_E \text{ if } \vec{U} \cdot \vec{n} < 0 \end{array} \right\} \tag{2.24}$$

The QUICK scheme was developed as an improvement of UD where, a parabolic fitting between the points P and E (see Fig.4.2) is implemented, implying the use of an additional point to define the function. This point is selected depending on the direction of the convection process; i.e. if $u_x > 0$, W is selected and conversely, if $u_x < 0$, EE is selected (where u_x is the velocity component in the x direction). This scheme is more accurate than the UD scheme presenting less numerical diffusion although it introduces spurious oscillations for complex flows (Ferziger and Peric, 2002). The third interpolation method evaluated is the van Leer scheme, a second order scheme that allows controlling the spurious oscillations generated by the QUICK scheme. This is achieved by defining a diffusive function. Details of the discretization schemes and their implementation can be reviewed in Ferziger and Peric (2002) and Versteeg and Malalasekera (2007).

2.4 Results

In this section, the dynamic mesh wave generation and propagation methodology is tested against analytical solution as well as with experimental data for a solitary wave. Additionally, the cases for a monochromatic wave over a trapezoidal cross section structure and a solitary wave over a slender column are validated using experimental data reported in the literature and a backward wave breaking process due to vortex influence is explained. All test cases neglect the Reynolds Stress tensor, except for the

Solitary-Slender Column case, where the $\kappa\omega - SST$ turbulent model is used (available in OpenFoam©). All simulations are 2-DV, since we are interested in the wave propagation and transformation rather than its transversal effects. For the numerical stability, the Courant number was restricted to 0.8 and for the free surface and hydrodynamic quantities the absolute error has to be lower than 10^{-6}, before to pass to the next time step. Additionally, in order to determine where the free surface position is on the vertical axis (based on Equations (2.16) and (2.17)), the γ values equal to 0.5 were enough to extract the free surface time series. In order to evaluate the convergence behaviour and mesh independence, different mesh size were chosen to estimate the error, order and ratio of convergence. The order and ratio of convergence are estimated using the UD scheme and three different meshes (see Table 4.1), since the other two schemes are improvements to the this formulation. The error analysis was based on the two finest meshes. The numerical wave flume is a semi-infinite domain in the direction of the wave propagation, increasing the cell size away from the wave propagation zone to induce artificial damping in order to avoid reflection effects.

$\varepsilon = 0.270$	$H/15$	$H/30$	$H/40$
$\Delta x(m)$	0.0054	0.0028	0.0020
$\Delta y(m)$	0.0027	0.0014	0.0010
$\varepsilon = 0.409$	$H/15$	$H/30$	$H/40$
$\Delta x(m)$	0.0082	0.0040	0.0030
$\Delta y(m)$	0.0040	0.0020	0.0015

Table 2.1: Wave non-linearity and mesh properties for the numerical experiments for the solitary wave on a flat bottom case.

2.4.1 Solitary Wave on a Flat Bottom

The profile for the solitary wave in the Boussinesq approach takes the form, (Chang et al., 2001)

$$\eta = H \operatorname{sech}^2 \left(\sqrt{\frac{3H}{4h^3}} (x - ct) \right) \tag{2.25}$$

where c is the wave celerity, H the wave height and h the still water depth. The damping due to viscous effects along its propagation direction can be included by using the Keulegan's formulation (Keulegan, 1948; Liu and Orfila, 2005; Liu et al., 2006).

The numerical domain is a 25 m long, 0.6 m wide and 0.9 m deep in a 0.15 m still water depth. Two different values for the non-linear wave characteristics ($\varepsilon = H/h$) are tested. The vertical mesh resolution is defined by dividing H by 15, 30 and 40 (for both wave cases); and the horizontal resolution is based on the mesh quality defined in section 3. In Table 4.1, the mesh resolution for $H/15$ ($Mesh1$), $H/30$ ($Mesh2$) and $H/40$ ($Mesh3$) are shown and the error analysis is presented for $Mesh2$ and $Mesh3$

since the relative error based on the wave peak differences was defined to be lower than 20%.

Model convergence behaviour

In order to evaluate the performance of the numerical wave flume, it is important to assess the convergence of the solution against the analytical one. The formulations presented in this section follow the E. and Hoekstra (2008) methodology. To estimate the order and ratio of convergence, three different meshes have been implemented with a refinement ratio below 2.5, the slip boundary condition and the advective term UD since this formulation solves the flow quantities based on the flow direction being the other two improvements of the former.

Having three different grid size δ_1, δ_2 and δ_3, and their specific variables (scalar or vectorial) solution ϕ_1, ϕ_2 and ϕ_3 (the free surface wave in this case), the convergence ratio can be estimated by Equation (2.26) as:

$$\Gamma = \frac{\phi_2 - \phi_1}{\phi_3 - \phi_2} \tag{2.26}$$

where ϕ_1 stands for the finest grid solution, ϕ_2 for the intermediate grid solution and ϕ_3 the coarsest grid one and convergence conditions are defined as:

$0< \Gamma <1 \quad => \quad$ Monotonic convergence
$-1< \Gamma <0 \quad => \quad$ Oscillatory convergence
$\Gamma <-1 \quad => \quad$ Monotonic divergence
$\Gamma >1 \quad => \quad$ Oscillatory divergence

For the order of convergence (j), a fitting to an error estimator values is done by a power function expressed by Equation (2.27)

$$E_r = \phi_i - \phi_0 = \zeta h_i^j \tag{2.27}$$

where ζ is a coefficient and ϕ_0 is the free surface reference value estimated by using Equation (2.25) at three recording station (see Fig 4.1).

The results for j for both nonlinearity values (ε equals to 0.27 and 0.409) using the wave peak error and having R-square higher than 80% (in the fitting), are presented in the Table 2.2. Additionally, Γ values reported in this work are an average between the three recording stations illustrated in Fig 4.1. As can be observed, using both parameters, the numerical solution shows a *Monotonic convergence* behaviour and the error analysis can be done using the two finest meshes.

$\varepsilon =$	0.270
j	0.4368
Γ	0.4121
$\varepsilon =$	0.409
j	0.6412
Γ	0.5262

Table 2.2: Numerical wave flume convergence behaviour.

Generation Method	UPWIND Discretization Scheme $\varepsilon = 0.270$				UPWIND Discretization Scheme $\varepsilon = 0.409$			
	$M1$	$M2$	$M3$	Ω	$M1$	$M2$	$M3$	Ω
$G\ Mesh2$	-7.2	-10.6	-11.8	0.055%	-8.8	-12.5	-15.4	0.08%
$G\ Mesh3$	-4.4	-7.4	-10.1	0.046%	-6.3	-9.5	-12.3	0.074%
	van Leer Discretization Scheme $\varepsilon = 0.270$				van Leer Discretization Scheme $\varepsilon = 0.409$			
$G\ Mesh2$	-5.9	-8.8	-11.3	0.044%	-5.1	-8.4	-11	0.072%
$G\ Mesh3$	-3.3	-6.2	-8.6	0.043%	-3.7	-6.4	-8.9	0.064%
	QUICK Discretization Scheme $\varepsilon = 0.270$				QUICK Discretization Scheme $\varepsilon = 0.409$			
	$M1$	$M2$	$M3$	Ω	$M1$	$M2$	$M3$	Ω
$G\ Mesh2$	-5.8	-8.8	-11.2	0.044%	-4.5	-7.9	-10.5	0.074%
$G\ Mesh3$	-3.4	-6.3	-8.6	0.042%	-3.3	-6.3	-8.7	0.066%
	QUICK Discretization Scheme $\varepsilon = 0.270$				QUICK Discretization Scheme $\varepsilon = 0.409$			
	$M1$	$M2$	$M3$	Ω	$M1$	$M2$	$M3$	Ω
$Ra\ Mesh3$	-1.9	-3.9	-6.4	0.032%	4.6	1.7	-1.06	0.07%

Table 2.3: Numerical relative wave peak error (%) and wave peak decay with respect to theory for the solitary wave on a flat bottom case using all the numerical schemes.

Slip flat bottom

First, the model is tested against the theoretical wave peak solution given by Equation (2.25), considering a slip condition on the bottom (no friction) and varying the mesh resolution to determine the effect of the mesh size on the numerical results. For all cases, the relative wave peak error and main wave peak decay (Ω) (evaluated by taking the mean slope along three measuring points) are obtained at three locations along the numerical wave flume, for all numerical schemes. These virtual wave gauges are at the same locations than the experimental ones (see locations in Fig 4.1). Errors for the three schemes and the two waves are reported in Table 2.3 and a time history at the three gauges for the three schemes and for the two wave non-linearities in Fig 4.4 and 4.5, respectively. As seen, the Goring-Raichlen wave theory with $Mesh3$,

gives the best solution with all the numerical schemes. The appropriate mesh and advective numerical scheme is used for comparing the Keulegan's solution against the experimental data with the Rayleigh wave generation method (Ra), a more accurate theory than the Goring-Raichlen (G) (Katell and Eric, 2002). However, recent works using experimental and numerical approaches where Equation (2.3) is modified using the Fenton's wave profile, show improvement in the attenuation of the trailing waves and a reduction of the main wave peak decay (Wu et al., 2014,0). This formulation is more accurate for pure solitary wave generation than the other theories mentioned above. Also, it is important to remark that the experimental data available for the model validation, comes from the Goring and Rayleigh formulations and the Fenton's improvement will not be used in this work.

	$Model$	$Keulegan$	$Model$	$Keulegan$
	$\varepsilon = 0.270$		$\varepsilon = 0.409$	
Ω	0.039%	0.045%	0.08%	0.081%

Table 2.4: Model and Keulegan's Wave decay rates for two wave non-linearity factors.

It is important to note that the exact solution of the paddle movement in the G approach is obtained from a system of equations which implies a larger computational effort. The paddle movement for the cases studied is presented in Fig 4.3 which reproduces Equation (2.7) and (2.8), and the G simplification given by Equation (2.28):

$$\xi(t) = S_G \tanh\left(7.6\left(\frac{t}{\tau_G} - 0.5\right)\right) \tag{2.28}$$

Which obeys the hyperbolic tangent function, avoiding the need of an iterative solution for the boundary condition at each time steep.

Regarding the G method, the numerical solutions for both non-linear wave parameters underestimates the wave peak giving the highest trailing wave amplitude. The Ra method, overestimates the main wave height and diminishes the trailing wave amplitude.

All methods reproduce the spurious trailing waves (Fig 4.4, 4.5, 3.6 and 3.7) for both non-linear wave values tested. G is the method with the highest trailing wave amplitude and the smallest trailing wave period. Conversely, the Ra method, gives the smallest amplitude and the larger wave period for both ε values. Note that an increment of the non-linear parameter generates an increment in the amplitude of the trailing waves and a reduction in their wave period. Not significant effects in the wave celerity and the trailing waves have been noticed regarding the discretization scheme. Additionally, the wave decay rate and the error in the wave peak increase with larger non-linearities due to limitations in the wave generation theories as already reported

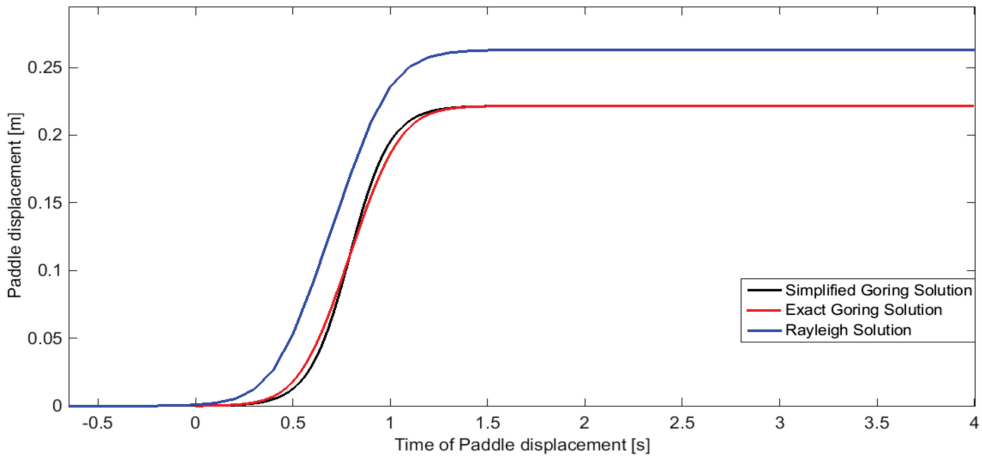

Figure 2.3: Paddle displacement with different theories for $\varepsilon = 0.270$.

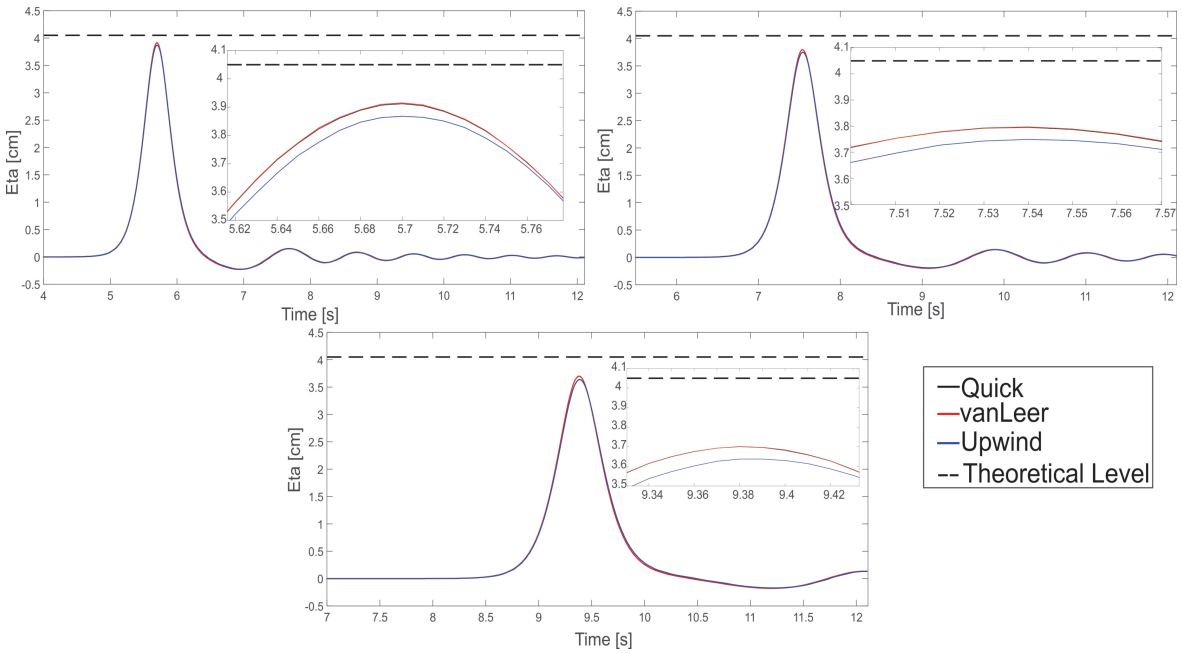

Figure 2.4: Numerical time history (and zoom at the peak) of the wave profile at M1(Left), M2(Right) and M3(Down) for $\varepsilon = 0.270$ for three discretization schemes, theoretical and Goring-Raichlen theory.

by Katell and Eric (2002) and Wu et al. (2014).

Based on the results (Table 2.3), the $Mesh3$ and the QUICK scheme are selected for the wave simulation and comparison with Keulegan's solution and experimental data. However, it is important to remark that the van Leer and QUICK solutions are very close to each other, showing differences between them below 1% for all the

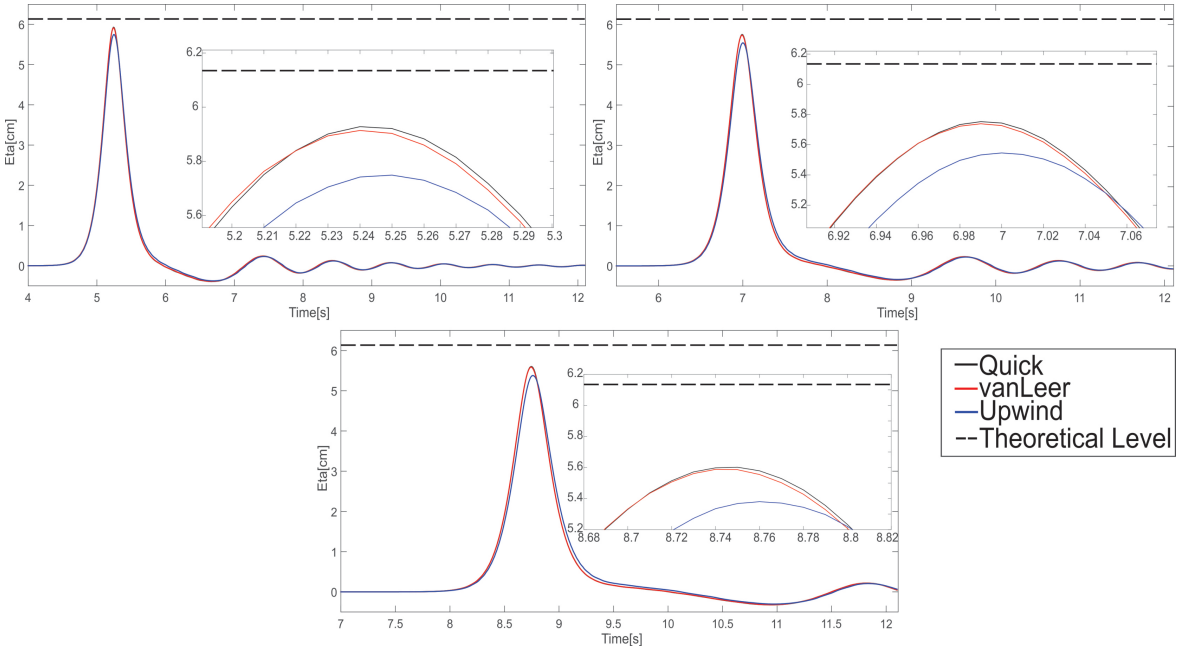

Figure 2.5: Numerical time history (and zoom at the peak) of the wave profile at M1(Left), M2(Right) and M3(Down) for $\varepsilon = 0.409$ for three discretization schemes, theoretical and Goring-Raichlen theory.

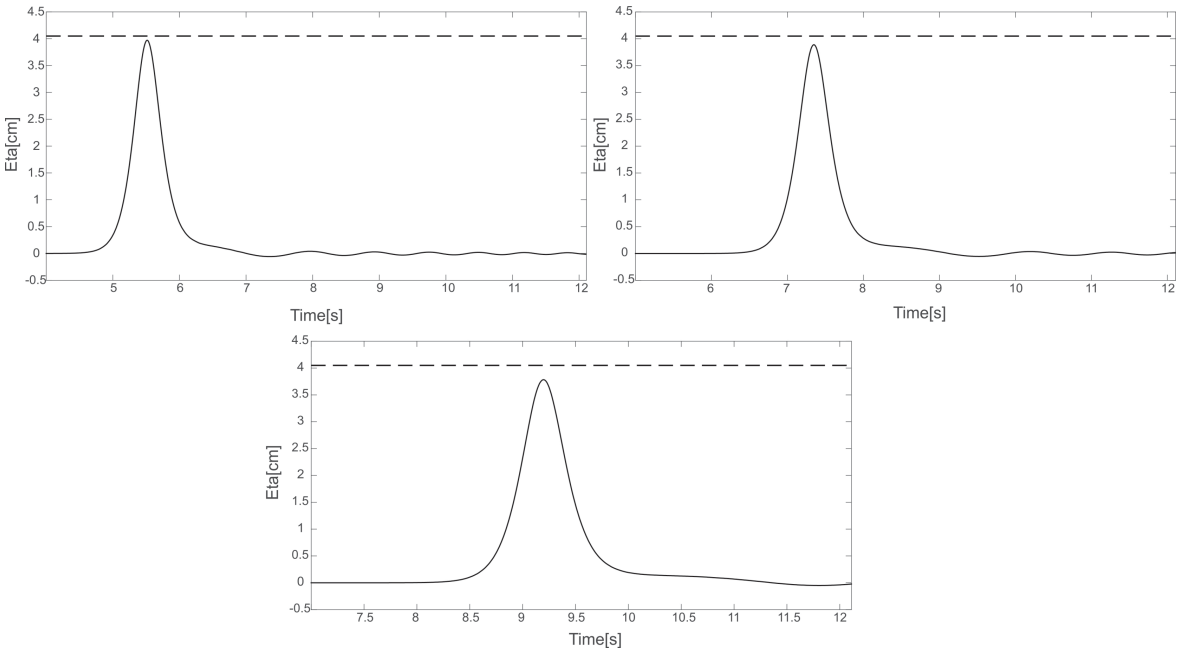

Figure 2.6: Numerical time history of the wave profile at M1(Left), M2(Right) and M3(Down) for $\varepsilon = 0.270$ using the Quick scheme, $Mesh2$, theoretical free surface and Rayleigh theory.

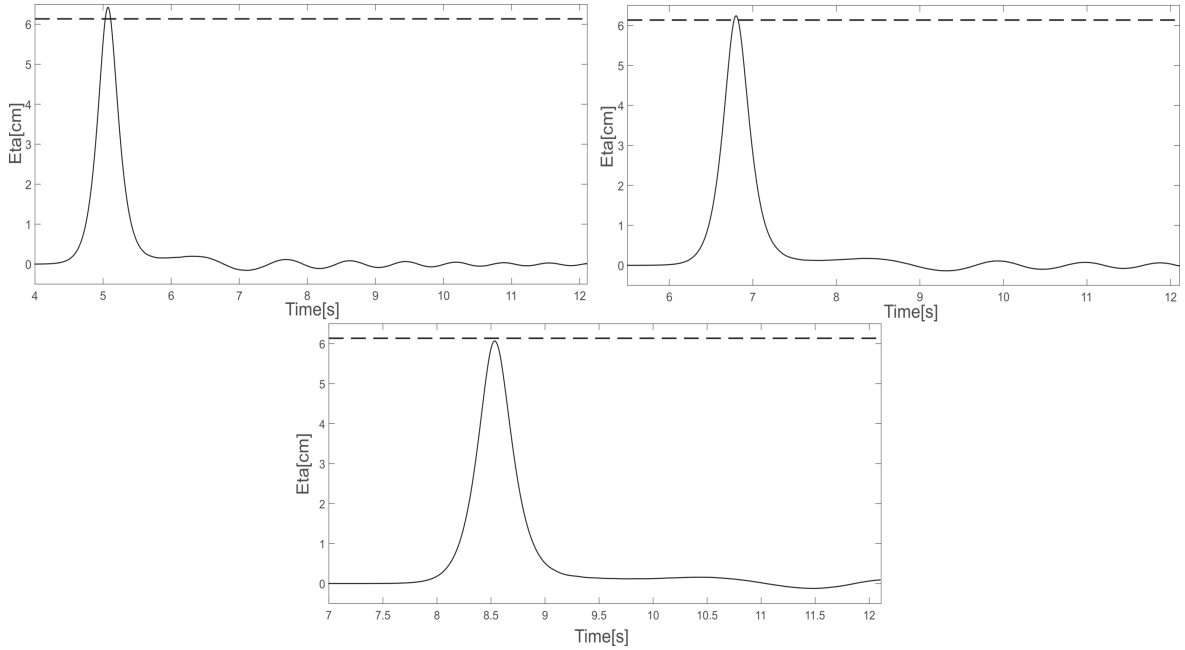

Figure 2.7: Numerical time history of the wave profile at M1(Left), M2(Right) and M3(Down) for $\varepsilon = 0.409$ using the Quick scheme, $Mesh2$, theoretical free surface and Rayleigh theory.

simulations.

Non slip flat bottom

Keulegan (1948), modified the solution for the theoretical solitary wave by including the effect of the bottom friction in order to model a realistic wave. Fig 3.8 and Fig 3.9 show the numerical solution obtained with the Ra method, the QUICK scheme and the decay rate for both non-linearity factors. For comparison purposes, the decay rate obtained by the Keulegan's correction is also included. The numerical model considers a non-slip boundary condition on the channel bottom ($u_x = 0$). The errors in the decay rate are summarized in Table 2.4 indicating that the numerical model gives smaller decay rate than the value predicted by Keulegan's formulation. The theoretical an numerical decay rate increase as the non-linear factor does.

Validation against experimental data

In this section we validate the model agaist the experimental data presented in Liu et al. (2006) for a solitary wave. These experiments were performed in a wave flume with the same characteristics as the numerical domain shown in the previous Section. For the validation, two solitary waves with the same non-linear parameters as those presented above were compared at locations $M1$, $M2$, and $M3$. Additionally, the numerical model considers the Rayleigh wave generation theory, a non-slip boundary

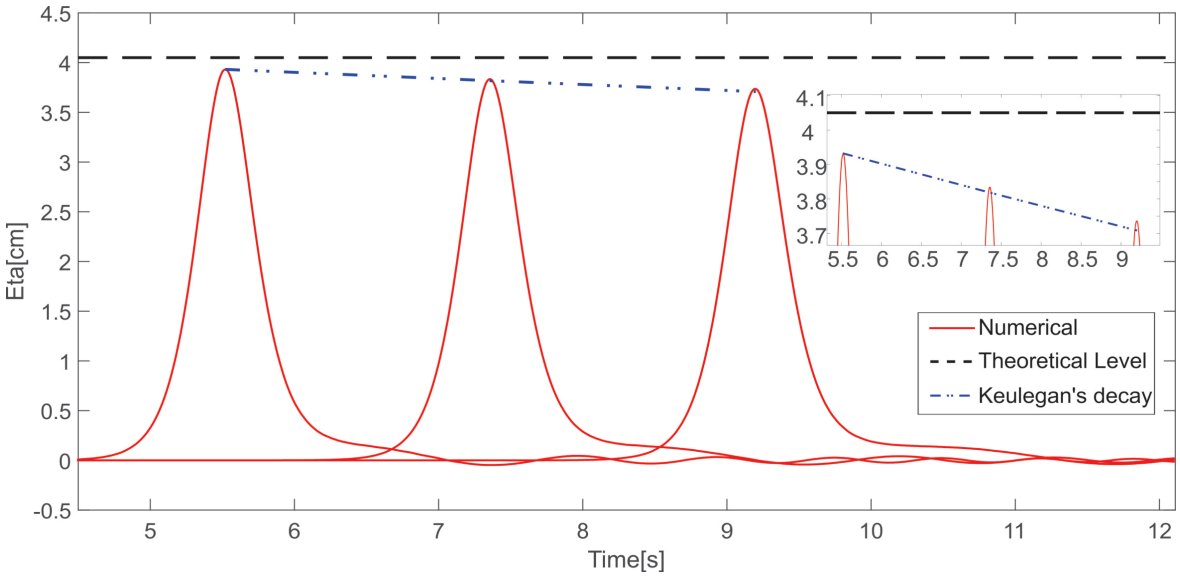

Figure 2.8: Numerical time history of the wave profile at M1, M2 and M3, the Kuelegan′s viscous damping by bottom friction and theoretical wave peak for $\varepsilon = 0.270$.

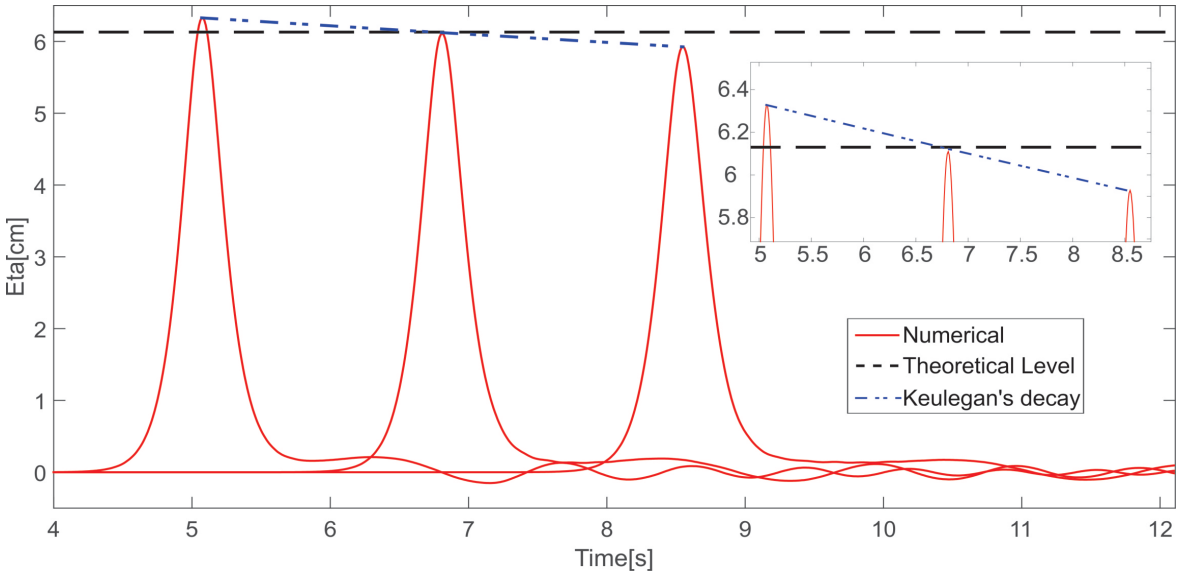

Figure 2.9: Numerical time history of the wave profile at M1, M2 and M3, the Kuelegan′s viscous damping by bottom friction and theoretical wave peak for $\varepsilon = 0.409$.

condition at the bottom and the QUICK scheme for the advective terms.

Model results and laboratory data are shown for $\varepsilon = 0.270$, at the three locations in Fig 3.10. The errors for the wave amplitude are shown in Table 2.5. From these figures it is clear that the model captures accurately the shape of the wave although underpredicts the wave amplitude. This error slightly increases in the direction of the

wave propagation indicating that the model overpredicts the wave decay rate. For $\varepsilon = 0.409$ (Fig 2.11), the model overpredicts the wave decay rate and the magnitude of the wave peak with errors up to 3.1% (Table 2.5). The numerical model overpredicts the wave peak decay rate for both non linear wave values, with the highest relative error of 5.5% for $\varepsilon = 0.270$.

$\varepsilon = 0.270$			$\varepsilon = 0.409$		
$M1$	$M2$	$M3$	$M1$	$M2$	$M3$
3.0	4.3	5.5	3.11	0.62	-0.95

Table 2.5: Relative wave peak error (%) between numerical and experimental data.

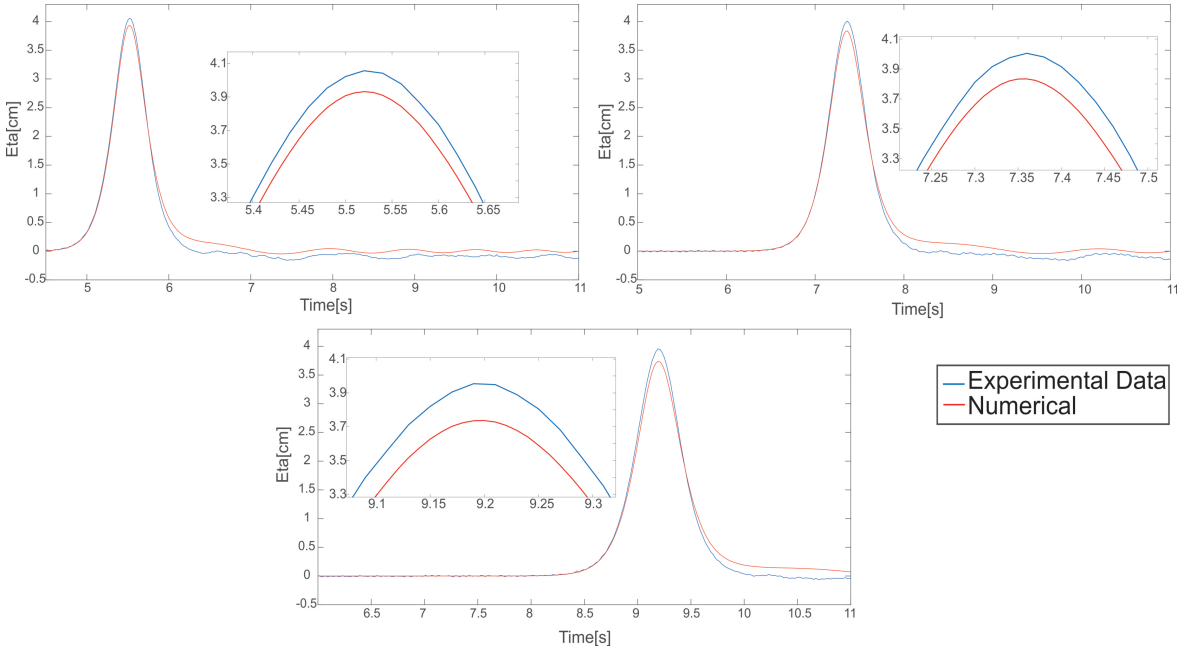

Figure 2.10: Numerical and experimental (Liu et al., 2006) time history of the wave profile at M1, M2 and M3 for $\varepsilon = 0.270$.

At M1 and for $\varepsilon = 0.270$, (Fig 2.12 left), the trailing waves have a maximum amplitude of 0.16 cm (4.43% of the main wave) with almost a constant period of 1.3 s. At this location, the model reproduces the trailing waves of the same amplitude but with a shorter period than those measured in the experiments. These waves detach earlier from the main wave than the experimental ones leading to a wave profile which is above the experimental one.

For the non-linearity factor $\varepsilon = 0.409$, the experimental and the numerical trailing waves at $M1$ (Fig 2.12 right), are in much better agreement than for the other

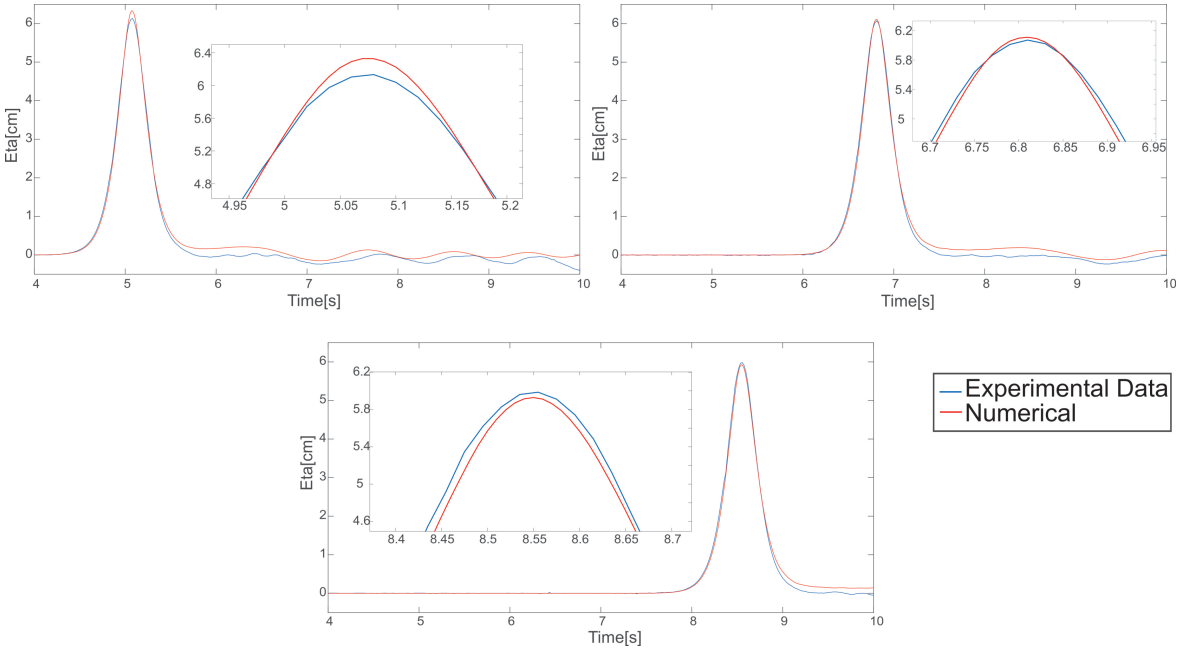

Figure 2.11: Numerical and experimental (Liu et al., 2006) time history of the wave profile at M1, M2 and M3 for $\varepsilon = 0.409$.

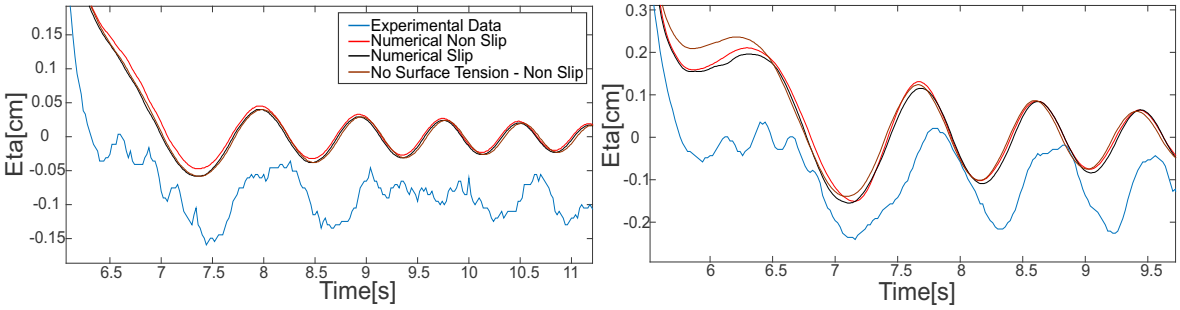

Figure 2.12: Numerical and experimental (Liu et al., 2006) trailing wave profile at M1 for $\varepsilon = 0.270$ (Left) and $\varepsilon = 0.409$ (Right).

non-linearity factor (amplitude of 0.27 cm or 4.8% of the main wave and period of 0.98 s). For this nonlinearity, the simulated waves detach at the same time than the experimental ones.

The analysis of the trailing waves shows that viscosity has little effect. For both non-linear factors and for slip (viscous fluid without bottom friction) and non slip (viscous fluid and bottom friction), the numerical results show that neither the fluid viscosity nor the bottom friction nor the surface tension have effect on the trailing waves, since they are modulated by the gravity term (from Equation (2.15)). Additionally, the *Weber* number (We) was estimated applying the linear wave theory showing different behaviour for the theoretical and the numerical computations when

neglecting the surface tension (Fig 2.12). The theoretical estimation of the We number is around 0.6 and 1.7 for ϵ 0.27 and 0.41 respectively indicating that effects of surface tension is important. In the numerical simulations, there are no differences for both nonlinearity factors.

At stations $M2$ and $M3$, the recording time in the experiments were too short to provide information about the trailing waves.

2.4.2 Monochromatic wave passing over a Trapezoidal cross section

In this Section, the numerical model is tested with the experiments by Dingemnas (1993) for a monocromatic wave interacting with a submerged trapezoidal cross section structure. The still water level is h=40 cm, the wave height H=2 cm and the wave period T=2.02 s; the incident Ursell number is $U_r = 4.5$, so the wave generation theory presented above is adequate and the wave can be modelled in the linear wave theory range. The submerged structure is 30 cm height and 11 m long (see Fig 2.13). To validate the model, the experimental free surface from the wave gauges (in red box D1, D2, D3 and D4) are compared against the numerical results. The distance from the paddle to the wave gauges are 2, 13.5, 15.7 and 19 meters, respectively. It is important to remark that the numerical simulation, the spectral analysis and error estimates were computed during a simulation of 45 seconds, but only the first 38 seconds are shown for illustration purposes.

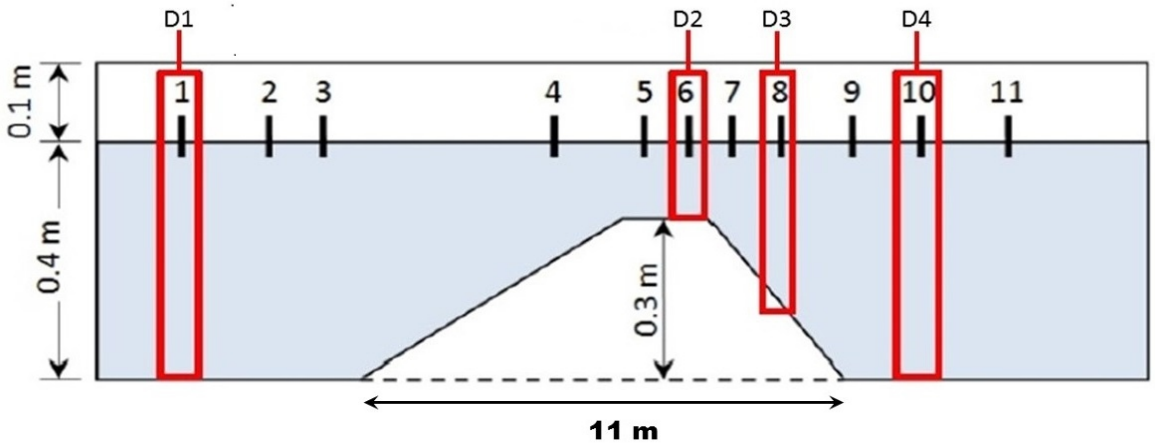

Figure 2.13: Dingeman's experimental set-up. (Modified from (Lambert, 2012))

The model results are shown in Fig 2.14 to Fig 2.17 in the time (lower panel) and frequency (upper panel) domains, respectively. All numerical results are recorded at the same location as the experimental ones, eliminating the need to calibrate the numerical incoming wave with the first experimental wave gauge, something that has to

be done when using static meshes. From the time series presented in Fig 2.14, the wave at D1 is a "perfect monochromatic wave"; however the wave at D2 and at the structure downstream slope (stations D3 and D4) has been transformed, generating *free waves* that detach from the main wave gaining energy by diffusion effects (Huang and Dong, 1999), even at points where secondary harmonics are as high as the incident one (D3 and D4). Comparison between numerical results and experimental data is presented in terms of the Agreement Index (AI), the Mean Absolute Error (MAE) and the Mean Bias Error (MBE) (Willmott and Matsuura, 2005) applied wave by wave. The error analysis shows that along the numerical domain, the model agrees very well with the experimental data (AI>98% and MAE< $7.5*10^{-4}$ meters) at all stations and the MBE for the records is around zero with a mean value close to $3 * 10^{-4}$ meters, showing a small over-prediction respect to the experimental data (see Fig 2.18). Furthermore, the wave error behaviour (AI) is very stable for all the waves (see Fig 2.18), implying that the model does not need a warming time interval being able to solve the physical behaviour of the variables from the initial time of simulation. Those *free waves* are explained from the wave mechanics viewpoint by using fully nonlinear Boussinesq models (Galan et al., 2013), where the wave trains are propagated from a deeper water to a shallower one. In deep water, the dispersion is more important than the nonlinear effects, but when the waves reach the shallow water, the nonlinear effects becomes more relevant and the dispersion decreases. In that moment, higher harmonics are released by the nonlinear processes and those harmonics are more dispersive than the incident waves when they reach deeper waters again.

Using a FFT decomposition of the free surface time series, it is possible to detect the wave frequencies as is shown in the upper panel of Fig 2.14 - Fig 2.17, where the vertical axes are twice the wave amplitude ($2A$) normalized by the incident wave height (Hi). At D1, the main frequency is 0.5 Hz (corresponding to the target wave) and downstream the structure, higher frequencies appear (D2, D3 and D4) with energy comparable with the incident wave(D3 and D4). These frequencies correspond to the *free waves* that travel slower than the incident phase velocity (Huang and Dong, 1999). They are the result of the water column variation that produces an increment in the advective acceleration (positive or negative). This acceleration is positive on the upstream slope and on the top (flat zone) of the structure up to the beginning of the structure downstream slope, where the acceleration is negative. Due to the change in the hydrodynamic conditions along the submerged structure, the mass conservation requires the free surface to adjust to the new flow conditions at the boundaries, increasing the wave steepness and also increasing the wave nonlinearity over the upstream slope and at the top of the structure. Over the downstream slope, the diffusive term in the momentum equation is more relevant than the advection term transfering energy from lower to higher frequencies. Notice that this structure has very mild slopes, long flat top and the ratio of its height-base lengths is much less than unity, working as a flat structure in an almost parallel flow (no flow separation occurs). For this type of physical processes together with low Reynolds number, we call them "Linear fluid structure interaction mechanism" from the fluid mechanics point of view.

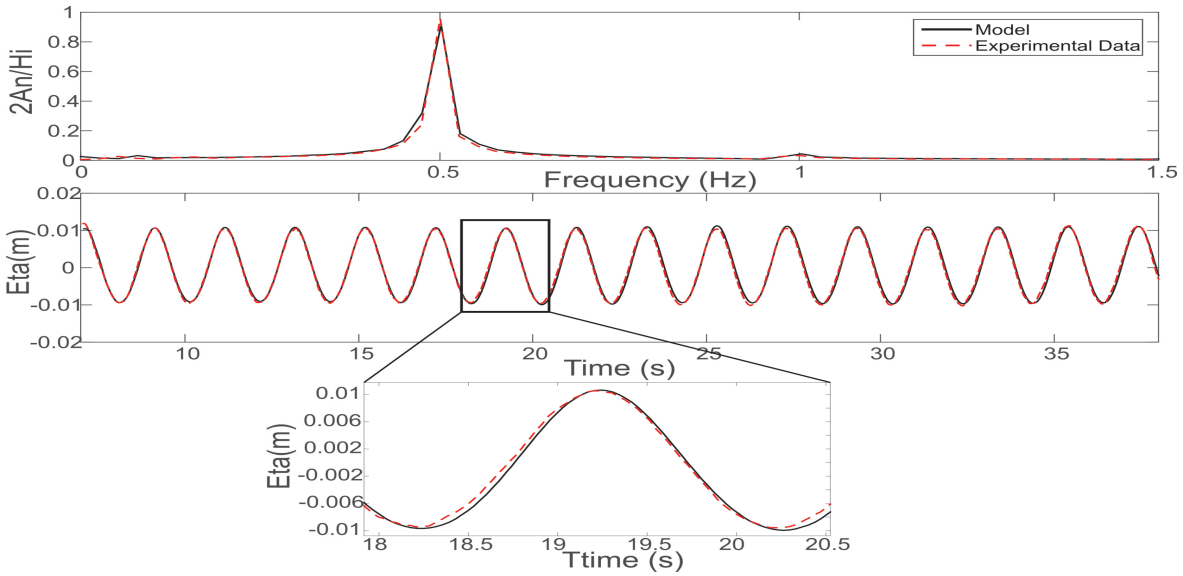

Figure 2.14: Dingeman's experimental data and numerical model results in the free surface (lower) and frequency (upper) domain at 6 meters from the Wavemaker (D1). Numerical (Black) Vs. Experiments (Red).

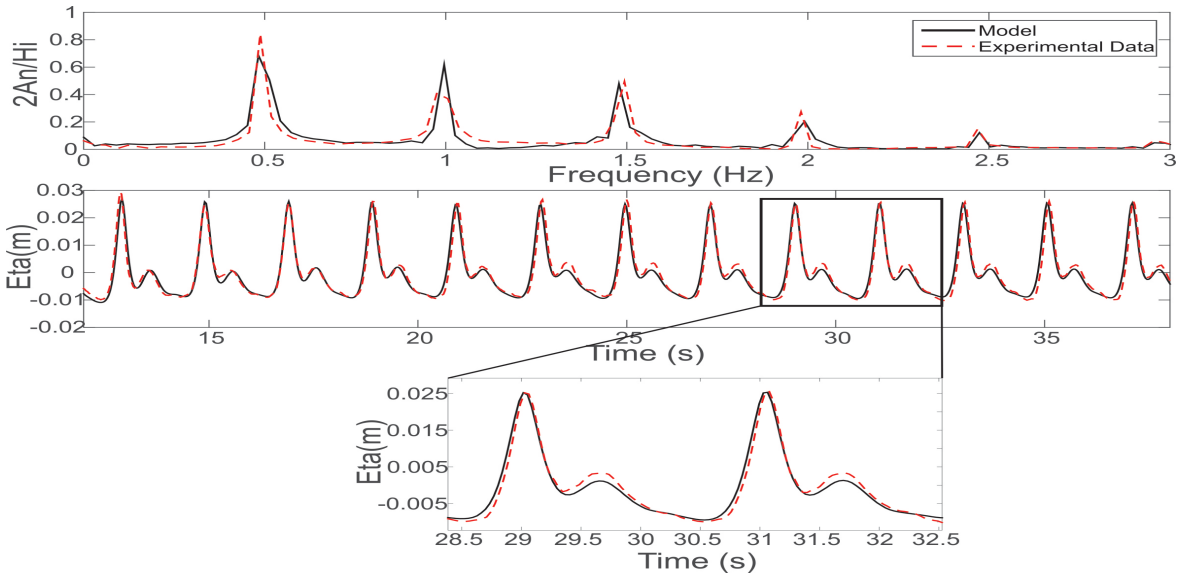

Figure 2.15: Dingeman's experimental data and numerical model results in the free surface (lower) and frequency (upper) domains at 13.5 meters from the Wavemaker (D2).

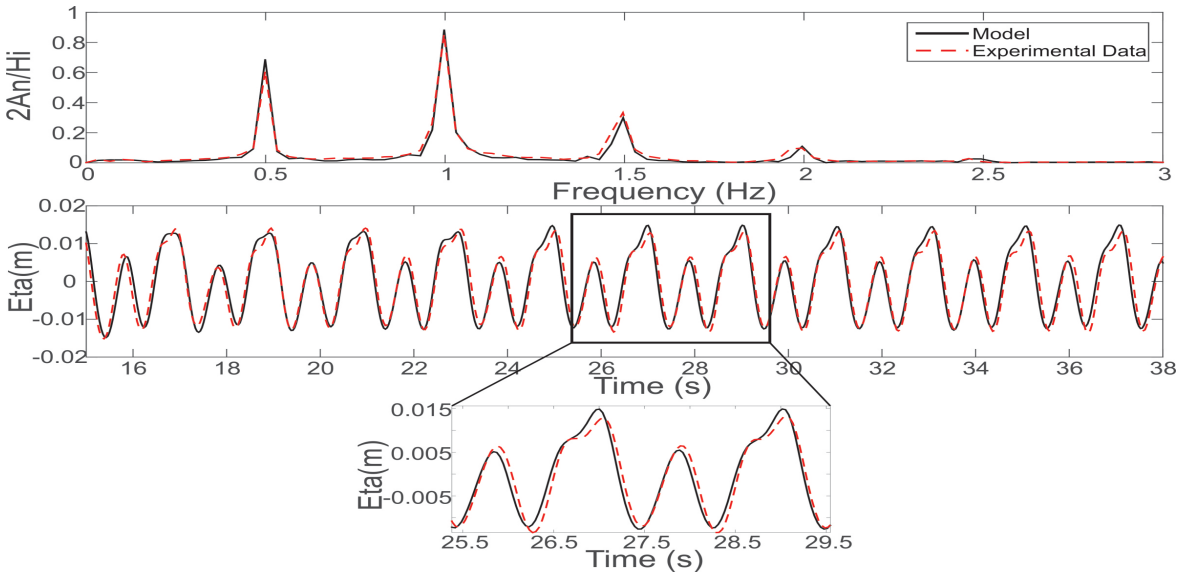

Figure 2.16: Dingeman's experimental data and numerical model results in the free surface (lower) and frequency (upper) domains at 15.7 meters from the Wavemaker (D3).

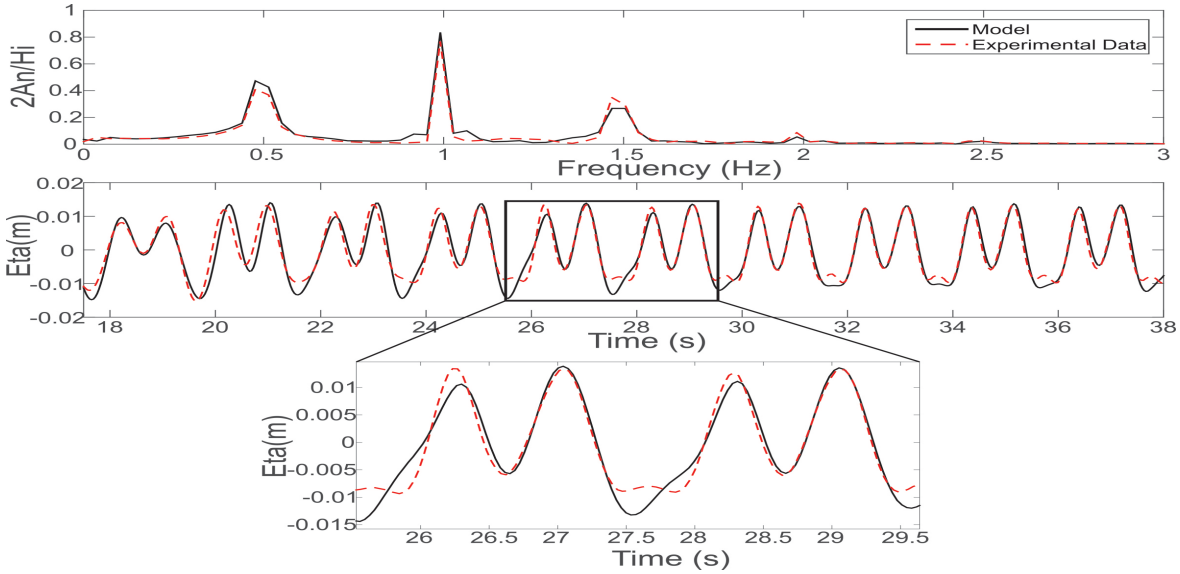

Figure 2.17: Dingeman's experimental data and numerical model results in the free surface (lower) and frequency (upper) domains at 6 meters from the Wavemaker (D4).

2.4.3 Solitary Wave-Slender Structure interaction

At higher complexity, in this section the model is tested with a solitary wave interacting with a slender column. Results are compared against the data published by Wu et al. (2012). The Goring and Raichlen (1980) theory is used for the generation of the solitary wave, since it is the used by the work of Wu et al. (2012). The still water level

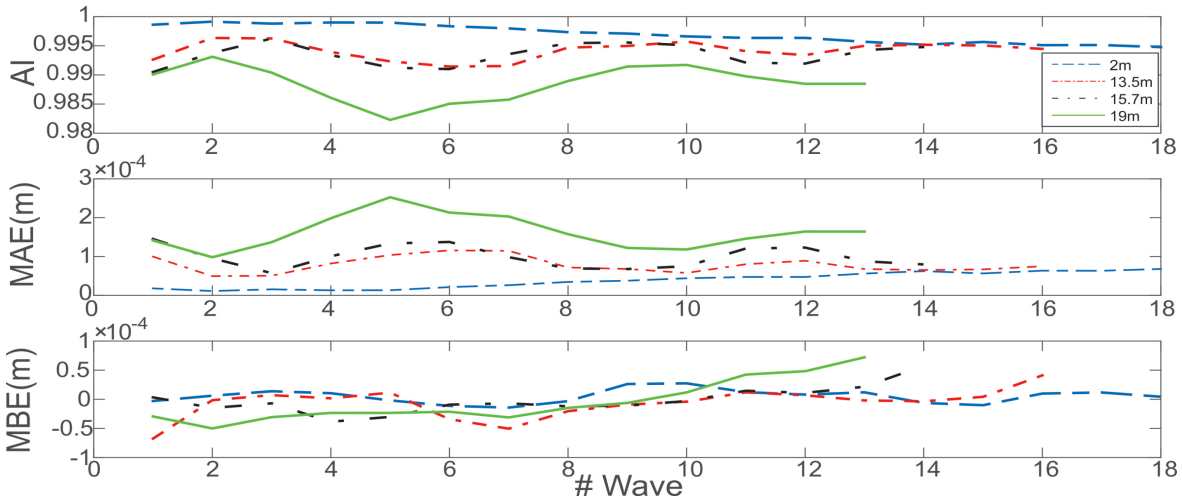

Figure 2.18: Index of agreement, Maximum absolute error (MAE) and Mean bias error (MBE) for all stations.

is h=14cm and the wave height H=7cm; with a nonlinear parameter of $\varepsilon = 0.5$. Wave breaking is presented downstream of the structure. The submerged structure is 10 cm high (d) and 2 cm thick (w). The experiment set up is shown in Fig 2.19. The mesh size close to the solid walls is 0.8 millimetres. To validate the model, the PIV velocity field data is qualitatively compared against the numerical results and quantitatively with the vertical velocity profiles.

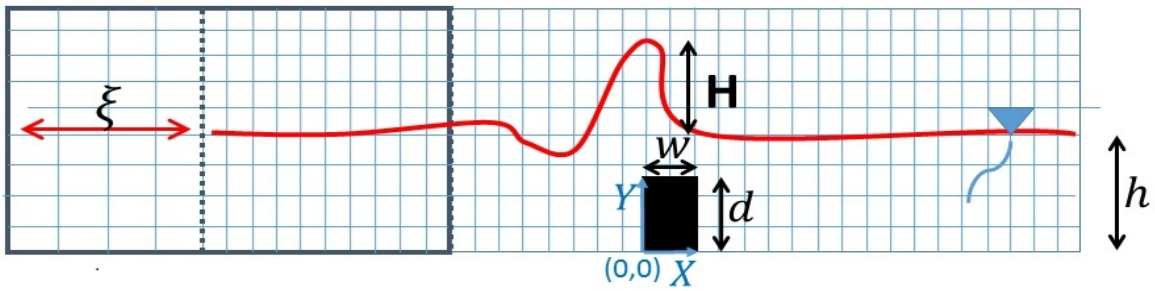

Figure 2.19: Overview of the numerical and experimental set-up based on (Wu et al., 2012).

For the numerical configuration, the turbulent 2-D vertical $\kappa\omega - SST$ model is used with the no-slip condition at the bottom, zero velocity at the end of the wave flume and zero gradient pressure on the walls (bottom and structure). The turbulent quantities on the solid walls (sub index w) and at the free-stream (sub index ∞) are set based on

the formulation suggested by Hellsten (1998) (Equations (2.29)-(2.33))

$$\omega_w = \frac{2\nu}{0,075 d_*^2} \tag{2.29}$$

$$\kappa_w = 10^{-7} \tag{2.30}$$

$$\omega_\infty = \Gamma \frac{U_\infty}{L} \tag{2.31}$$

$$\nu_t = 10^{-3}\nu \tag{2.32}$$

$$\kappa_\infty = \nu_t \omega_\infty \tag{2.33}$$

where ν, d_* and Γ are the fluid viscosity, the first node wall distance and a proportionality coefficient between 1-10, respectively. The eddy viscosity at the boundary layer (ν_{tw}) follows the formulation presented by Spalding (1961), which is valid along the entire boundary layer, from $Y^+ \sim 1$ to $Y^+ > 30$. The advective terms in the transport equation are solved using the QUICK scheme.

Eight velocity profiles at five different instants are compared with the experimental data. These profiles are taken from $z = -h$ to $z = \eta$ at 0.06, 0.08, 0.1, 0.12, 0.14, 0.16, 0.18 and 0.2 meters from the downstream face of the slender column. Comparisons are performed at $t = 0.46, 0.6, 0.74, 0.88, 1.02$ seconds after the wave crest reaches $x = -0.657m$ (see Fig 2.19). Additionally, a qualitative comparison between velocity fields is shown for each time.

Maximum errors for the horizontal and vertical velocity components for each time are reported in Table 2.6, showing that the AI is higher than 83%. The lower AI and the higher MAE are obtained at $t = 1.02$ seconds (the post-breaking time). The highest discrepancies are obtained when the horizontal velocity profile has the strongest inflexion point (center of the vortex) with a vertical velocity slightly close to the vortex center. In this situation, the model underpredicts the velocity gradients, decreasing the vorticity (see Fig 2.20 - Fig 2.24).

t	$MAE - U[\frac{m}{s}]$	$MAE - V[\frac{m}{s}]$	$AI - U$	$AI - V$
0.46	0.022	0.0245	0.97	0.93
0.6	0.042	0.055	0.96	0.88
0.74	0.05	0.08	0.95	0.84
0.88	0.08	0.08	0.93	0.84
1.02	0.08	0.09	0.91	0.83

Table 2.6: Error estimation for the worst velocity profile at each time steep. Case of the wave passing the slender column

The vortex structure and the magnitude of the velocity are in agreement with the experimental ones (Fig 2.20 - 2.24, upper panel). At $t = 0.46$ s, a flow separation appears due to the drag pressure force exerted on the flow, inducing an adverse pressure

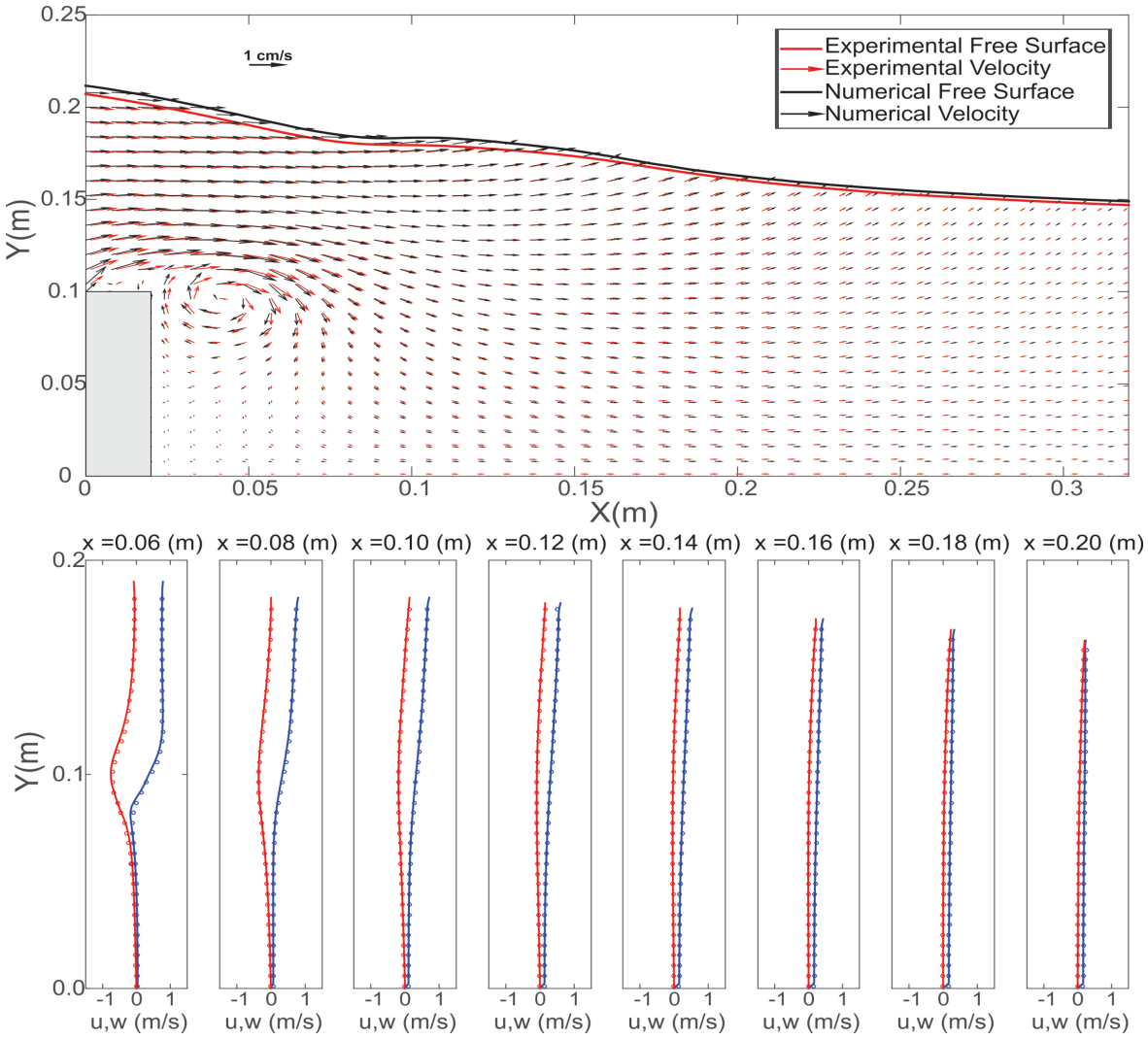

Figure 2.20: Experimental (Wu et al., 2012) and Numerical velocity field comparison (upper panel), and velocity profiles (lower panel) (Blue-horizontal and Red-vertical components) at $t = 0.46$ seconds.

gradient exerted by the solid column (the main vortex). At this time two vortices arise: the main vortex located downstream the column and a second one at the top of the structure, both reported by Wu et al. (2012). The main vortex is advected by the wave with velocity magnitudes decreasing slightly in the wave propagation axis. This behaviour is observed by following the vortex velocity profiles all time steps and noticing that the vertical velocity close to the vortex center (upstream and downstream) has an almost "constant" value of 1 m/s and the difference between the upper and lower (around the vortex center) horizontal velocities is also 1 m/s (see Fig 2.20 - 2.24, lower panel). Following these description, we hypothesize that, the vortex travels faster than what it is being diffused by turbulent and viscous effects; so that the advective term is more relevant than the diffusive one in the transport equation. This behaviour is

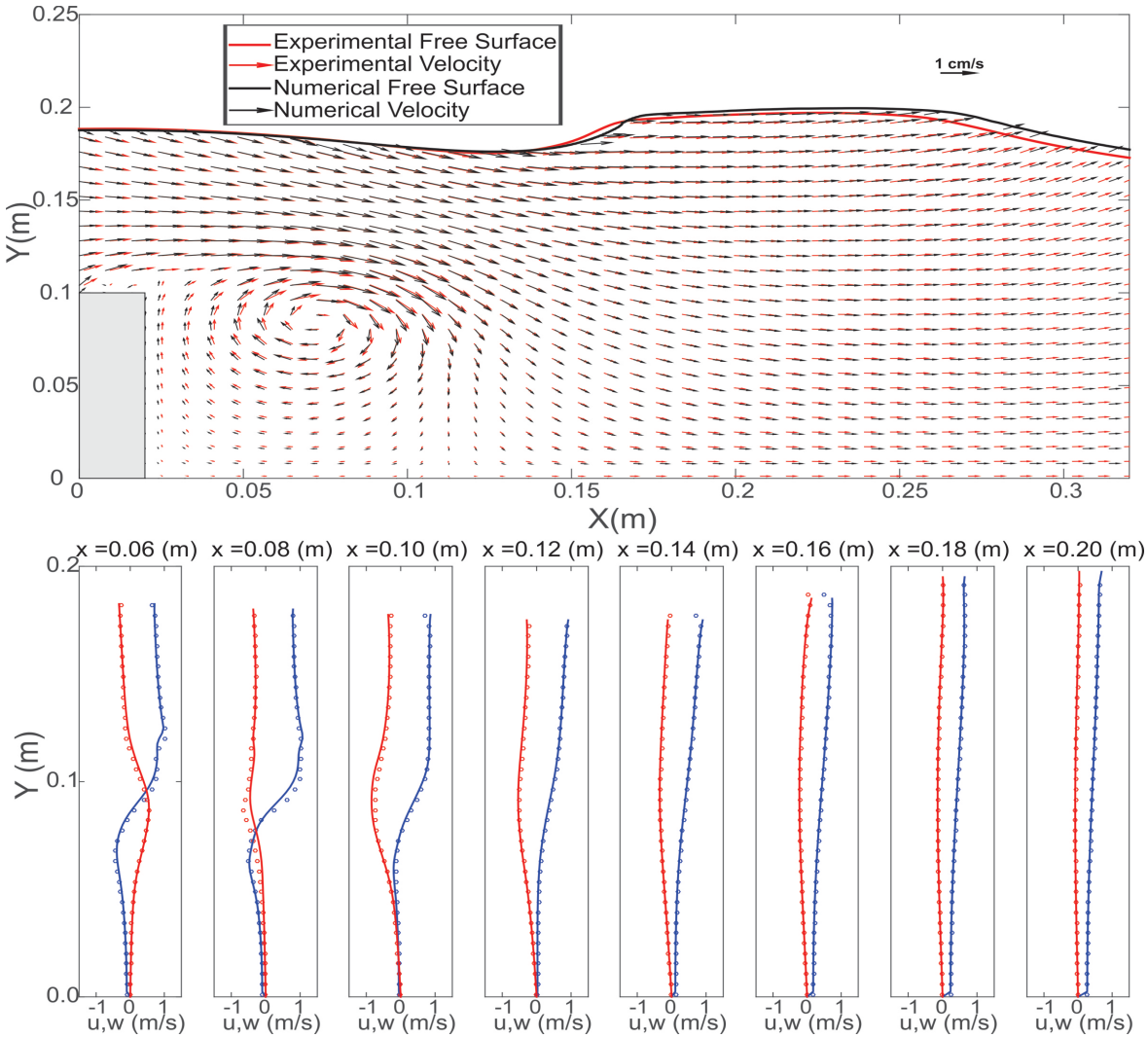

Figure 2.21: Experimental (Wu et al., 2012) and Numerical velocity field comparison (upper panel), and velocity profiles (lower panel) (Blue-horizontal and Red-vertical components) at $t = 0.6$ seconds (before the wave breaking).

in contradiction with Chang et al. (2001), who postulated that the diffusion is higher than the advection downstream the submerged obstacle.

As the main vortex travels along the wave propagation axis, the vortex on the top of the structure vanishes, since there is no significant flow over the column. The vortex generated by the flow separation induces downstream a steeper free surface profile at 0.6 and 0.74 seconds because the velocity is higher in the vortex upper zone accumulating mass at its downstream side (see Fig 2.21 - Fig 2.22). As a result, the water column loses its own stability until the moment when the wave breaking process appears ($t = 0.88$ s) (see Fig 2.23). Breaking is occurring in the opposite direction of wave propagation, because the accumulated mass downstream the vortex is taken from

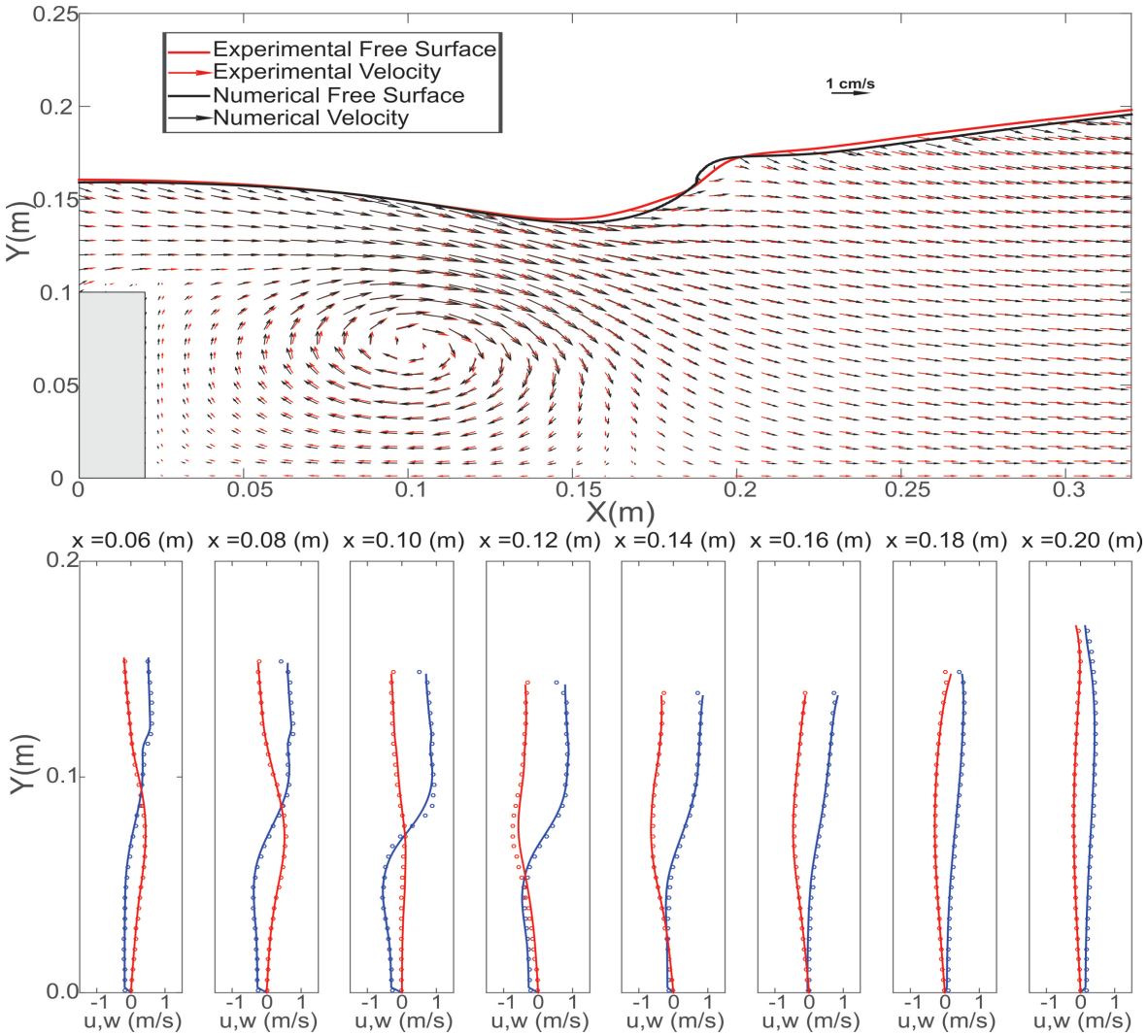

Figure 2.22: Experimental (Wu et al., 2012) and Numerical velocity field comparison (upper panel), and velocity profiles (lower panel) (Blue-horizontal and Red-vertical components) at $t = 0.74$ seconds (before the wave breaking).

the upstream side ($t = 1.02$ seconds)(see Fig 2.23). This simulation gives more information about the crest-crest exchange process, reported by Cooker et al. (1990), where the physical phenomena was studied by using the Euler's equations (without viscous effects) with no vortices in the flow. When the backward breaking wave is present, a new vortex appears and air is trapped in the water (notice that this air entrainment is not capture by the PIV measurements). This vortex interacts with the main vortex (produced by adverse pressure gradient) evolving into an elliptic form without affecting its original direction and magnitude. This implies that the turbulent structure is dominated by the flow separation effects even when the wave breaking processes occurs.

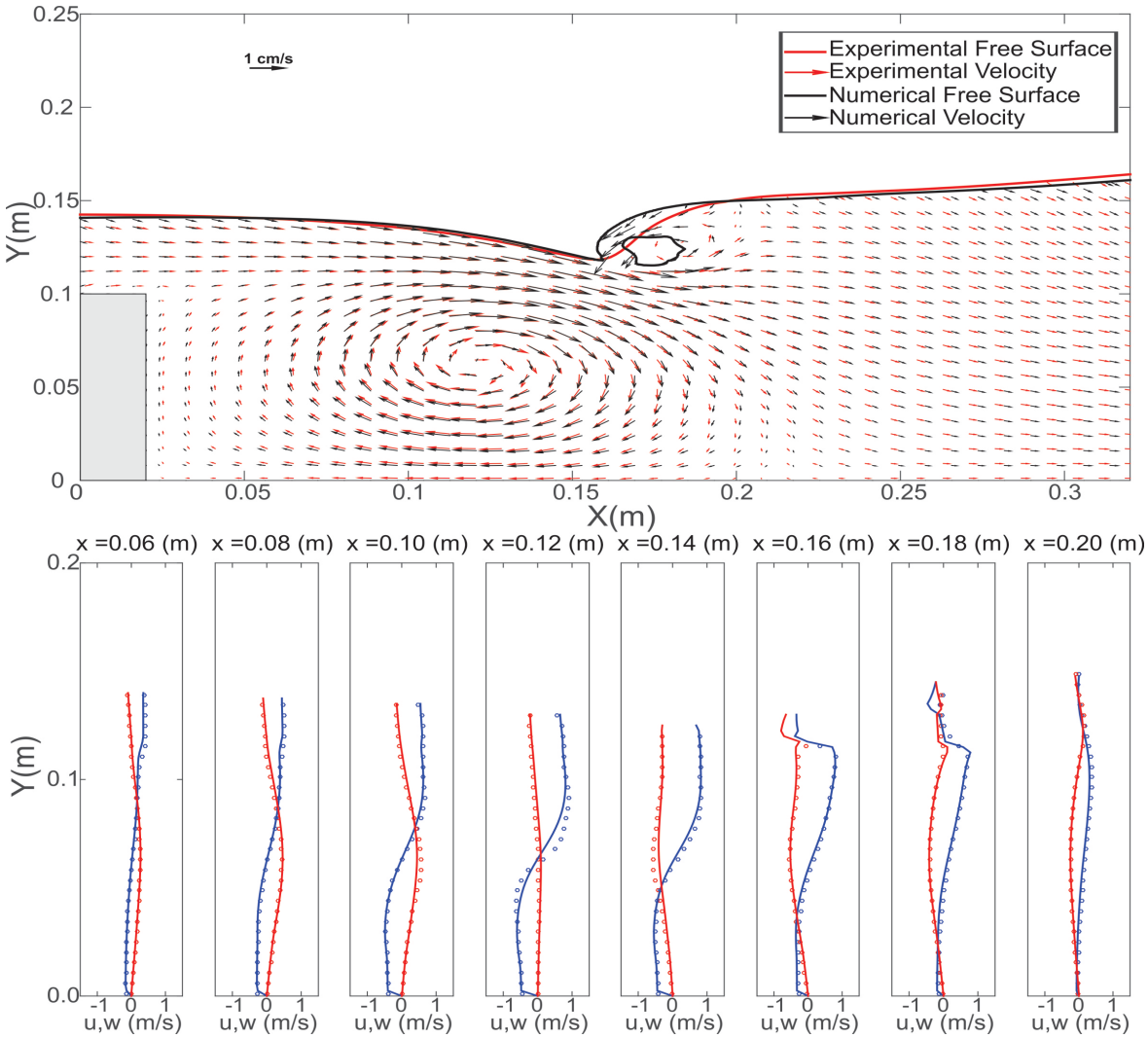

Figure 2.23: Experimental (Wu et al., 2012) and Numerical velocity field comparison (upper panel), and velocity profiles (lower panel) (Blue-horizontal and Red-vertical components) at $t = 0.88$ seconds (at the wave breaking).

2.5 Conclusions

A numerical model implemented in OpenFoam© for dynamic mesh has been presented for wave propagation. The numerical results can be analysed at the same points as the experimental data, eliminating the need to calibrate the numerical incoming wave with the first experimental wave gauge as has to be done with static meshes. The definition of the generation and propagation zones solved the cell deformation problem close to the vicinity of the wave-structure interaction region. The inclusion of the trailing waves in the solitary wave propagation includes a more realistic wave generated by the model. We reiterate here that the properties of the solitary and wave trains are dependent on the generation method according to Katell and Eric (2002).

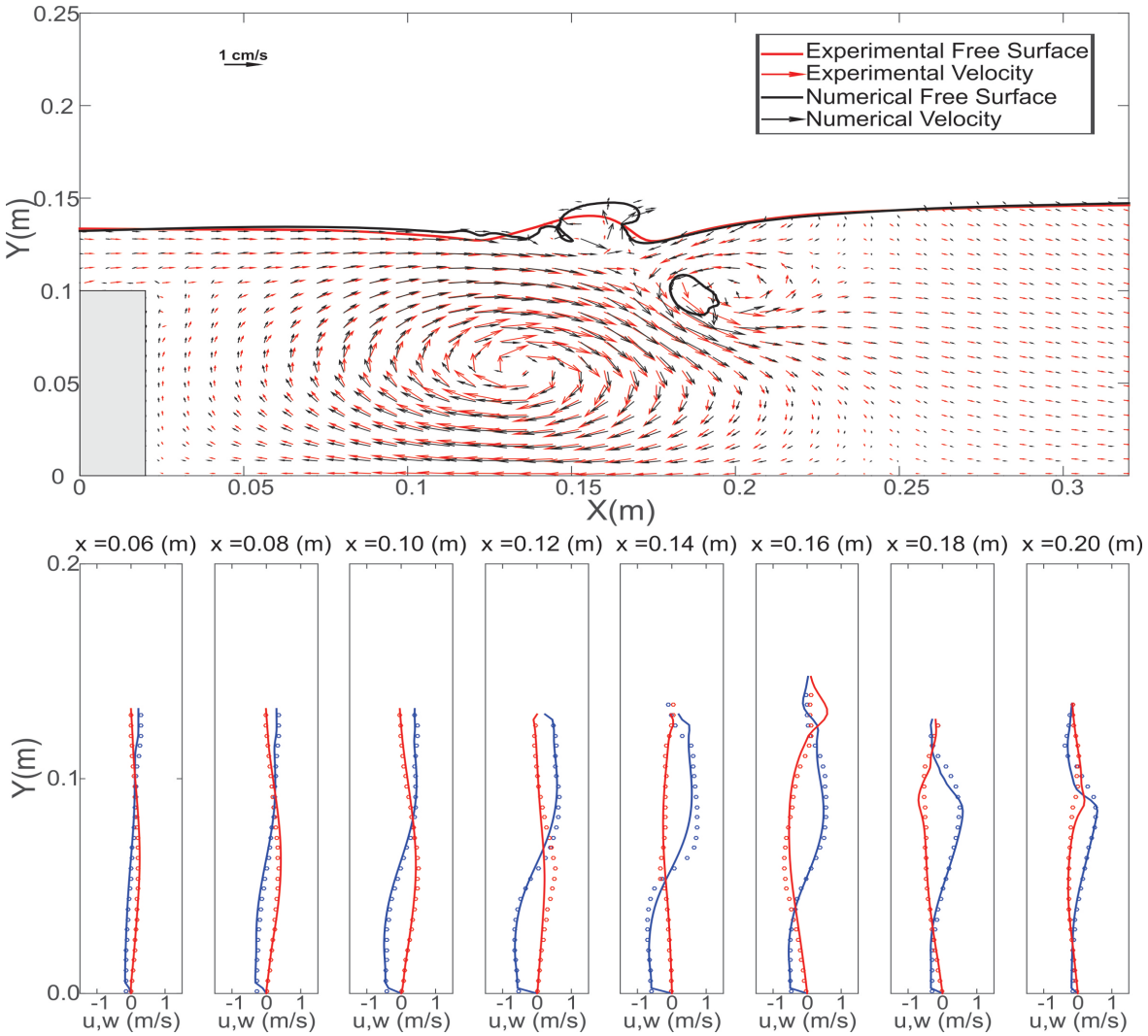

Figure 2.24: Experimental (Wu et al., 2012) and Numerical velocity field comparison (upper panel), and velocity profiles (lower panel) (Blue-horizontal and Red-vertical components) at $t = 1.02$ seconds (at the post-wave breaking).

A special treatment was made for the grid size in a region close to the limits between the paddle stroke in the so-called wave generation zone and at the rigid mesh, the wave propagation zone, since geometric similarity must be preserved between the two areas when defining the computational grid. Additionally, for a solitary wave propagation, a mesh size of $H/40$ was found enough for a correct wave simulation even in wave structure scenario. Regarding monochromatic waves, a vertical mesh size of $H/25$ was enough close to the free surface.

To validate the case of a solitary wave on a flat bottom, the wave generation methods were tested for several discretization schemes of the convective terms. Model results

were compared against the analytical solution for the solitary wave as well as with experimental data. The tests included a solitary wave propagating with slip and non-slip wall conditions. For these cases, the three different discretization schemes, the UD, QUICK and van Leer were compared against the analytical solution for the different wave generation theories. The results showed that the Rayleigh method better fits the analytical solitary wave in terms of the wave amplitude, the smallest wave decay rate and moderate spurious trailing waves. None of the numerical schemes tested had effects on the trailing waves. The QUICK and van Leer schemes adjusted better the analytical solitary wave being the less diffusive schemes.

Regarding the trailing waves, the model results were compared with the experimental data reported by Liu et al. (2006). Numerical results agreed very well with experimental data for the case corresponding to $\varepsilon = 0.409$. The simulated trailing waves were above the measured ones, indicating that the model underestimates the depression produced by the trailing waves once the main wave has passed a certain location. These trailing waves were not affected neither by the fluid viscosity, the bottom friction, the discretization schemes nor by the surface tension. They are directly induced by the wave generation method and modulated by the gravity force. It is worth to note that the numerical wave decay ratio was higher than the obtained in the flume experiments.

When simulating the wave behaviour over a submerged trapezoidal structure, the appearance of higher harmonics were well simulated for the monochromatic wave case, where the trapezoidal obstacle can be seen as a thin plate on the flume bottom due to its small height-length ratio (0.3/11).

Finally, for a solitary wave flowing over a slender submerged column, the comparison between modelled and measured velocity profiles showed that the model represented very well the measuremnts as the maximum error for the velocity profiles was 17%, and that the advection effects were higher than the diffusive ones over the main vortex at the downstream side of the structure. The turbulent flow structure at the submerged solid slender column was dominated by the flow separation effects, even when the wave breaking processes occured. Additionally, the backward breaking wave was not induced by the bottom friction or water depth reduction but it was forced by the effect of the main vortex on the free surface profile; this phenoma explaines in more detail, the crest-crest exchange processes presented by Cooker et al. (1990) and the backward wave breaking.

For future analysis, the effect of the vortex on the structure stability should be studied, since it can undermine the soil that embeds the structure and advecting it by the vortex displacement, inducing a structure overturning.

Chapter 3

Simplified approach to oscillatory flow-submerged canopy

Abstract

A shear layer at the top of a submerged canopy is analyzed under oscillatory flow driven by free surface waves. By applying a dimensional analysis at the shear layer scale, a simple analytical model that reveals the dominant terms in Navier-Stokes equation is developed. A set of laboratory data show good agreement with the analytical model and the assumptions applied in its derivation. The wave-seagrass interaction can be assumed as a horizontal parallel flow, since the mean vertical velocity and the vertical advection can be negligible compared to the mean horizontal velocity and the horizontal advection, respectively. Notable results are that the shear layer thickness (δ) can be approximated as a function of the horizontal orbital excursion (A_w) by $\delta \approx 0.2A_w$. Additionally, the turbulent model parametrization as function of A_w shows good agreement in developing the shear layer, so that the mixing process at the top of the canopy and the development of the horizontal velocity profile are modulated by the horizontal orbital excursion and wave period.

3.1 Introduction

Seagrass ecosystems constitute one of the most diverse and productive environments on Earth (Maxwell et al., 2017). The aquatic vegetation provides a wide range of benefits and ecosystems services; for example, the production of oxygen, the improvement of water quality, the sheltering of important species, and the prevention of shoreline erosion by damping waves and storm surges (Luhar et al., 2010; Ondiviela et al., 2014).

The hydrodynamic impact begins when the seagrass canopy dissipates the incident wave height by following a hyperbolic decay (Kobayashi et al., 1993; Méndez et al., 1999; Losada et al., 2016; Lei and Nepf, 2019), reduces the oscillatory velocity (Abdolahpour et al., 2016), and increases turbulence at stem length scales (Zhang et al., 2018). The wave height attenuation based on field and laboratory observations can reach up to 70% of the incident wave height, depending on the canopy density, length and submergence ratio (Stratigaki et al., 2011; Koftis et al., 2013; Anderson and Smith, 2014; Ondiviela et al., 2014; Karambas et al., 2015). The oscillatory velocity inside the canopy can be reduced up to 40% (compared to a bare bed), presenting a shear layer at the top of the canopy (Ghisalberti and Nepf, 2002) that depends on the canopy density, wave period and wave height (Lowe et al., 2005; Pujol et al., 2013). So the reduction of the flow inside the canopy is a function of the drag length scale (L_{cd}) and horizontal orbital excursion (A_w) (Lowe et al., 2005).

The magnitude of the shear layer in the velocity profile induces a strong vertical mixing (Abdolahpour et al., 2018). This vortex is highly dependent on wave conditions and canopy properties (Ghisalberti and Schlosser, 2013), so that minor changes in forcing can yield major changes in mixing (Abdolahpour et al., 2016).

To understand the canopy-oscillatory flow interaction, Lowe et al. (2005) developed a simplified 2-Box model to analyze the reduction of the mean oscillatory velocity inside the canopy interacting with a very rough surface; Zeller et al. (2015) presented a simplified model to describe the seagrass effects in combined current-waves, solving the vertical advection by assuming linear wave theory. However, the dominant terms behind the shear layer formation, as the drag term, unsteadiness term, Reynolds stresses or the pressure gradient are not yet completely understood and quantified. Additionally, a detailed analysis of the shear layer at the top of the canopy has not yet been presented.

In the present work, a one-dimensional (1D) model for pure wave-seagrass flows, with important applications in coastal protection and ecosystem services, is proposed by analysing the 2D Navier-Stokes equation at the shear layer and horizontal orbital excursion scales. The resulting expression is a function of the local acceleration, horizontal pressure gradient, vertical shear and drag force. Some assumptions reported in the literature were found valid and others did not agree with the analytical and laboratory results.

The paper is structured as follows: In section 2, a dimensional analysis to the 2D Navier-Stokes equation is performed by defining physical reference variables and simplifying the momentum equations. In section 3, the methods used to obtain a set of laboratory data with a seagrass canopy are presented. And finally, in section 4, the laboratory data is used to calibrate and validate the analytical model, and a simple expression to estimate the shear layer is defined.

3.2 1D Model approximation for wave-seagrass interaction

3.2.1 Model Development

In this work a 1D model approximation to a 2D momentum equation is presented. The model starts by assuming that the cross-stream direction is negligible compared to the streamwise (wave propagation axis). So that any cross-stream component is due to the turbulence at the wake scale produced by the canopy stem (not considered in the present development), and the 2D momentum and mass conservation equations for the instantaneous streamwise velocity (u), vertical velocity (w), pressure (p) and constant fluid density (ρ) can be expressed by:

$$\frac{\partial u}{\partial t} + u\frac{\partial u}{\partial x} + w\frac{\partial u}{\partial z} = -\frac{1}{\rho}\frac{\partial p}{\partial x} + \nu\left(\frac{\partial^2 u}{\partial x^2} + \frac{\partial^2 u}{\partial z^2}\right) \tag{3.1}$$

$$\frac{\partial w}{\partial t} + u\frac{\partial w}{\partial x} + w\frac{\partial w}{\partial z} = -\frac{1}{\rho}\frac{\partial p}{\partial z} + \nu\left(\frac{\partial^2 w}{\partial x^2} + \frac{\partial^2 w}{\partial z^2}\right) - g \tag{3.2}$$

$$\frac{\partial u}{\partial x} = -\frac{\partial w}{\partial z} \tag{3.3}$$

where ν and g are the kinematic fluid viscosity and the gravitational acceleration, respectively.

The vegetation interacting with the surrounding wave flow (see the analysis domain, zones R1 and R2 in Figure 3.1) can be assumed to be dense enough that the stem skin friction can be neglected (Kobayashi et al., 1993; Luhar et al., 2017), the canopy resistance is dominated by the drag force and the add mass term is negligible (Ghisalberti and Schlosser, 2013). With this simplification, the presence of the seagrass canopy can be modelled by modifying the Navier-Stokes equations to include the drag force (from the bottom to the top of the canopy) in the momentum equation.

To simplify Eq.(3.1) to Eq.(3.3), a dimensional analysis is performed to identify the dominant terms, so some reference variables are defined: U_∞(the orbital velocity far from the seagrass effects), A_w (horizontal orbital excursion length), T (wave period) and δ (shear layer thickness at the top of the canopy). The dimensionless variables

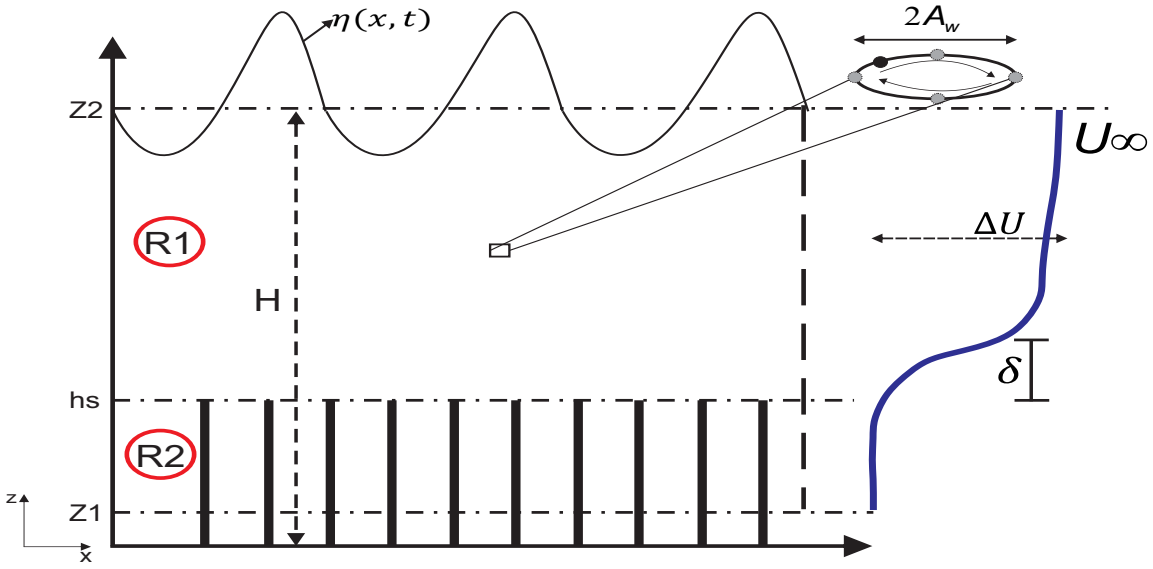

Figure 3.1: Theoretical Seagrass-Wave flow scheme. The blue line is a horizontal velocity profile at a fixed position along the water depth, and hs is the segrass height.

are defined by Eq.(3.4) and substituted in Eq.(3.1) to Eq.(3.3) giving the dimensionless forms Eq.(3.5) to Eq.(3.7). Additionally, by the mass conservation equation, the dimensionless vertical velocity (w^*) in Eq.(3.4), can be scaled as $W_\infty \sim \frac{U_\infty \delta}{A_w}$,

$$u^* = \frac{u}{U_\infty}, w^* = \frac{wA_w}{U_\infty \delta}, p^* = \frac{p}{\rho U_\infty^2}, x^* = \frac{x}{A_w}, z^* = \frac{z}{\delta}, t^* = \frac{t}{T}, g^* = \frac{g}{g} \tag{3.4}$$

$$\frac{A_w}{TU_\infty}\frac{\partial u^*}{\partial t^*} + u^*\frac{\partial u^*}{\partial x^*} + w^*\frac{\partial u^*}{\partial z^*} = -\frac{\partial p^*}{\partial x^*} + \nu\left(\frac{A_w}{U_\infty \delta^2}\frac{\partial^2 u^*}{\partial z^{*2}} + \frac{1}{A_w U_\infty}\frac{\partial^2 u^*}{\partial x^{*2}}\right) \tag{3.5}$$

$$\begin{aligned}\frac{\delta^2}{U_\infty A_w T}\frac{\partial w^*}{\partial t^*} + \frac{\delta^2}{A_w^2}\left(u^*\frac{\partial w^*}{\partial x^*} + w^*\frac{\partial w^*}{\partial z^*}\right) = \\ -\frac{\partial p^*}{\partial z^*} + \frac{\nu\delta}{A_w U_\infty}\left(\frac{1}{\delta}\frac{\partial^2 w^*}{\partial z^{*2}} + \frac{\delta}{A_w^2}\frac{\partial^2 w^*}{\partial x^{*2}}\right) - \frac{g^* g\delta}{U_\infty^2}\end{aligned} \tag{3.6}$$

$$\frac{\partial u^*}{\partial x^*} = -\frac{\partial w^*}{\partial z^*} \tag{3.7}$$

where t, z and x are time, vertical and horizontal coordinates, respectively.

The shear layer thickness should be function of L_{cd} (this will be analysed later); however, in the scaling process, the shear layer is assumed to be of the same order of magnitude as the wave boundary layer. Thus Eq.(3.8) is used in the present development. Additionally, δ is strongly correlated to the mean flow Reynolds number (Re) from laminar to turbulent flow (Jensen et al., 1989; Sana and Tanaka, 2007), and

remarking that for marine canopy environments $Re \sim (O(10^2) - O(10^6))$ (Ghisalberti and Schlosser, 2013; Abdolahpour et al., 2016), simplifications to Eq.(3.5) and Eq.(3.6) can be applied by substituting Eq.(3.8) and Eq.(3.9) into Eq.(3.5) and Eq.(3.6)

$$\delta \sim \frac{A_w}{\sqrt{Re}}, \quad A_w = \frac{U_\infty T}{2\pi} \tag{3.8}$$

$$Re = \frac{U_\infty A_w}{\nu}, \quad Re > 1000 \tag{3.9}$$

where Re is considered large enough to neglect viscous effects.

Finally, Eq.(3.5) and Eq.(3.6) are reduced in dimensionless form to Eq.(3.10) and Eq.(3.11) or in terms of the original variables Eq.(3.1) and Eq.(3.2) to Eq.(3.12) and Eq.(3.13), respectively:

$$\frac{1}{2\pi}\frac{\partial u^*}{\partial t^*} + u^*\frac{\partial u^*}{\partial x^*} + w^*\frac{\partial u^*}{\partial z^*} = -\frac{\partial p^*}{\partial x^*} + \frac{\partial^2 u^*}{\partial z^{*2}} \tag{3.10}$$

$$\frac{\partial p^*}{\partial z^*} = \frac{g^* g A_w}{\sqrt{Re} U_\infty^2} < 1 \tag{3.11}$$

$$\frac{\partial u}{\partial t} + u\frac{\partial u}{\partial x} + w\frac{\partial u}{\partial z} = -\frac{\partial p}{\rho \partial x} + \nu\frac{\partial^2 u}{\partial z^2} \tag{3.12}$$

$$\frac{\partial p}{\partial z} << \frac{\partial p}{\partial x} \tag{3.13}$$

Eq.(3.13) implies that the vertical change of the pressure across the shear layer (δ) is negligible compared to the horizontal one, and hydrostatic pressure formulation was assumed not changing across the shear layer. Any effect by a steady current released by the presence of the canopy (Abdolahpour et al., 2017) is not considered here, since it occurs at a larger temporal and spacial scales. Additionally, inside the shear layer, the vertical gradient of the horizontal velocity is as important as the horizontal pressure gradient and the local acceleration is the least relevant term (by a factor of $(2\pi)^{-1}$) (see Eq.(3.10)). The analysis of the advective terms is introduced later.

Now, applying the Reynolds decomposition for the velocity field ($u = U + u'$, $w = W + w'$) and pressure ($p = P + p'$); assuming that the horizontal scale is much larger than the vertical one (Fletcher, 1987) given the ratio $\frac{\delta}{A_w} << 1$, turbulence and waves do not correlate (Bricker and Monismith, 2007) and averaging in time, the momentum equation takes the form of Eq.(3.14):

$$\frac{\partial U}{\partial t} + U\frac{\partial U}{\partial x} + W\frac{\partial U}{\partial z} = -\frac{\partial P}{\rho \partial x} - \frac{\partial \overline{u'w'}}{\partial z} \tag{3.14}$$

where U and W are the horizontal and vertical wave-induced orbital velocities, respectively. u' and w' are the turbulent velocities.

Additionally, the order of the vertical and horizontal components of the mean advective term can be expressed as,

$$U\frac{\partial U}{\partial x} \sim \frac{U_\infty^2}{A_w}, \quad W\frac{\partial U}{\partial z} \sim \frac{U_\infty^2}{A_w} \tag{3.15}$$

so they can be reduced in one term by:

$$U\frac{\partial U}{\partial x} + W\frac{\partial U}{\partial z} \approx \Gamma U\frac{\partial U}{\partial x} \tag{3.16}$$

Substituting this into Eq.(3.14) and keeping only the horizontal advection term by adding a Γ parameter yields Eq.(3.17)

$$\frac{\partial U}{\partial t} + \Gamma U\frac{\partial U}{\partial x} = -\frac{\partial P}{\rho\partial x} + \frac{\partial \overline{u'w'}}{\partial z} \tag{3.17}$$

The Eq.(3.17) is valid at the horizontal orbital excursion length and orbital velocity scales. This mathematical formulation implies that the seagrass-wave interaction is dominated by the horizontal velocity and the flow can be assumed parallel. Additionally, up to this point the momentum equation in terms of U (the mean flow variable) includes the relative importance of the advective terms by Γ, but in the next subsection a Volume-averaged procedure is applied to approximate the expression $\frac{\partial U}{\partial x} \approx 0$, so we obtain a velocity profile representative at the wave excursion length domain.

Volume-averaged at the particle excursion scale

At the wave excursion particle scale, the horizontal spatial variability of the mean velocity (U) is of the same order of magnitude as the other terms in the transport equation (see Eq.(3.17)); however, it is impractical to account explicitly for this variability over and within the seagrass canopy (Finnigan, 2000). Therefore, a volume average is applied to the horizontal flow heterogeneity to deal with the advective term (Finnigan, 2000; Nepf, 2012; Zeller et al., 2015). This procedure is applied to Eq.(3.17). An averaging volume ($\hat{\mathrm{V}}$) is defined based on Finnigan (2000) and Nepf (2012) to remove the wave excursion-scale heterogeneities. The stem-scale heterogeneities are also averaged by this operation. The dimensions of $\hat{\mathrm{V}}$ are the wave excursion particle A_w and thickness ζ, where A_w was chosen from the dimensional analysis because it is large enough to include several stems, but significantly small compared to changes at the wavelength (λ) scale and canopy length (L) scale. The averaging volume height, ζ, has to be small enough so it does not modify the flow quantity variations at the computational grid scale ($\triangle z$).

The volume-averaging decomposition for any scalar or vectorial field can be expressed as:

$$\psi = \langle\psi\rangle + \psi'' \tag{3.18}$$

where $\langle\rangle$ is the volume-averaged flow quantity and $''$ is the fluctuation from spatial heterogeneity (Finnigan, 2000; Nepf, 2012). This volume-averaging decomposition is applied to the time-averaged variables. Additionally, the averaging expression for time and space derivatives are:

$$\left\langle \frac{\partial \psi}{\partial x} \right\rangle = \frac{\partial \langle \psi \rangle}{\partial x} - \frac{1}{\hat{V}} \iint_{S_t} \psi \vec{n} dS \tag{3.19}$$

$$\left\langle \frac{\partial \psi}{\partial t} \right\rangle = \frac{\partial \langle \psi \rangle}{\partial t} - \frac{1}{\hat{V}} \iint_{S_t} \psi v_i \vec{n} dS \tag{3.20}$$

where S_t is the sum of all stem surface inside $\hat{V}$, $\vec{n}$ is the unit normal vector pointing away from S_t and v_i is the velocity of a point on the stem surface (Raupach and Shaw, 1982). Now, hypothesizing no stem skin friction and no flux through the stem surface area, the momentum equation for volume-averaged velocity comes from replacing Eq.(3.18), Eq.(3.19) and Eq.(3.20) into the Eq.(3.17):

$$\frac{\partial \langle U \rangle}{\partial t} = -\frac{\partial \langle P \rangle}{\rho \partial x} - \underbrace{\frac{\partial \langle \overline{u'w'} \rangle}{\partial z}}_{\text{I}} - \underbrace{\frac{\partial \langle U''W'' \rangle}{\partial x}}_{\text{II}} - \underbrace{f_x}_{\text{III}} \tag{3.21}$$

where term I includes the volume-averaged Reynolds stress $\langle \overline{u'w'} \rangle$ and term II includes the dispersive flux $\langle U''W'' \rangle$ (Finnigan, 2000; Nepf, 2012; Zeller et al., 2015). The term III represents the pressure drag force. Since the vertical gradients are much larger than the horizontal ones, term II is negligible in comparison to term I for $ah_s > 0.1$ (Nepf, 2012; King et al., 2012) and the momentum equation (Eq.(3.21)) reduces to:

$$\frac{\partial \langle U \rangle}{\partial t} = -\frac{\partial \langle P \rangle}{\rho \partial x} - \frac{\partial \langle \overline{u'w'} \rangle}{\partial z} - f_x \tag{3.22}$$

$$f_x = \frac{\Omega(z)}{\hat{V}} \iint_{S_t} P \vec{n} dS = \frac{\Omega(z) C_d a}{2(1-\phi)} \langle U \rangle |\langle U \rangle| \tag{3.23}$$

The pressure drag force (Eq.(3.23)) can be written in terms of a drag coefficient, C_d; a quadratic velocity law, where $|\langle U \rangle|$ is the absolute velocity value; and the solid volume fraction occupied by the canopy elements inside the volume-averaged Lowe et al. (2005), ϕ. Aditionally, as the volume-averageing is applied over the length A_w, the frontal area per unit volume is expressed as $a = \frac{Nd}{A_w}$ $\left[\frac{1}{m}\right]$, N being the number of seagrass elements inside the volume $\hat{V}$ and d the stem diameter. The presence of the seagrass canopy in the water column is included in this equation by using a step function ($\Omega(z)$) with values of 1 (for $0 \leq Z_1 \leq h_s$) or 0 (for $h_s < Z_2 \leq H + \eta$) (King et al., 2012; Singh et al., 2016).

The Reynolds stress tensor is solved by using a Zero-Equation Eddy viscosity model (Eq.(3.24))

$$-\langle \overline{u'w'} \rangle = \nu_t \left(\frac{\partial \langle U \rangle}{\partial z} \right) = Im^2 \left| \frac{\partial \langle U \rangle}{\partial z} \right| \left(\frac{\partial \langle U \rangle}{\partial z} \right) \tag{3.24}$$

where Im is the mixing length scale and ν_t the eddy viscosity.

Boundary conditions and Numerical solution

The effect of the atmosphere and sea-bed are negligible in comparison to the drag force exerted by the seagrass, therefore, close to the free surface and on the sea bottom, the vertical gradients can be neglected $\left(\frac{\partial}{\partial z} \approx 0\right)$ (Tanino and Nepf, 2008; Singh et al., 2016). Additionally, by studying non-wave breaking scenarios ($\frac{H_w}{h} < 0.7$) and using the mean horizontal velocity expression for shallow water regions ($U_\infty = \frac{CH_w}{h}$), the particle excursion is always much smaller than the wavelength ($A_w < 0.1\lambda$); where H_w is the wave hight, h the still water depth and C the wave phase speed. So the boundary conditions for the horizontal velocity at $z = 0$ and $z = h$ can be obtained by a numerical solution (a Runge-Kutta method, for example) of Eq.(3.25) and Eq.(3.26), respectively, as function of the wave passing over the seagrass:

$$\frac{\partial \langle U \rangle}{\partial t} = -\frac{\partial \langle P \rangle}{\rho \partial x} = -g\frac{\partial \eta}{\partial x} \tag{3.25}$$

$$\frac{\partial \langle U \rangle}{\partial t} = -g\frac{\partial \eta}{\partial x} - f_x \tag{3.26}$$

Additionally, replacing the pressure gradient (Eq.(3.25)) in Eq(3.22) gives Eq.(3.27)

$$\frac{\partial \langle U \rangle}{\partial t} = -g\frac{\partial \eta}{\partial x} - \frac{\partial \langle \overline{u'w'} \rangle}{\partial z} f_x \tag{3.27}$$

From now on for simplicity in reporting and presenting results, the variables will be redefined as: $\langle U \rangle = U$ and $\langle \overline{u'w'} \rangle = \overline{u'w'}$.

Finally, the 1D model in this section (Eq.(3.27)) solves a volume-averaged velocity profile at the wave excursion scale. The governing equation shows that the vertical mass exchange is a function of the shear layer at the top of the canopy. This conclusion achieved by this model agrees with the experimental work for several wave excursion values reported by Abdolahpour et al. (2016) and Abdolahpour et al. (2018).

3.2.2 Drag coefficient estimation

The drag force exerted by the seagrass in the momentum equation (Eq.(3.27)) is highly dependent on the drag coefficient. For oscillatory flows the drag coefficient has been fitted by using the Reynolds number ($Re_d = \frac{Ud}{\nu}$) (Kobayashi et al., 1993; Bradley and Houser, 2009; Koftis et al., 2013), where U is the maximum orbital velocity above the seagrass and d is the diameter of the stem. However, in recent research the Keulegan-Carpenter number ($KC_d = \frac{UT}{d}$) has been applied (Luhar and Nepf, 2016; Luhar et al., 2017), since for oscillatory flows the wave excursion-stem diameter (or drag scale) ratio has to be taken into account. In the present work, the C_d is estimated as function of

KC_d number in Figure 11 for cylinders in Keulegan and Carpenter (1958), these values show good agreement at individual blade scale (Lei and Nepf, 2019). It is important to remark that the inertial force can be neglected since KC_d is larger than one for all the experiments (Luhar and Nepf, 2016) (see section Methods).

3.3 Methods

In order to validate the model and all the assumptions presented in this work, a set of velocity time series were recorded in a pure-wave environment experiments in the Civil and Environmental engineering department at the University of California-Berkeley. The wave tank is 30 m long, 1.8 m high and 0.45 m wide, with a flap type wavemaker system (Figure 3.2).

In typical field conditions, ϕ is between $1\%-10\%$ (Luhar et al., 2010), and a between $1m^{-1} - 100m^{-1}$ (Nepf, 2012). The experiments were ran by using a random seagrass canopy distribution with two different density values (Low and $Medium$) based on the classification by Ghisalberti and Schlosser (2013) and Abdolahpour et al. (2016) (Table 3.1). The canopy was made of plastic elements that are 25 cm high, the diameter of the stem 12 mm, and six different wave conditions for each seagrass canopy were simulated (Table 3.2). To avoid any edge effect by the canopy, the stems are mounted on an acrylic plate of 1.2m length, to have a seagrass canopy length larger than $2A_w$ for all the experiments (Abdolahpour et al., 2016). The canopy was always in the shallow submerged region ($h/h_s \approx 2$) (Nepf, 2012), using a false bottom and a still water level of 50 cm (see Figure 4.2). All the simulated waves were in the intermediate water wave condition ($11 < \lambda/h < 26$), where λ is the wavelength. The reflection coefficient was estimated by using $C_r = \frac{I_r^2}{5.5+I_r^2}$ (Nejadkazem and Gharabaghi, 2008), giving values below 10% for all the wave conditions. I_r is the Iribarren number at the beach.

Table 3.1: Seagrass Canopy geometric set-up. $\triangle S$ is the average spacing between stems.

$Density$	$a[m^{-1}]$	$\phi[\%]$	$\triangle S[m]$
Low	5.0	4.8	0.05
$Medium$	8.0	7.6	0.04

A Nortek Acoustic Doppler Velocimeter (ADV) was used starting at 12 cm above the bottom up to the free surface (depending on the wave height) to measure the velocity at different vertical positions. 14 recording locations (7 inside and 7 above the canopy) separated 2 cm and a sampling interval of 10 minutes at 25 Hz were performed. The signal was filtered by using a Signal Noise Ratio (SNR) and Correlation values

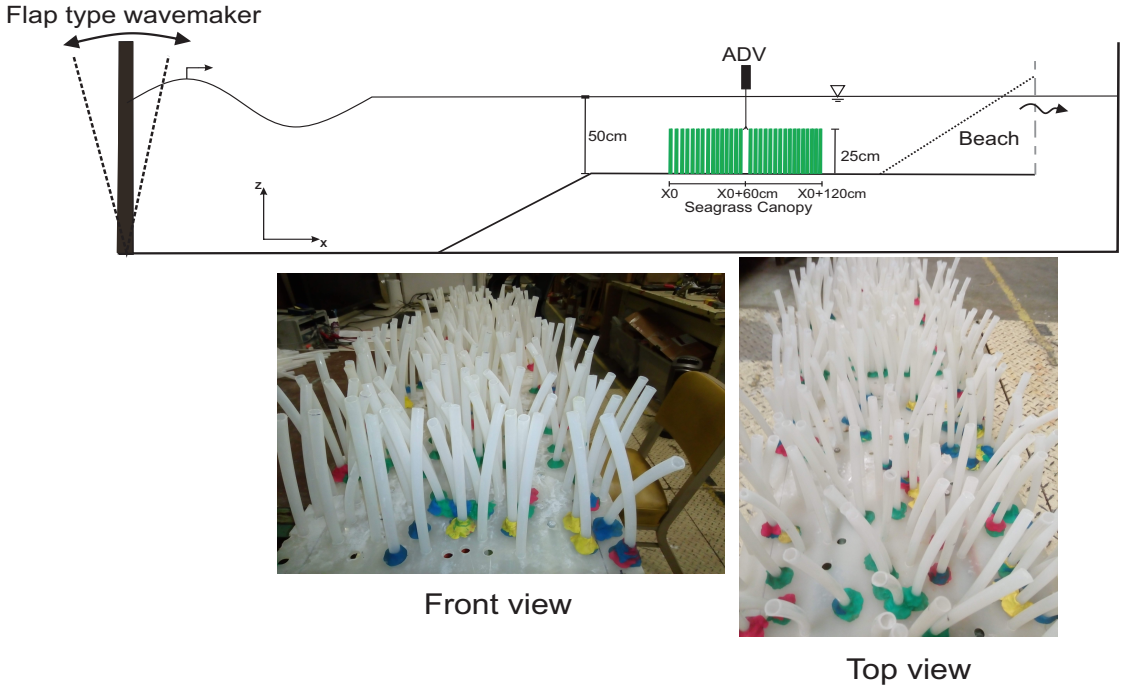

Figure 3.2: Experimental setup, ADV position, and frontal and top view of the random seagrass canopy.

of 30 dB and 95%, respectively. To apply the filter, the averaged values for SNR and Correlation at every recording station were estimated and the data below the mean value minus twice the standard deviation (Pujol et al., 2013) were replaced by a cubic fitting (Rusello et al., 2006; Chanson et al., 2008). The despike method proposed by Goring and Nikora (2002) was also applied to the filtered data.

To obtain a velocity profile for a specific wave condition, the phase-averaged method was used (Lowe et al., 2005; Pujol et al., 2013; Abdolahpour et al., 2016). This method is based on the fact that the instantaneous velocity in a wave environment can be decomposed in steady (U_c), oscillatory (U_w) and turbulent ($u^{'}$) components:

$$u_i = U_c + U_w + u^{'} \tag{3.28}$$

To determine the oscillatory term to analyse the wave seagrass interaction (U_w), the Hilbert transform is applied to the time series and the velocity record is transformed to the phase domain (φ) between $[-\pi\ \pi]$. The data were grouped into common phases (91 phase bins) to calculate the phase-averaged statistics (Pujol et al., 2013; Abdolahpour et al., 2016) (see Figure 4.3). The steady component U_c can be defined by Eq.(3.29). The turbulent component is estimated by the difference between the instantaneous, steady, and the oscillatory velocities.

Table 3.2: Experimental scenarios for two different seagrass densities and 12 mm stem diameter. L and M stand for low and medium density, respectively. ($KC = \frac{UT(aC_d)}{1-\phi}$).
.

$Name$	$T[s]$	$U_\infty[\frac{cm}{s}]$	$A_w[cm]$	KC	Re	KC_d	C_d
$L1$	3	16.8	8	3.7	13508	42.1	1.4
$L2$	4	10.0	7	3.3	7305	37.9	1.4
$L3$	4	23.0	16	6.8	36345	83.2	1.3
$L4$	5	16.8	15	6.3	24764	77.1	1.3
$L5$	5	18.8	16	6.8	29822	83.3	1.3
$L6$	6	16.1	16	7.0	26395	86.1	1.3
$M1$	3	15.9	7	5.0	10889	35.9	1.4
$M2$	4	13.3	8	6.2	11227	44.3	1.4
$M3$	4	16.3	12	8.5	19523	62.6	1.3
$M4$	5	17.2	13	9.5	23015	69.9	1.3
$M5$	5	13.4	11	8.2	15340	60.1	1.3
$M6$	6	15.8	15	10.3	23748	78.9	1.3

$$U_c = \frac{1}{2\pi}\int_{-\pi}^{\pi} u_i(\varphi)d\varphi \tag{3.29}$$

In order to compare the analytical oscillatory velocity profile against the measurements, the root mean squared velocity for the horizontal and vertical components was estimated in the phase domain (U_w^{rms} and W_w^{rms}) by using Eq.(3.30) (Lowe et al., 2005; Abdolahpour et al., 2016)

$$U_w^{rms} = \sqrt{\frac{1}{2\pi}\int_{-\pi}^{\pi}(U_w(\varphi) - U_c)^2 d\varphi} \tag{3.30}$$

Finally, since a statistical value does not provide enough information about the model performance when a comparison between the measurements and numerical data along the water column is performed, an Interquartile range (IQR) combined with the Bootstrapping method were applied to estimate the 95% confidence interval. The Bootstrapping method generates enough resampled data to ensure that the $Median$ and the $Mean$ are the same in the probability distribution (Singh and Xie, 2003). Later, the $Median$, Q1 (25%) and Q3 (75%) values were obtained and IQR = Q3 - Q1.

3.4 Results

The equation presented in the present work (see Eq.(3.27)) can be used to solve the vertical profile of the mean horizontal velocity during a wave period; however, the

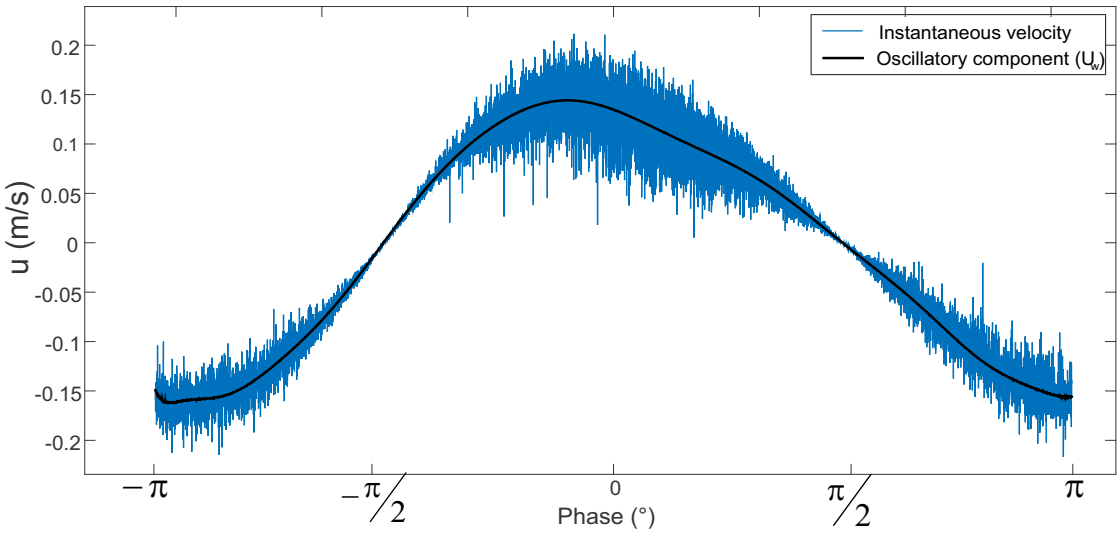

Figure 3.3: Comparison between the instantaneous velocity and phase-averaged oscillatory velocity.

data to validate the statements and assumptions are from an ADV device. So it is not possible to measure along the recording stations simultaneously and a statistical quantity has to be used for the model validation. The *rms* value of the horizontal and vertical oscillatory velocities, and horizontal orbital excursion was estimated in order to determine the *rms* shear layer thickness. The assumptions to develop the model are validated for *Low* and *Medium* densities; and finally, the analytical model is compared to velocity profile for both densities.

3.4.1 Validating the Assumptions

The assumptions to validate are:

$$(a) \quad W_w \sim \frac{\delta}{A_w} U_{w\infty} \quad \rightarrow \quad W_w^{rms} \sim \frac{\delta^{rms}}{A_w^{rms}} U_{w\infty}^{rms}$$

$$(b) \quad W_w \frac{\partial U_w}{\partial z} \sim \frac{U_{w\infty}^2}{A_w} \quad \rightarrow \quad W_w^{rms} \frac{\partial U_w^{rms}}{\partial z} \sim \frac{U_{w\infty}^{rms^2}}{A_w^{rms}}$$

where $A_w^{rms} = \frac{TU_{w\infty}^{rms}}{2\pi}$ and δ^{rms} are the root mean squared horizontal orbital excursion length and shear layer thickness, respectively. δ^{rms} represents a typical shear layer thickness problem not bounded by solid walls (Wilcox, 2006) (see Figure 4.4). It is important to remark that the *rms* velocity profiles from the numerical model were estimated by the same method as for the experimental data, solving the momentum equation in time and estimating U_{model}^{rms} at the recording depths levels.

To validate the assumptions (a), the ratio between the mean vertical and horizontal components of the oscillatory velocity is estimated (Figure 4.5), showing that at the top

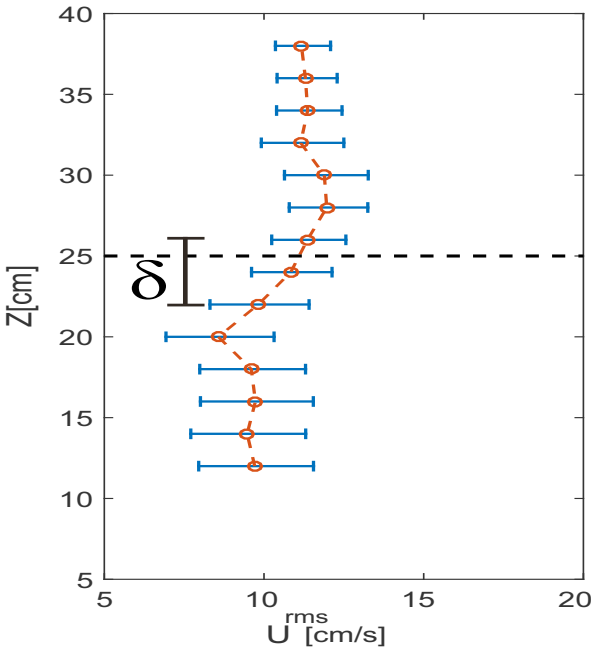

Figure 3.4: Root mean square horizontal velocity profile and shear layer thickness definition.

of the canopy (a) is centered around 0.2 for all the wave scenarios with some peaks for short wave periods, but always lower than 0.35 ($L1$, $L3$ and $M1$), so $\delta^{rms} \approx 0.2A_w^{rms}$. This result is similar to the solution presented by Wilcox (2006) for mixing layers in flows not bounded by solid walls. However, as the data are recorded each 2 cm (same order of magnitude as A_w) and δ is expected to be function of L_{cd}, a scaling analysis relating the mixing time scale by the shear layer (t_{KH}) and the horizontal orbital excursion time scale (t_w) is performed in order to verify the relationship between A_w and δ. The variables are defined by $t_{KH} \sim \frac{L_{cd}}{u_*}$ and $t_w \sim \frac{A_w}{U_\infty}$. $L_{cd} \sim \frac{1}{aC_d}$ and the friction velocity (u_*) at the top of the canopy can be scaled as:

$$u_*^2 \sim \nu_t \frac{U_\infty}{\delta}, \quad \nu_t \sim I_m^2 \frac{U_\infty}{\delta} \tag{3.31}$$

where $I_m \sim O(10^{-2})$ (see the turbulent closure model in the next section), $L_{cd} \sim O(10^{-1})$, and $O(t_{KH}) \sim O(t_w)$ based on the experimental work by Abdolahpour et al. (2018), then $\Phi = \frac{t_{KH}}{t_w} \sim O(10^0)$, so δ can be expressed as:

$$\delta^2 \sim \frac{U_\infty^2 I_m^2 t_{KH}^2}{L_{cd}^2} = \frac{t_{KH}^2 I_m^2 A_w^2}{t_w^2 L_{cd}^2} \tag{3.32}$$

$$\delta \sim \frac{\Phi I_m A_w}{L_{cd}} = 10^{-1} A_w \tag{3.33}$$

As can be observed in Eq.(3.33), there is an agreement between the validation of assumption (a) and the scaling process regarding the relationship between δ and A_w.

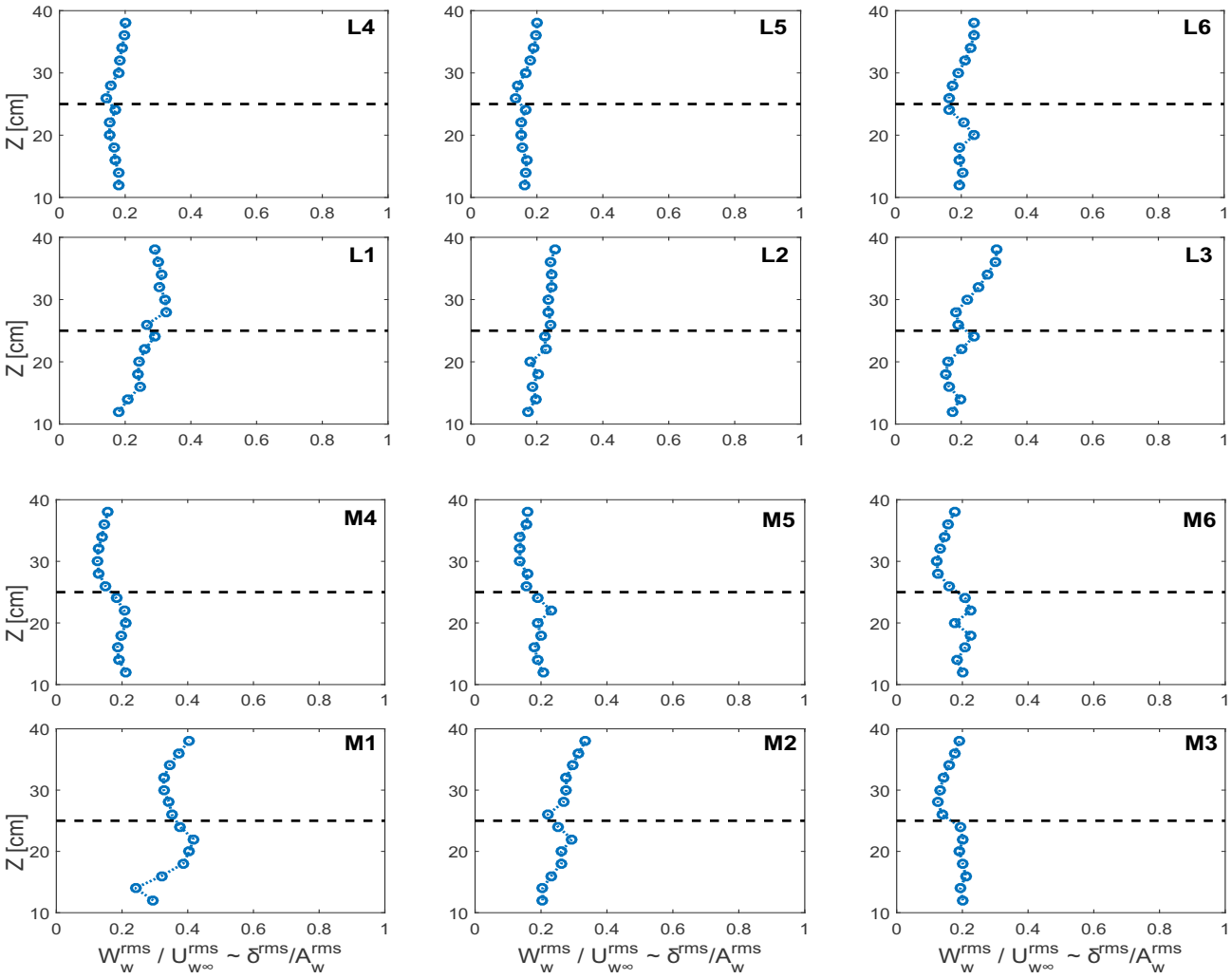

Figure 3.5: δ^{rms}/A_w^{rms} along the water column for *Low* and *Medium* density canopy. Dashed line is the Canopy Top.

Also, the shear layer thickness is function of L_{cd} but $\delta \approx 0.2A_w$ is a valid approximation.

To validate (b), the analysis of the advective terms shown in Eq.(3.15) to Eq.(3.16) implies that the advection is dominated by the horizontal component. So to prove this assumption, the $\frac{\sigma}{\Theta}$ ratio is calculated expecting a value smaller than 1. σ is the *rms* vertical advection and Θ is the *rms* of the order of magnitude of the horizontal advection (see Eq.(3.34)).

Based on the experimental data shown in Figure 3.6, the σ/Θ ratio at the top of the canopy is centered around 0.1 with some peaks for short wave periods, but always lower than 0.18 ($L1$, $L3$ and $M1$). This implies that the horizontal advection is around 90% larger than the vertical advection, and the flow can be assumed parallel and horizontal, so that the simplification made in Eq.(3.17) before the volume-averaged procedure is

valid. Additionally, any effect on the flow by the vertical advection can be negligible compared to the horizontal advection, a contradictory argument to the formulation by Zeller et al. (2015), who assumed that the vertical advection is an important component in the momentum equation.

In summary the assumptions (a) and (b) are valid for the development of the present model.

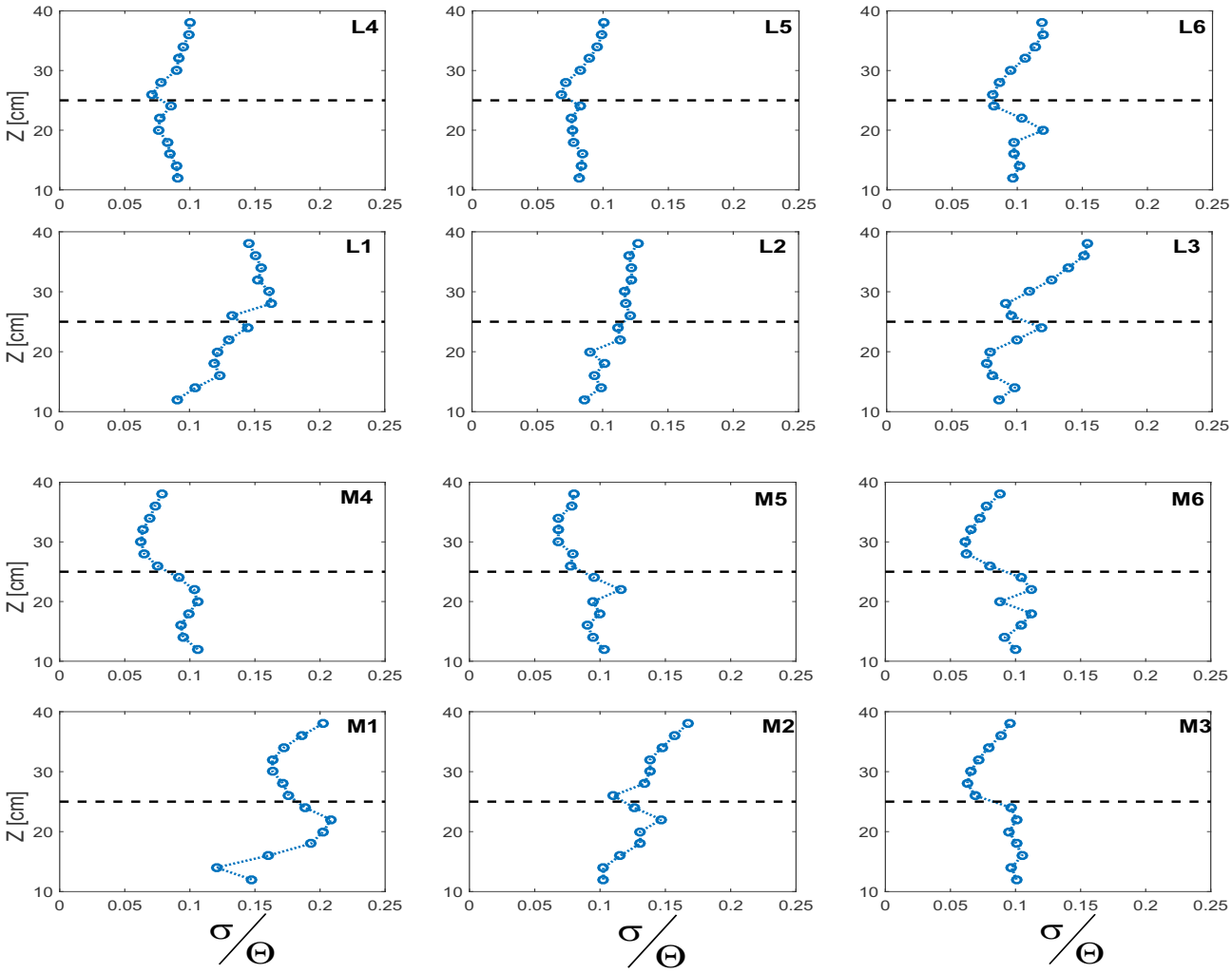

Figure 3.6: σ/Θ along the water column for *Low* and *Medium* density canopy. Dashed line is the Canopy Top.

$$\sigma = W_w^{rms} \frac{\partial U_w^{rms}}{\partial z}, \Theta = \frac{U_{w\infty}^{rms^2}}{A_w^{rms}} \tag{3.34}$$

3.4.2 Validation of the model

To validate the model, a comparison between the *rms* oscillatory velocities from the experimental and numerical values was done. Initially, two important aspects have to be taken into consideration: 1) the parametrization of the drag coefficient as a function of the vertical position ($C_d = C_d(z)$); and 2)the solution for mean horizontal velocity by using a mixing model. In general, for wave-seagreass interaction at laboratory and field studies, a constant drag coefficient in the vertical axis is assumed; however, Ghisalberti and Nepf (2004) and Zampogna et al. (2016) showed that for steady flows there is an important change in the drag value as a function of z and can be expressed by:

$$C_d(z) = C_d \begin{cases} 1.4\left(\frac{z}{hs}\right)^{2.5} + 0.45\ , & 0 \leq \frac{z}{hs} < \beta \\ -4.8\left(\frac{z}{hs}\right) + 4.8, & \beta \leq \frac{z}{hs} < 1 \end{cases} \tag{3.35}$$

where C_d is shown on Table 2.2 for all the wave scenarios, and the maximum $\overline{u'w'}$ in the vertical axis was used to define β. $\overline{u'w'}$ is the time-averaged Reynolds stress. Figure 3.7 shows the $\overline{u'w'}$ profile for $L2$, $L4$ and $L5$, being β between [0.88 0.96] and outside this region $\overline{u'w'}$ approaches to zero. This interval was considered narrow enough so that β is set on 0.92.

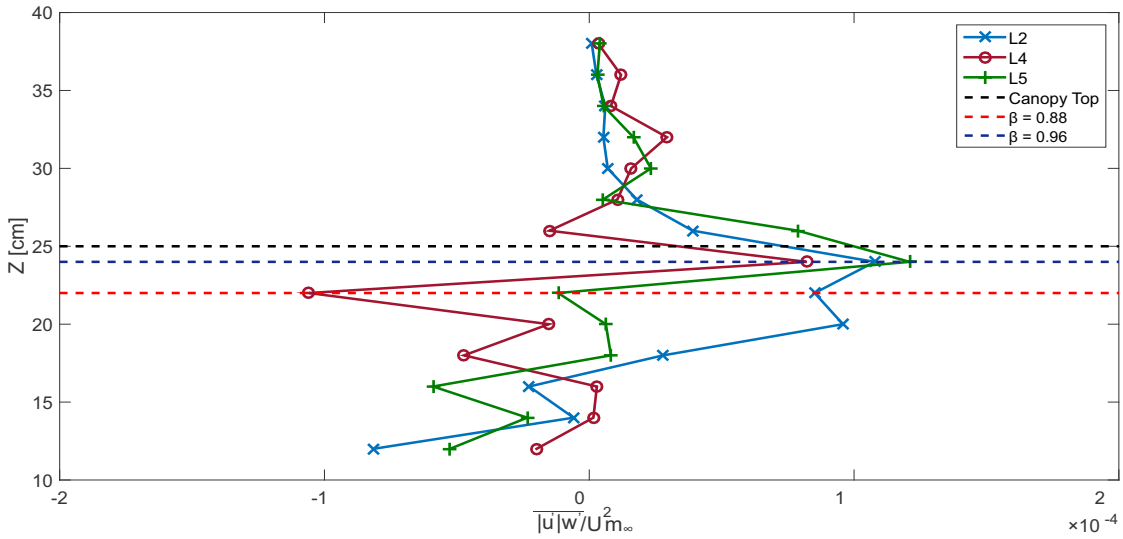

Figure 3.7: $\overline{u'w'}$ profile for three characteristic wave conditions with *Low* density canopy. The blue and red dashed lines indicate the location of β.

Regarding the numerical simulations, the incoming wave height was estimated from the velocity time records (Figure 3.8-panel I), and the mean horizontal velocity profile was solved by using linear wave theory at the free surface (Figure 3.8-panel II) (the linear wave theory appeared to predict the velocities in the whole intermediate water depth range (Hedges, 1995)); later, the U^{rms}_{model} was estimated (Figure 3.8-panel III). For the turbulent closure model (Eq.(3.24)), the mixing length parameter can be estimated

as a function of δ (Rodi, 1993), $Im = 0.07\delta$, or with $Im = 0.14A_w$. Thus in oscillatory flows, the mixing process is modulated by a finite horizontal particle displacement magnitude (A_w), while in steady flow the particles have more time and space to develop the velocity profile. Additionally, Im is assumed constant on the water column.

In Figure 3.8-panel II, it was possible to observe that the model is able to reproduce the shear layer at the top of the canopy; additionally, the numerical simulation presents a lag between the mass of water above and inside the canopy. This lag is produced by a reduction of momentum by the stems on the flow (drag force) and a constant diffusion of momentum by the diffusive term in the governing equation (*Stokes' second problem* (Kundu et al., 1990)).

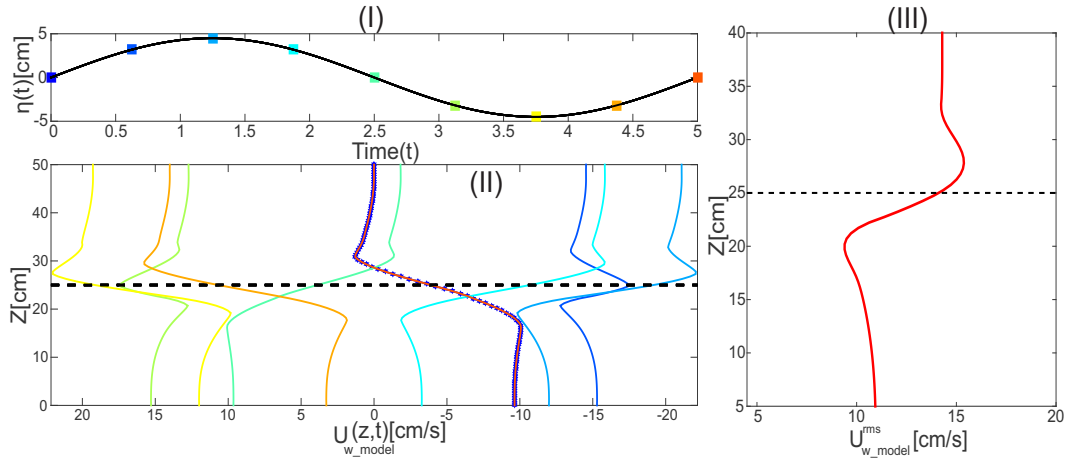

Figure 3.8: Free surface record (I), horizontal velocity profile at different time values (II), *rms* velocity profile (III) calculated from (II).

Finally, the validation of the model is shown in Figure 3.9 and Figure 3.10, where the model shows a good general agreement with the experimental data and most of the simulated velocity profiles are inside the confidence interval (C.I.) of the experimental data. Additionally, the horizontal velocity profile above and at the top of the canopy is in a better concordance compared to the profile in the canopy.

Concerning the results inside the canopy, the biggest discrepancies against the experimental data are presented for $L3$, $L5$ and $M5$. The model predicts the position of the maximum drag coefficient around 2 cm below the laboratory data and overestimates the magnitude. The constant drag coefficient formulation seems to have a better response for these cases. For $L1$, $L2$, $L4$, $L6$, $M2$, $M4$ and $M6$ not only the velocity profile above the canopy is well reproduced but also the flow inside the canopy has a good concordance with the measurements. Additionally, it seems that a constant drag coefficient formulation has a better response for cases with $KC > 7$ and $Re > 23000$. For Re <23000, the drag coefficient as a function of z fits better the measurements

and $\beta = 0.92$ is a good estimation.

3.5 Conclusions

By scaling analysis, a simplified one-dimensional horizontal model was developed. This simplified model has applications on large scale models for coastal protection and ecosystem services not only on seagrass ecosystems but also on submerged structures with known geometry and spatial distribution.

The laboratory data shows that the mean vertical velocity is around 20% of the mean horizontal velocity and the vertical advection is 10% of the horizontal one, supporting the assumptions to develop the model. Additionally, the seagrass-wave interaction can be assumed as a horizontal parallel flow, and the shear layer thickness can be approximated by $\delta \approx 0.2A_w$.

During the scaling process it was possible to determine the dominant terms in the momentum equation, being these, the horizontal pressure gradient, horizontal advection, the vertical gradient of the horizontal velocity, the drag force by the seagrass and the local acceleration. Two important differences were found in this work, compared to the work by Zeller et al. (2015): 1) the local acceleration is the least dominant term in the momentum equation (see Eq.(3.10)); and 2) the vertical advection can be negligible compared to the horizontal one. Also, the analytical model solves the horizontal velocity profile by using the free surface wave, and the developed model by Lowe et al. (2005) solves the depth-averaged velocity from the freestream velocity.

The model is valid for cases when the shear layer is present, but the horizontal orbital excursion length has to be larger than the stem spacing. Additionally, the model needs to be tested for sparse canopies, where the bottom friction is important and the shear layer is not present.

No documentation or publications were found regarding the behaviour of dispersive fluxes in oscillatory flow. The $ah_s > 0.1$ threshold (Nepf, 2012) for steady flows does not take into account the finite horizontal particle displacement in oscillatory flows (A_w). The discrepancies between the measurements and numerical results are attributed to spatial heterogeneities and wake scale turbulence processes by the stems, since the mixing model reproduces the shear layer, but some velocity gradients are observed inside the canopy. Additionally, experimental work has to be done on trying to measure the spatial heterogeneities in oscillatory flow scenarios and its relation with A_w. Also, a possible source of error could be the assumption of linear theory on the free surface, and by using a recorded free surface the velocity profiles can be improved.

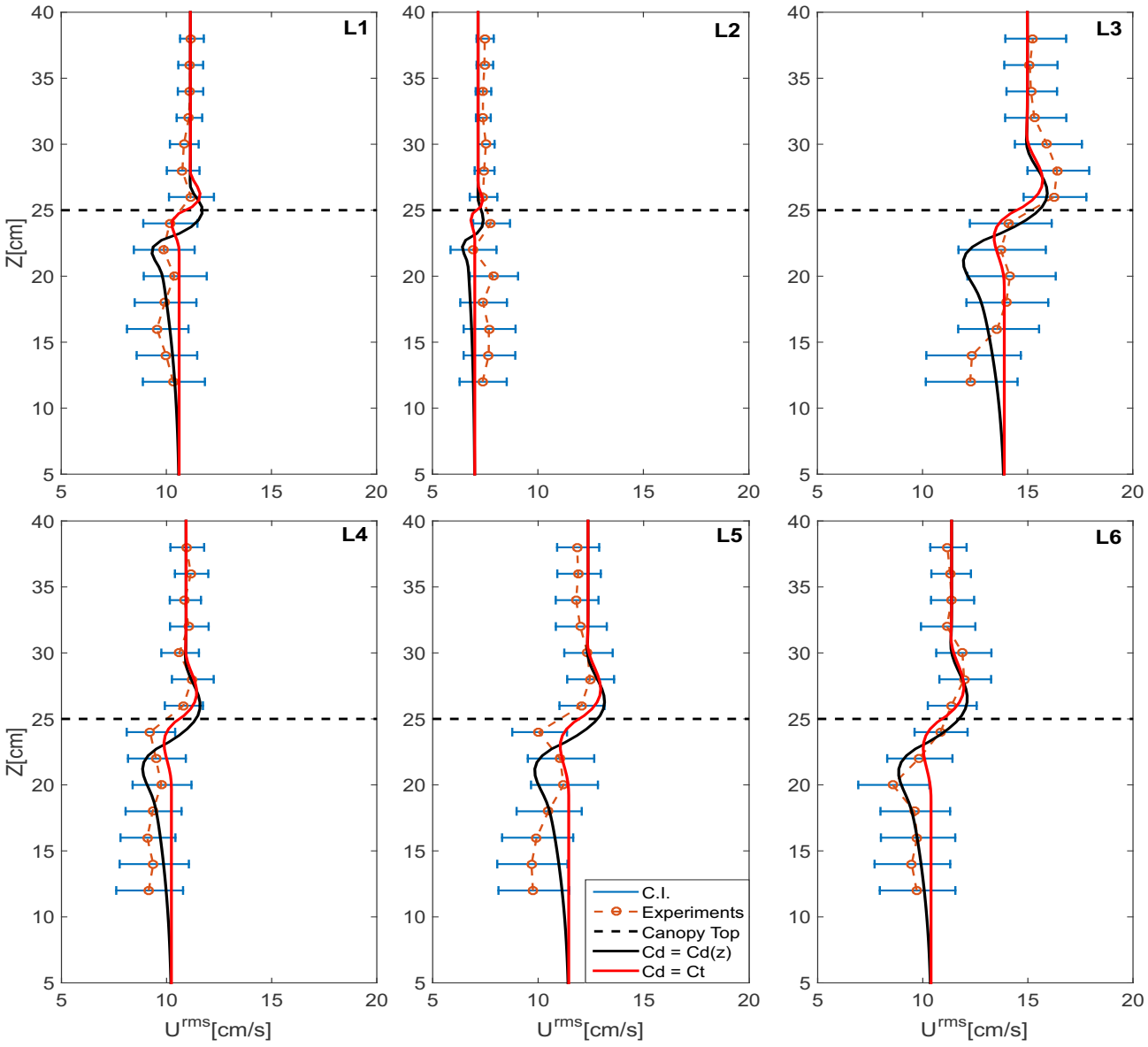

Figure 3.9: Experimental and simulated oscillatory component of the horizontal velocity profiles for *Low* density canopy. The blue line is the confidence interval.

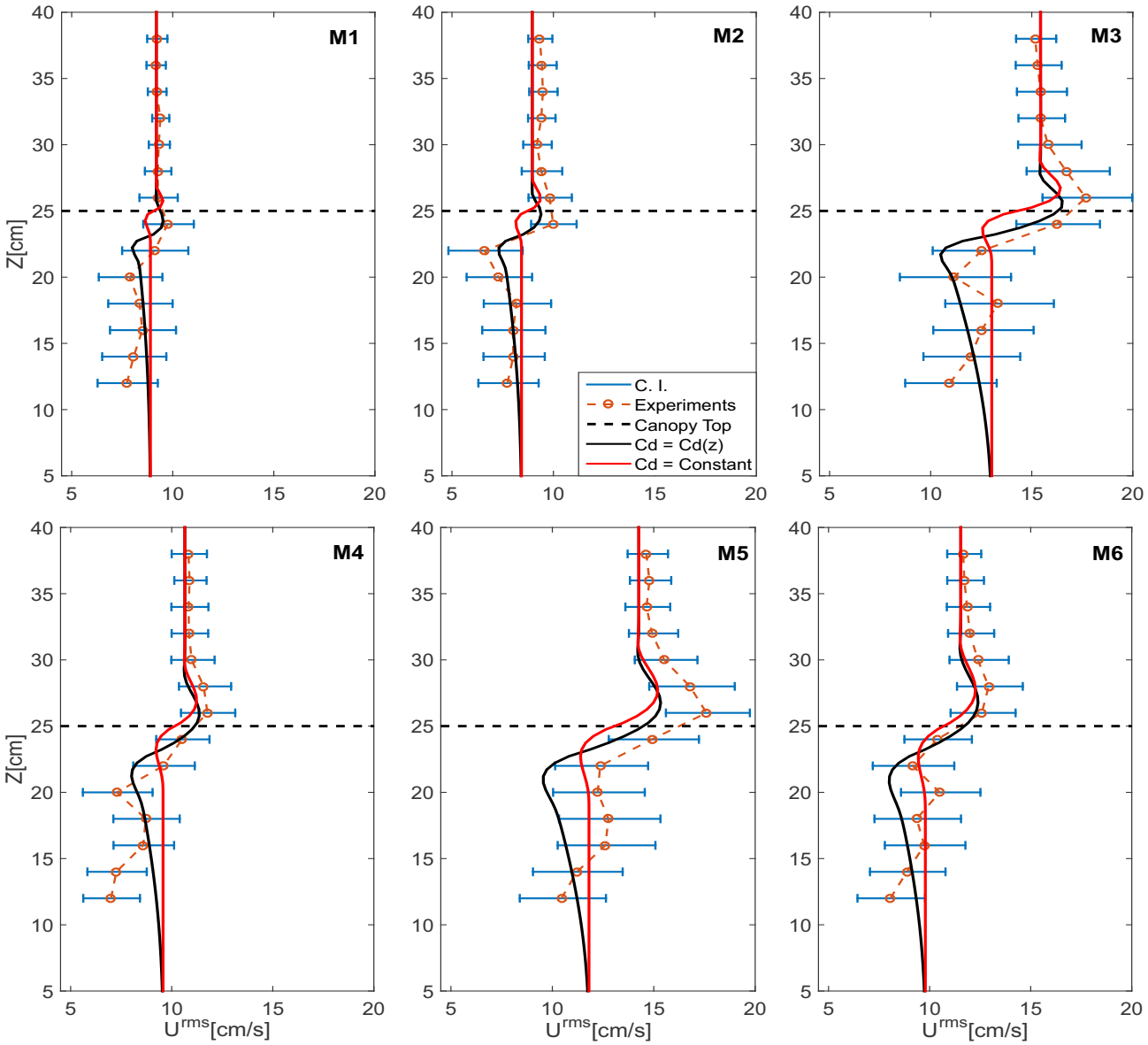

Figure 3.10: Experimental and simulated oscillatory component of the horizontal velocity profiles for *Medium* density canopy. The blue line is the confidence interval.

Chapter 4

Piecewise linear method for Kelvin-Helmholtz solution in seagrass-oscillatory flow interaction

Abstract

A theoretical solution for the Kelvin-Helmholtz instability (KH) over submerged canopies is presented. The method linearises the vertical velocity profile in the seagrass-oscillatory flow applying the piecewise linear method, together with the Kelvin's circulation theorem. Results show that the frequencies of the KH instabilities are higher than those from the incident free surface wave and they can be expressed by $f_{KH} \approx 4f_w$. Additionally, the turbulent spectrum of the Reynold stress ($S_{u'w'}$) show cases where the wake scale is the dominant turbulent production mechanism (even when the KH is present in the flow) and other where the KH is the main source of turbulent production. For $>$18000 and $KC >$20, the KH is the dominant turbulent production mechanism, and for $<$7500 and $KC <$12 the wake scale is the dominant process.

4.1 Introduction

The aquatic vegetation is a highly valuable ecosystem that play important ecological services in coastal protection (Ondiviela et al., 2014). It contributes to coastal resilience by protecting the coastal land by wave dissipation mechanisms (Foster-Martinez et al., 2018; Tinoco and Coco, 2018). The wave height dissipation can reach up to 70% of the incident wave, depending on the seagrass canopy density, coverage, blade height and submergence ratio (Anderson and Smith, 2014; Pinsky et al., 2013; Bradley and Houser, 2009; Foster-Martinez et al., 2018).

The presence of the seagrass attenuates the oscillatory velocity within the canopy (Lowe et al., 2005), and generates a shear layer at the top of the canopy (Ghisalberti and Nepf, 2002). The presence of the shear layer induces a strong vertical mixing across the top of the canopy (Abdolahpour et al., 2018) and modulates wave-induced currents at the top of the canopy in the shoreward direction (Abdolahpour et al., 2017), that can be in charge of sediment transport. This shear layer induces a mass and momentum transfer that is governed by the presence of Kelvin-Helmholtz-type vortex instabilities (KH) (Abdolahpour et al., 2016). Similar investigations regarding the effect of shear instability, by longshore currents at beaches, that modulates the sediment dynamics and current-wave refraction called "'far infragravity" have been reported (Mei and Liu, 1993; Bettess and Bettess, 1982). Furthermore, the understanding of the KH effects by the seagrass-oscillatory flow interaction at the beach is a critical issue to research, in order to analyze if the KH modes are in the infragrativy range.

The KH formation is highly dependent on the wave conditions and canopy properties. The kinematic energy of the instability needs to be strong enough to overcome the viscosity, and the wave period needs to be long enough to generate a shear layer (Ghisalberti and Schlosser, 2013). If these wave and canopy conditions are satisfied, the inflexion point and the Fjϕrtof's conditions (necessary but not sufficient conditions) are present in the oscillatory velocity profile and lead to the KH (Kundu et al., 1990; Drazin and Reid, 2004).

Regarding the KH solution, Py et al. (2004,0) applied the piecewise-linear method to a steady wind-flow velocity profile, coupled to a flexible canopy, finding that the main characteristics of the KH can be well reproduced. Also, Singh et al. (2016) modified the Orr-Sommerfeld equation including the drag effect by the vegetation, finding that the KH modes are similar to those solved by the Rayleigh's equation. Additionally, Zampogna et al. (2016); Luminari et al. (2016) studied the drag-model sensitivity for KH on steady flow-canopy scenarios finding no important differences in the KH modes between viscous and inviscid formulations. And for oscillatory flows, Abdolahpour et al. (2018) used the same Strouhal number proposed by Ho and Huerre (1984) and (Ghisalberti and Nepf, 2002) in steady flows, but this formulation does not take into account its relation with the incoming free surface wave. Thus, solutions to the KH have been developed concluding that there are not relation with fluid viscosity.

In the present work the Pieceswise-linear method is applied to understand the KH modes in oscillatory flow-seagrass interaction. This work aims to develop an analytical model to answer the following questions: does the KH release shorter or longer waves than the incident one in seagrass-oscillatory flow interaction?, and what is the frequency of the KH as a function of the incoming free surface wave frequency?.

The paper is structured as follows; in section 2, a theoretical solution to the KH frequencies by simplifying the vertical profile of a characteristic horizontal velocity in seagrass-oscillatory interaction is developed. In section 3, the theoretical solution is validated and the energy spectra characterized for cases where the turbulent wake is the dominant process and cases where the KH is the dominant. Finally, section 4 concludes the work.

4.2 Kelvin-Helmholtz instability solution

For wave-seagrass interaction the flow can be assumed as a horizontal parallel-shear flow (Cáceres-Euse et al., 2019) and the velocity profile can be decomposed in the mean vertical velocity plus a vertical dependant component by a superposition law see Eq.(4.1),

$$U^{rms}(z) = \overline{U}^{rms} + \tilde{U}(z)^{rms}; \qquad \overline{U}^{rms} = \frac{U_1^{rms} + U_2^{rms}}{2}, \tag{4.1}$$

where U^{rms} is the root mean squared velocity of the oscillatory flow, $\overline{U}^{rms}$ is the uniform velocity, analogous to cases without seagrass; U_1^{rms}, U_2^{rms} are the velocity far above and below the shear layer, and $\tilde{U}(z)^{rms}$ is the velocity produced by the presence of the seagrass (Figure 4.1).

At seagrass-oscillatory flow interaction, the velocity profile varies along the wave period, so to analyze the KH instability it is important to define a characteristic velocity profile that presents the most relevant shape of the flow in the wave period. The characteristic velocity used is $\tilde{U}(z)^{rms}$.

A linear perturbation analysis is performed by defining an instantaneous velocity and pressure as:

$$\begin{aligned} u(x,z,t) &= \tilde{U}(z)^{rms} + u'(x,z,t), \\ w(x,z,t) &= w'(x,z,t), \\ p(x,z,t) &= ct + p'(x,z,t). \end{aligned} \tag{4.2}$$

The instability by $\tilde{U}(z)^{rms}$ can be studied as a temporal stability problem where the perturbation can be formulated as:

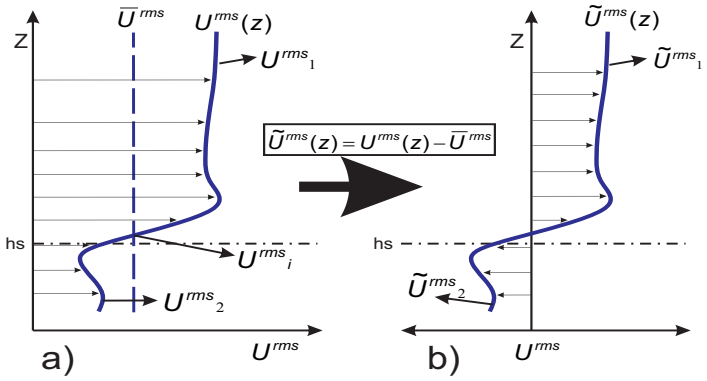

Figure 4.1: Characteristic horizontal velocity profile for wave-seagrass interaction $U^{rms}(z)$ (Panel (a)). $\overline{U}^{rms}$ is the uniform velocity component and $\tilde{U}(z)^{rms}$ is the component as a function of z (Panel (b)). hs is the seagrass height.

$$\begin{aligned} u'(x,z,t) &= \hat{u}(z)e^{i(kx-wt)}, \\ w'(x,z,t) &= \hat{w}(z)e^{i(kx-wt)}, \\ p'(x,z,t) &= \hat{p}(z)e^{i(kx-wt)}, \end{aligned} \tag{4.3}$$

where u', w' and p' are the horizontal and vertical disturbed velocities and pressure respectively, k is a real streamwise wavenumber, ω a complex number where the real part (ω_r) is the frequency of the mode and the imaginary one (ω_i) the growth or decay rate in time, and $c = \omega/k$ the phase speed. Since viscosity does not have any influence on the solution of the unstable modes we will treat it as a dumping term.

Replacing Eq.(4.2) and Eq.(4.3) into the two-dimensional Euler's momentum equation and applying the Squire's transformation (Drazin and Reid, 2004) gives:

$$\begin{aligned} &ik(\tilde{U}^{rms} - c)\hat{u} + D\tilde{U}^{rms}\hat{w} = -ik\hat{p}, \\ &ik(\tilde{U}^{rms} - c)\hat{w} = -D\hat{p}, \\ &ik\hat{u} + D\hat{w} = 0, \qquad D = \frac{d}{dz}. \end{aligned} \tag{4.4}$$

Additionally, defining a stream function as,

$$u' = \frac{\partial \psi'}{\partial z}, \quad w' = -\frac{\partial \psi'}{\partial x}, \quad \text{and} \quad \psi'(\mathrm{x},\mathrm{z},\mathrm{t}) = \phi(\mathrm{z})\mathrm{e}^{\mathrm{i(kx-wt)}}, \tag{4.5}$$

and replacing it into Eq. (4.4) one obtains the Rayleigh's stability equation:

$$(\tilde{U}^{rms} - c)(D^2 - k^2)\phi - \phi D^2 \tilde{U}^{rms} = 0 \tag{4.6}$$

Now, the KH instability arising from the seagrass-flow interaction, can be represented as an unbounded flow problem where the unstable modes can be found solving

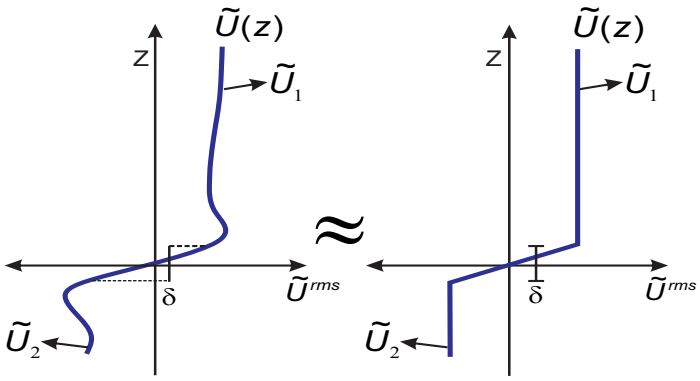

Figure 4.2: Simplification of $\tilde{U}(z)^{rms}$ to a piecewise-linear velocity profile and the definition of the shear layer thickness (δ). $\tilde{U}(z) = \tilde{U}(z)^{rms}$.

the Rayleigh's equation. For unbounded flows it is possible to consider that as z $\rightarrow$ 0 (bottom) or z $\rightarrow$ h (free surface), $\tilde{U}^{rms}$ approaches to a constant value (see Figure 4.1). U_i is the horizontal velocity at the inflexion point approximated to the uniform velocity ($\overline{U}^{rms} \sim U_i$).

4.2.1 Piecewise-linear method on wave-seagrass interaction

The piecewise-linear method simplifies a smoothly varying function by linear segments being linear in the shear layer and constant outside of it (Figure 4.2).

The Rayleigh's equation is solved following Drazin and Reid (2004). We assume that the shear layer, δ in the velocity profile is quasi-symmetric respect to the canopy top and that the inflexion point is located close to the seagrass top ($z_i \sim hs$). As the velocity profile becomes a linear function, $D^2\tilde{U}(z)^{rms} = 0$ and the Rayleigh's equation is:

$$D^2\phi - k^2\phi = 0. \tag{4.7}$$

If $\tilde{U}(z)^{rms}$ agrees with the Rayleigh's inflexion point at z_i and the Fjϕrtof's condition, certain matching conditions have to be satisfied at the discontinuity of $\tilde{U}(z)^{rms}$ and D$\tilde{U}(z)^{rms}$. Moreover on each discotinuity the pressure has to balance $\Delta\hat{p} = 0$ (Drazin and Reid, 2004; Phillips, 2018). This gives the jump conditions:

$$\begin{aligned} &\Delta[(\tilde{U}(z)^{rms} - c)D\phi - D\tilde{U}(z)^{rms}\phi] = 0, \\ &\Delta\left[\frac{\phi}{\tilde{U}(z)^{rms} - c}\right] = 0 \end{aligned} \tag{4.8}$$

where Δ implies the change at the discontinuity. For wave-seagrass interaction problem, locating the inflexion point at the canopy top, the velocity profile can be defined as:

$$\tilde{U}(z) = \begin{cases} \tilde{U}_1^{rms} & \text{for} \quad \mathrm{z} > \dfrac{\delta}{2} \\ 2\dfrac{\tilde{U}_1^{rms}}{\delta} z & \text{for} \quad -\dfrac{\delta}{2} < \mathrm{z} < \dfrac{\delta}{2} \\ \tilde{U}_2^{rms} = -\tilde{U}_1^{rms} & \text{for} \quad \mathrm{z} < -\dfrac{\delta}{2} \end{cases} \tag{4.9}$$

where $\delta \sim 0.2A_w$, and $A_w = \overline{U}^{rms}T/2\pi$ is the horizontal wave excursion length (Cáceres-Euse et al., 2019). Additionally, the corresponding solution to the homogeneous ordinary differential equation Eq.4.7 is:

$$\phi(z) = \begin{cases} \phi^+ = Ae^{-kz} & \text{for} \quad \mathrm{z} > \dfrac{\delta}{2} \\ \phi^0 = Be^{-kz} + Ee^{kz} & \text{for} \quad -\dfrac{\delta}{2} < \mathrm{z} < \dfrac{\delta}{2} \\ \phi^- = De^{kz} & \text{for} \quad \mathrm{z} < -\dfrac{\delta}{2} \end{cases} \tag{4.10}$$

Solution of Eq.4.8 using Eq.4.9 and Eq.4.10 can be formulated as:

$$\begin{bmatrix} e^{k\frac{\delta}{2}}[2k(\tilde{U}_1^{rms} - c) - \dfrac{2\tilde{U}_1^{rms}}{\delta}] & -2\frac{\tilde{U}_1^{rms}}{\delta}e^{-k\frac{\delta}{2}} \\ 2\dfrac{\tilde{U}_1^{rms}}{\delta}e^{-k\frac{\delta}{2}} & e^{k\frac{\delta}{2}}[2k(\tilde{U}_1^{rms} - c) - \frac{2\tilde{U}_1^{rms}}{\delta}] \end{bmatrix} \begin{bmatrix} B \\ E \end{bmatrix} = 0, \tag{4.11}$$

where a non-trivial solution leads to the quadratic dispersion equation for the celerity,

$$c^2 - c(\tilde{U}_1^{rms} + \tilde{U}_2^{rms}) = -\frac{\tilde{U}_1^{rms}}{k\delta}(\tilde{U}_1^{rms} - \tilde{U}_2^{rms}) - \tilde{U}_1^{rms}\tilde{U}_2^{rms} - \frac{(\tilde{U}_1^{rms})^2}{k^2\delta^2}(e^{-2k\delta} - 1) \tag{4.12}$$

The imaginary part of the complex number (c) is:

$$kc_i(k;\delta) = k\tilde{U}_1^{rms}\sqrt{\frac{(k\delta - 1)^2 - e^{-2k\delta}}{k^2\delta^2}} \tag{4.13}$$

while the real part is implying that instability releases a steady wave (Drazin and Reid, 2004).

To solve the Eq.4.13, the dominant modes of the instability are determined in an interval that covers the 50% of the total area of the possible growing modes, centred on the fastest one (see Figure 4.3). These values are between $k\delta = [0.5698 - 1.024]$ or $k = \frac{[0.5698-1.024]}{\delta}$.

Additionally, as $c_r = 0$ for $\tilde{U}^{rms}(z)$, the Kelvin's circulation theorem implies that the instability is advected by the uniform base flow ($\overline{U}^{rms}$), as shown for adverse pressure gradient vortex-types by Cáceres-Euse et al. (2018). This behaviour is supported by experimental data for steady flows, where the instability travels at a speed between

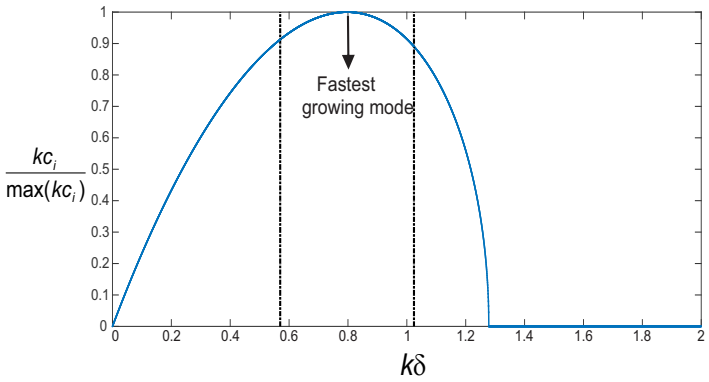

Figure 4.3: Solution to possible unstable modes from the dispersion relation equation (Eq.4.13). The black dashed lines correspond to the inferior and superior limit of the fastest growing mode.

1.0-1.45 times the velocity at the inflexion point (see Figure 4.1-panel a) (Ghisalberti and Nepf, 2002; Mandel et al., 2017). This result presents an apparent "progressive wave" with,

$$f_{KH} = \frac{k\overline{U}^{rms}}{2\pi} \approx [0.09 - 0.16]\frac{\overline{U}^{rms}}{\delta} \tag{4.14}$$

Replacing the value of δ as a function of A_w gives a frequency range for the KH modes:

$$f_{KH} = [2.83 - 5.02]f_w \tag{4.15}$$

where f_w is the free surface wave frequency. Eq. 4.14 is a modified formulation to the existent one for unforced mixing layer by Ho and Huerre (1984), steady currents-seagrass canopy by Ghisalberti and Nepf (2002), and wave-seagrass canopy interaction by Abdolahpour et al. (2018).

4.3 Results

We used the data of Abdolahpour et al. (2016) that correspond to rigid stems in high canopy density. All experiments present KH instabilities for the seagrass-oscillatory flow interaction, based on Keulegan-Carpenter ($KC > 5$) and Reynolds (> 1000) numbers by Ghisalberti and Schlosser (2013) (see Table 4.1). The resultant spectra were estimated by using the Reynolds stress tensor ($u^{'}w^{'}$) time series at three recording positions (see Figure 4.4), in order to capture the turbulent wake scales (nearby the bottom), the KH energy (at the shear layer) and the energy close to the free surface. Initially, a phase-averaged method was applied to the instantaneous horizontal and vertical velocity time series for wave-turbulence decomposition (Lowe et al., 2005; Abdolahpour et al., 2016), where the flow can be decomposed in a steady component (U_c), wave orbital velocity (U_o) and turbulent velocity ($u^{'}$) (Eq4.16).

Run	$T[s]$	$U_\infty[\frac{cm}{s}]$	KC	Re
1	9	3	5.4	1290
3	8	5.6	8.9	3992
6	8	7.7	12.3	7549
11	5	14.9	14.9	17666
12	9	11.3	20.3	18290
17	6	18.8	22.5	33751
19	6	14.3	25.8	44141

Table 4.1: Experiments for rigid stems and high density. U_∞ was estimated for bared bed. From Abdolahpour et al. (2016)

.

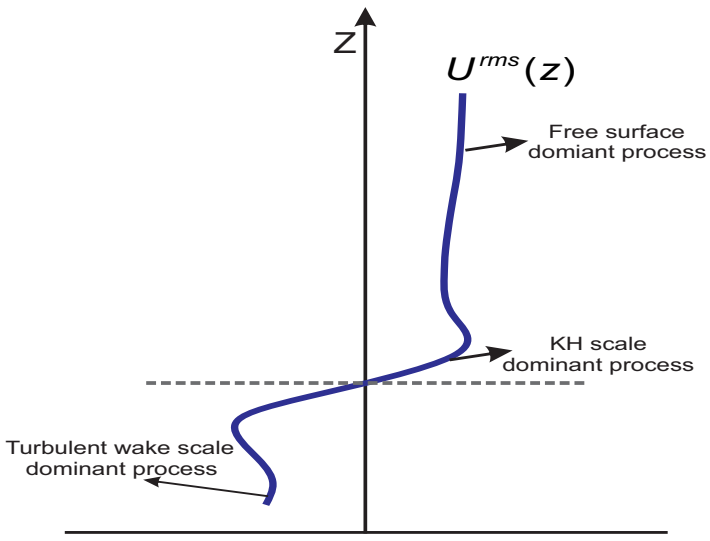

Figure 4.4: The three recording stations in the velocity profile. The gray dashed line is the seagrass top.

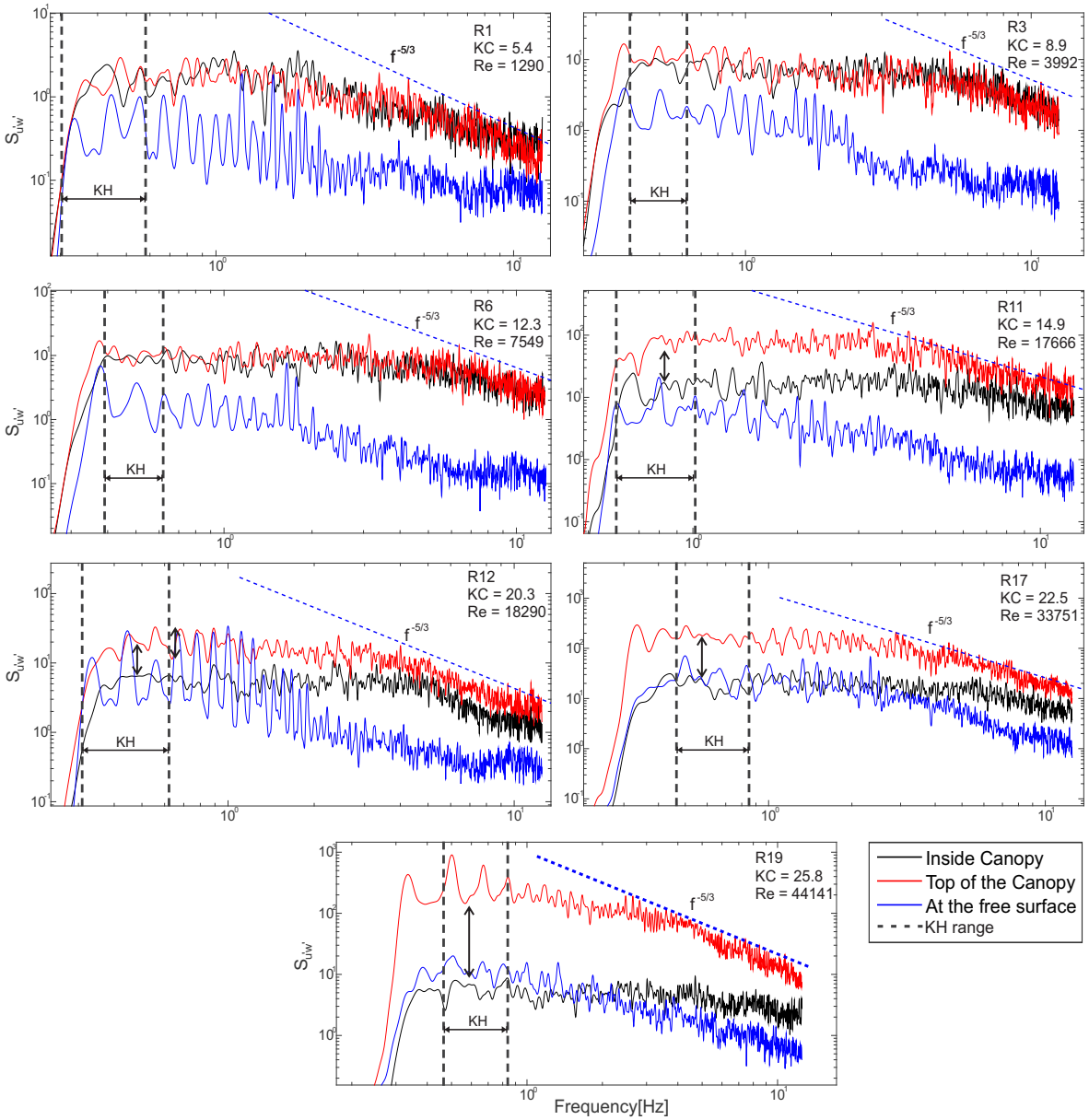

Figure 4.5: Spectra of the vertical velocity averaging using the three recording stations. The KH energy range is indicated by the gray vertical dashed lines and the $f^{-5/3}$ law by blue dashed line.

$$u_i = U_{ci} + U_{oi} + u_i^{'} \tag{4.16}$$

Additionally, a high pass filter was applied to the turbulent components, using a cut-off frequency three times higher than the wave frequency in order to attenuate free surface effects (Abdolahpour et al., 2018). To estimate the energy spectra ($S_{u'w'}$), the Welch's method was applied to the records with 40-s ensemble window with 50% overlap (Mandel et al., 2017) and the energy normalized by the maximum Reynolds stress in the vertical axis (at the canopy top).

Figure 4.5 shows the shear production energy contained at the three recording stations; bottom (black), top of the canopy (red) and free surface (blue). An increment in the energy spectrum inside the dashed black lines (the KH band) is observed for cases R11, R12, R17 and R19 coinciding with Eq. 4.15. Thus, the developed formulation gives information about the band where the KH can be expected; also, the KH frequency is always higher than the free surface wave. For R1, R3 and R6 the differences in the shear production between the bottom and top of the canopy was not observed, even when the criteria by Ghisalberti and Schlosser (2013) was satisfied.

In general, the energy by shear production at the free surface is one order of magnitude smaller than the energy at the top of the canopy, but for cases with $<$7500 and KC $<$12, the energy at the bottom and at the top of the canopy were very close, so it is possible to conclude that the wake production is the dominant process in the system and the KH production is not relevant. For cases with 8000$<<$18000 and 13$<$ KC $<$20, there is an increment in the energy in the KH band, but its magnitude is of the same order of magnitude as the energy close to the bottom, so the KH and wake production can be assumed to be equally important (similar results are reported by Abdolahpour et al. (2016)). For cases with $>$18000 and KC $>$20, there is an increment in the energy at the KH band and the system can be dominated by KH production; additionally, the energy along the whole frequency axis is higher than the energy at the bottom, so part of the energy produced by shear at the KH band is transferred at smaller scales and added to the wake scale production. Additionally, there is a small increment in the energy spectrum at the free surface for R19, and some signature of the KH production can be observed and affects the free surface for high Re, phenomena observed by Mandel et al. (2017) for steady flows.

4.4 Conclusions

By simplifying the vertical profile of a characteristic horizontal velocity in the seagrass-oscillatory flow interaction with a seagrass canopy, and applying the piecewise linear method, it was possible to solve theoretically the KH frequencies. It was found that the KH releases shorter waves than the incident wave with $f_{KH} \approx 4f_w$. The understanding of this process has important implication on beach morphodynamics, since

there is still an open question about the frequency-release mechanisms by seagrasses that affect the beach erosion and sedimentation. For much longer released waves than the incoming free surface wave, it is plausible to assume a permanent current that modifies the sediment distributions, so this mechanism should be analyzed in U_c.

Additionally, $KC > 5$ and > 1000 are not sufficient conditions to assume that the seagrass-oscillatory flow interaction is dominated by the shear production by an inflexion point in the velocity profile, since for $<$7500 and KC $<$12, the turbulent production at the bottom is very close to the turbulence at the top of the canopy, and the wake scale by the presence of the stems seem to be the main turbulent production mechanism. For 8000$<<$18000 and 13$<$ KC $<$20, the wake and KH production are equally important; and for $>$18000 and KC $>$20, the KH production is the dominant process. Additionally, the free surface is affected by the KH energy when $\geq$44000 and KC $\geq$25.

Chapter 5

General Conclusions

5.1 General Conclusions

In this thesis, a theoretical solution to the Kelvin-Helmholtz instability for seagrass-oscillatory flows interaction was developed. The investigation started by analysing the effect of an isolated submerged element, with similar dimensions to a seagrass stem, interacting with a solitary wave. It was possible to conclude that the vortex formation by the adverse pressure gradient can be the dominant turbulent structure, even when the wave breaking is present; additionally, the vortex is transported by the base flow produced by the wave and the Kelvin's circulation theorem is valid for this type of problems.

After analysing the validity of the Kelvin's circulation theorem for this type of problems, a dimensional analysis to the Navier-Stokes equations was performed, in order to determine the relevant terms in seagrass-oscillatory flow interaction; finding that the horizontal pressure gradient and the vertical gradient of the horizontal velocity are the dominant terms in the momentum equation, and a simplified parametrization to the shear layer thickness can be proposed (δ). δ is function of the horizontal orbital excursion value ($\delta \sim 0.2A_w$). This simplified model has important applications on regional to coastal models, since the mathematical expression takes into account the most relevant physical aspects of the problem as a function of the wave properties (wave height and period) and seagrass distribution, and low computational cost.

Finally, it was possible to develop a theoretical solution to the Kelvin-Helmholtz instability by using the assumption that a base flow transports a steady wave released by the instability (Kelvin's circulation theorem). The steady wave was found by linearising the vertical profile by the piecewise linear method and the inclusion of δ in the definition of the simplified horizontal velocity. The solution showed that the shear velocity is the main source of turbulent production when $KC > 14$ and $Re > 17000$ and the wake production is the dominant turbulent production mechanism when $KC < 13$ and $Re < 8000$; additionally, the released Kelvin-Helmholtz frequency is always higher than the free surface wave frequency ($f_{KH} \approx 4f_w$).

As future work, the understanding of long waves released by the seagrass-oscillatory flow interaction is a challenging topic to research, since there is still an open question: If the intensity of steady currents, due to the presence of seagrass in oscillatory flows, is a function of the shear magnitude (Abdolahpour et al., 2018) and wave height decay along the seagrass meadow (Luhar et al., 2010), is the steady current related to a longer released wave than the incident one in charge of affects the morphodynamic of the beaches?, is the steady current related to an infragravity wave?.

References

Abdolahpour, M., Ghisalberti, M., Lavery, P., and Mcmahon, K. (2016). Vertical mixing in coastal canopies. *Limnology and Oceanography*.

Abdolahpour, M., Ghisalberti, M., McMahon, K., and Lavery, P. S. (2018). The impact of flexibility on flow, turbulence, and vertical mixing in coastal canopies. *Limnology and Oceanography*.

Abdolahpour, M., Hambleton, M., and Ghisalberti, M. (2017). The wave-driven current in coastal canopies. *Journal of Geophysical Research: Oceans*.

Amini Afshar, M. (2010). Numerical wave generation in openfoam.

Anderson, M. E. and Smith, J. M. (2014). Wave attenuation by flexible, idealized salt marsh vegetation. *Coastal Engineering*.

Bettess, P. and Bettess, J. A. (1982). A generalization of the radiation stress tensor. *Applied Mathematical Modelling*, 6:146–150.

Bradley, K. and Houser, C. (2009). Relative velocity of seagrass blades: Implications for wave attenuation in low-energy environments. *Journal of Geophysical Research: Earth Surface*.

Bricker, J. D. and Monismith, S. G. (2007). Spectral wave-turbulence decomposition. *Journal of Atmospheric and Oceanic Technology*, 24.

Cáceres-Euse, A., Toro-Botero, F. M., Orfila-Foster, A., and Osorio-Arias, A. (2018). Vortex formation in wave-submerged structure interaction. *Ocean Engineering*, 166:47–63.

Cáceres-Euse, A., Variano, E. A., Toro-Botero, F., Gómez-Giraldo, A., and Osorio, A. (2019). Simplified approach to oscillatory flow-submerged canopy (submitted). *Experiments in Fluids*.

Chang, K.-A., Hsu, T.-J., and Liu, P. L.-F. (2001). Vortex generation and evolution in water waves propagating over a submerged rectangular obstacle Part I. Solitary waves. *Coastal Engineering*, 52:257–283.

Chang, K.-A., Hsu, T.-J., and Liu, P. L.-F. (2005). Vortex generation and evolution in water waves propagating over a submerged rectangular obstacle. Part II: Cnoidal waves. *Coastal Engineering*, 52:257–283.

Chanson, H., Trevethan, M., and Aoki, S. I. (2008). Acoustic Doppler velocimetry (ADV) in small estuary: Field experience and signal post-processing. *Flow Measurement and Instrumentation*, 19:307–313.

Chen, L., Zang, J., Hillis, A., Morgan, G., and Plummer, A. (2014). Numerical investigation of wavestructure interaction using OpenFOAM. *Ocean Engineering*, 71:91–109.

Chen, Y.-L. and Hsiao, S.-C. (2016). Generation of 3D water waves using mass source wavemaker applied to Navier-Stokes model. *Coastal Engineering*, 109:76–95.

Christou, M., Swan, C., and Gudmestad, O. (2008). "the interaction of surface water waves with submerged breakwaters". *Coastal Engineering*, 55:945–958.

Cooker, M., Peregrine, D., Vidal, C., and Dold, J. (1990). The interaction between a solitary wave and a submerged semicircular cylinder. *Journal of Fluid Mechanics*, 215:1–22.

Dean, R. G. and Dalrymple, R. A. (1991). *Water Wave Mechanics for Engineers and Scientists*. Prentice-Hall.

Dingemnas, M. (1993). Comparison of computations with Boussinesq-like models and laboratory measurements.

Dong, C. M. and Huang, C. J. (2001). On a 2-D Numerical Wave Tank in Viscous Fluid. *International Offshore and Polar Engineering Conference*, Ill:1098–6189.

Drazin, P. and Reid, W. (2004). *Hydrodynamic Stability*.

E., L. and Hoekstra, M. (2008). Testing Uncertainty Estimation and Validation Procedures in the Flow Around a Backward Facing Step. *3rd Workshop on CFD Uncertainty Analysis, Lisbon*.

Elangovan, M. and Sahoo, G. (2010). Generation of Irregular Wave for Marine Application by Piston Type Wave Maker. *Proceedings of the Twentieth International Offshore and Polar Engineering Conference*, 7:556–571.

Ferziger, J. H. and Peric, M. (2002). *Computational Methods for Fluid Dynamics*. Springer.

Finnigan, J. (2000). Turbulence in PLant Canopies. *Annual Review of Fluid Mechanics*, pages 519–571.

Fletcher, C. A. (1987). *Computational Techniques for Fluid Dynamics Volume II*.

Foster-Martinez, M. R., LLacy, J. R., Ferner, M. C., and Variano, E. A. (2018). Wave attenuation across a tidal marsh in San Francisco Bay. *Coastal Engineering*, 136:26–40.

Frigaard, P., Hogedal, M., and Chistensen, M. (1993). Wave generation theory.

Galan, A., Simarro, G., Orla, A., Simarro, J., and Liu, P. L.-F. (2013). A FULLY NONLINEAR MODEL FOR WATER WAVE PROPAGATION FROM DEEP TO SHALLOW WATERS. *Journal of Waterway Port Coastal and Ocean Engineering*, pages 362–371.

Ghisalberti, M. and Nepf, H. (2002). Mixing layers and coherent structures in vegetated aquatic flows. *Journal Of Geophysical Research*, 107.

Ghisalberti, M. and Nepf, H. (2004). The limited growth of vegetated shear layers. *Water Resources Research*, 40.

Ghisalberti, M. and Nepf, H. (2009). Shallow flows over a permeable medium: The hydrodynamics of submerged aquatic canopies. *Transport in Porous Media*, 40.

Ghisalberti, M. and Schlosser, T. (2013). Vortex generation in oscillatory canopy flow. *Journal of Geophysical Research: Oceans*, 118:1534–1542.

Goring, D. and Raichlen, F. (1980). The Generation Of Long Waves In The Laboratory. *Coastal Engineering Proceedings*, 1(17):430–443.

Goring, D. G. and Nikora, V. I. (2002). Despiking Acoustic Doppler Velocimeter Data. *Journal of Hydraulic Engineering*, 128:117–126.

Greenshields, C. J. (2015). *OpenFOAM - The Open Source CFD Toolbox - User Guide*.

Grue, J. (1992). Nonlinear water waves at a submerged obstacle or bottom topography. *Journal of Fluid Mechanics*, 244:455–476.

Hedges, T. (1995). Regions of validity of analytical wave theories. *Proc. Inst. Civ. Engnrs., Water, Marine and Energy*, 112:111–114.

Hellsten, A. (1998). Some improvements in Menter's k-omega SST turbulence model. *29th AIAA, Fluid Dynamics Conference*, pages 1–11.

Higuera, P., Lara, J. L., and Losada, I. J. (2013). Realistic wave generation and active wave absorption for NavierStokes models Application to OpenFOAM. *Coastal Engineering*, 71:102–118.

Higuera, P., Losada, ., and Lara, J. (2015). Three-dimensional numerical wave generation with moving boundaries. *Coastal Engineering*, 101:35–47.

Hirt, C. and Nichols, B. (1981). Volume of fluid (VOF) method for the dynamics of free boundaries. *Journal of computational physics*, 39(1):201–225.

Ho, C.-M. and Huerre, P. (1984). Perturbed Free Shear Layers. *Annual Review of Fluid Mechanics*, 16.

Huang, C.-J. and Dong, C.-M. (1999). Wave deformation and vortex generation in water waves propagating over a submerged dike. *Coastal Engineering*, 37:123–148.

Iwata, K., Kawasaki, K., and Do-Sam, K. (1996). Breaking limit, breaking and post-breaking wave deformation due to submerged structures. *Coastal Engineering*, 231.

Jacobsen, N. G., Fuhrman, D. R., and Fredse, J. (2012). A wave generation toolbox for the open-source CFD library: OpenFoam. *International journal for numerical methods in fluids*, 70.

Jasak, H. (2009). Dynamic Mesh Handling in OpenFOAM. *47th AIAA Aerospace Sciences Meeting including The New Horizons Forum and Aerospace Exposition*, pages 1–10.

Jasak, H. and Tukovic, Z. (2006). "automatic mesh motion for the unstructured finite volume method". *Transactions of Famena*, 30(2):1–20.

Jasak, H. and Tukovic, Z. (2010). Dynamic mesh handling in OpenFOAM applied to fluid-structure interaction simulations. *European Conference on Computational Fluid Dynamics*, pages 1–19.

Jasak, H., Weller, H. G., and Gosman, A. D. (1999). High resolution NVD differencing scheme for arbitrarily unstructured meshes. *International Journal for Numerical Methods in Fluids*, 31(2):431–449.

Jensen, B. L., Sumer, B. M., and Fredsoe, J. (1989). Turbulent oscillatory boundary layers at high Reynolds numbers. *Journal of Fluid Mechanics*, 206:265–297.

Karambas, T., Koftis, T., and Prinos, P. (2015). Modeling of Nonlinear Wave Attenuation due to Vegetation. *Journal of Coastal Research*.

Katell, G. and Eric, B. (2002). Accuracy of solitary wave generation by a piston wave maker. *Journal of Hydraulic Research*, 40(3):321–331.

Kawasaki, K. and Iwata, K. (1998). Numerical Analysis of Wave Breaking Due To Submerged Breakewater in three-dimensional wave field. *Coastal Engineering*, 231.

Keulegan, G. H. (1948). Gradual damping of solitary waves. *Nat. Bur. Sci. J. Res*, 40:487–498.

Keulegan, G. H. and Carpenter, L. H. (1958). Forces on Cylinders and Plates in an Oscillating Fluid. *Journal of Waterway Port Coastal and Ocean Engineering-ASCE*, 60:423–440.

King, A. T., Tinoco, R. O., and Cowen, E. A. (2012). A k- turbulence model based on the scales of vertical shear and stem wakes valid for emergent and submerged vegetated flows. *Journal of Fluid Mechanics*, 701:1–39.

Kobayashi, N., Raichle, A. W., and Asano, T. (1993). Wave attenuation by vegetation. *Journal of Waterway Port Coastal and Ocean Engineering-ASCE*, 119:30–48.

Koftis, T., Prinos, P., and Stratigaki, V. (2013). Wave damping over artificial Posidonia oceanica meadow: A large-scale experimental study. *Coastal Engineering*.

Kundu, P., Cohen, I., and Dowling, D. (1990). *Fluid Mechanics*.

Lambert, R. J. (2012). Development of a numerical wave tank using openfoam.

Lara, J. L., Garcia, N., and Losada, I. J. (2006). RANS modelling applied to random wave interaction with submerged permeable structures. *Coastal Engineering*, 53:395+417.

Lei, J. and Nepf, H. M. (2019). Wave damping by flexible vegetation: connecting individual blade dynamics to the 1meadow scale. *Coastal Engineering*.

Lin, P. and Liu, P. (1999). Internal wave-maker for Navier-Stokes equations models. *Journal of waterway port coastal and ocean engineering*, 3.

Liu, P. L. F. and Orfila, A. (2005). Viscous effects on transient long-wave propagation. *Journal of Fluid Mechanics*, 537:443–443.

Liu, P. L. F., Simarro, G., Vandever, J., and Orfila, A. (2006). Experimental and numerical investigation of viscous effects on solitary wave propagation in a wave tank. *Coastal Engineering*, 53:181–190.

Losada, I. J., Maza, M., and Lara, J. L. (2016). A new formulation for vegetation-induced damping under combined waves and currents. *Coastal Engineering*.

Losada, I. J., Silva, R., and Losada, M. (1996). 3-D non-breaking regular wave interaction with submerged breakwaters. *Coastal Engineering*, pages 229–248.

Lowe, R., Koseff, J., and Stephen, M. (2005). Oscillatory flow through submerged canopies: 1. Velocity structure. *Journal of Geophysical Research*, 110.

Luhar, M., Coutu, S., Infantes, E., Fox, S., and Nepf, H. M. (2010). Wave induced velocities inside a model seagrass bed. *Journal of Geophysical Research*.

Luhar, M., Infantes, E., and Nepf, H. (2017). Seagrass blade motion under waves and its impact on wave decay. *Journal of Geophysical Research: Oceans*.

Luhar, M. and Nepf, H. M. (2013). From the blade scale to the reach scale: A characterization of aquatic vegetative drag. *Advances in Water Resources*.

Luhar, M. and Nepf, H. M. (2016). Wave-induced dynamics of flexible blades. *Journal of Fluids and Structures*.

Luminari, N., Airiau, C., and Bottaro, A. (2016). Drag-model sensitivity of Kelvin-Helmholtz waves in canopy flows. *Physics of Fluids*.

Mandel, T. L., Rosenzweig, ., Chung, H., Ouellette, N. T., and Koseff, J. R. (2017). Characterizing free-surface expressions of flow instabilities by tracking submerged features. *Experiments in Fluids*.

Marion, A., Nikora, V., Puijalon, S., Bouma, T., Koll, K. B., Tait, S. J., Zaramella, M., Sukhodolov, A., O'Hare, M., Wharton, G., Aberle, J., Tregnaghi, M., Davies, P., Nepf, H., Parker, G., and Statzner, B. (2014). Aquatic interfaces: a hydrodynamic and ecological perspective. *Journal of Hydraulic Research*, 52:744–758.

Maxwell, P. S., Eklf, J. S., van Katwijk, M. M., O'Brien, K. R., de la Torre-Castro, M., Bostrm, C., Bouma, T. J., Krause-Jensen, D., Unsworth, R. K., van Tussenbroek, B. I., and van der Heide, T. (2017). The fundamental role of ecological feedback mechanisms for the adaptive management of seagrass ecosystems a review. *Biological Reviews*, 92.

Mei, C. C. and Liu, P. L.-F. (1993). Surface Waves and Coastal Dynamics. *Annual Review of Fluid Mechanics*, 25:215–240.

Méndez, F., Losada, I., and Losada, M. A. (1999). Hydrodynamics induced by wind waves in a vegetation field. *Journal of Geophysical Research*, 104.

Nejadkazem, O. and Gharabaghi, A. (2008). A survey of passive wave absorbers. *4th National Conference on Civil Engineering*, 24.

Nepf, H. (2013). Hydrodynamics of vegetated channels. *Journal of Hydraulic Research*, pages 37–41.

Nepf, H. M. (2012). Flow and Transport in Regions with Aquatic Vegetation. *Annual Review of Fluid Mechanics*.

Ohyama, T. and Nadaoka, K. (1991). Development of a numerical wave tank for analysis of nonlinear and irregular wave field. *Fluid dynamics research*, 231.

Oliveira, T., Gironella, F., Sanchez-Arcilla, A., Sierra, J., and Celigueta, M. (2009). Nonlinear Regular Wave Generation in Numerical and Physical Flumes. *Journal of Coastal Research*, 56:1025–1029.

Ondiviela, B., Losada, I. J., Lara, J. L., Maza, M., Galvn, C., Bouma, T. J., and van Belzen, J. (2014). The role of seagrasses in coastal protection in a changing climate. *Coastal Engineering*.

Phillips, M. (2018). Hydrodynamic of Instability Class notes. *University of California, Berkeley*.

Pinsky, M. L., Guannel, G., and Arkema, K. K. (2013). Quantifying wave attenuation to inform coastal habitat conservation. *Ecosphere*, 4.

Pujol, D., Serra, T., Colomer, J., and Casamitjana, X. (2013). Flow structure in canopy models dominated by progressive waves. *Journal of Hydrology*, 486:281–292.

Py, C., De Langre, E., and Moulia, B. (2004). The mixing layer instability of wind over a flexible crop canopy. *Comptes Rendus - Mecanique*, 332.

Py, C., De Langre, E., and Moulia, B. (2006). A frequency lock-in mechanism in the interaction between wind and crop canopies. *Journal of Fluid Mechanics*, 568.

Raupach, M. R., Finnigan, J. J., and Brunet, Y. (1996). Coherent Eddies and Turbulence in vegetation Canopies. *Boundary-layer Meteorology*, 78.

Raupach, M. R. and Shaw, R. H. (1982). Averaging procedures for flow within vegetation canopies. *Boundary-layer Meteorology*, 22.

Rodi, W. (1993). Turbulence Models and Their Applications in Hydraulics: A State of the Art Review.

Rusello, P. J., Lohrmann, A., Siegel, E., and Maddux, T. (2006). Improvements in Acoustic Doppler Velocimetery. *Conference on Hydroscience and Engineering*, 261:1–16.

Sana, A. and Tanaka, H. (2007). Full-range equation for wave boundary layer thickness. *Coastal Engineering*, 54:639–642.

Schanz, A. and Asmus, H. (2003). Impact of hydrodynamics on development and morphology of intertidal seagrasses in the Wadden Sea. *Marine Ecology Progress Series*, 261:123–134.

Schanz, A., Polte, P., and Asmus, H. (2002). Cascading effects of hydrodynamics on an epiphyte-grazer system in intertidal seagrass beds of the Wadden Sea. *Marine Biology*, 141:287–297.

Shen, L. and Chan, E.-S. (2008). Numerical simulation of fluidstructure interaction using a combined volume of fluid and immersed boundary method. *Ocean Engineering*, 35:939–952.

Singh, K. and Xie, M. (2003). Bootstrap: A Statistical Method.

Singh, R., Bandi, M. M., Mahadevan, A., and Mandre, S. (2016). Linear stability analysis for monami in a submerged seagrass bed. *Journal of Fluid Mechanics*.

Spalding, D. B. (1961). A Single Formula for the Law of the Wall. *Journal of Applied Mechanics*, pages 445–457.

Steven A., H. (1993). *Physical Models and Laboratory Techniques in Coastal Engineering*. World Scientific Publishing.

Stratigaki, V., Manca, E., Prinos, P., Losada, I. J., Lara, J. L., Sclavo, M., Amos, C. L., Caceres, I., and Sanchez-Arcilla, A. (2011). Large-scale experiments on wave propagation over Posidonia oceanica. *Journal of Hydraulic Research*.

Tanino, Y. and Nepf, H. (2008). Laboratory Investigation of Mean Drag in a Random Array of Rigid, Emergent Cylinders. *Journal of Hydraulic Engineering*.

Tinoco, R. O. and Coco, G. (2018). Turbulence as the Main Driver of Resuspension in Oscillatory Flow Through Vegetation. *Journal of Geophysical Research: Earth Surface*.

Van Der Heide, T., Van Nes, E. H., Geerling, G. W., Smolders, A. J. P., Bouma, T. J., and Van Katwijk, M. M. (2007). Positive feedbacks in seagrass ecosystems: Implications for success in conservation and restoration. *Ecosystems*.

Versteeg, H. K. and Malalasekera, W. (2007). *An Introduction to Computational Fluid Dynamics. Segunda ed.*

Weller, H. G., Tabor, G., Jasak, H., and Fureby, C. (1998). A tensorial approach to computational continuum mechanics using object-oriented techniques. *Computers in Physics*, 12(6):620–631.

Wilcox, D. C. (2006). *Turbulence Modeling for CFD Third Edition*.

Willmott, C. J. and Matsuura, K. (2005). Advantages of the mean absolute error (MAE) over the root mean square error (RMSE) in assessing average model performance. *Climate Research*, 30:79–82.

Wu, N. J., Hsiao, S. C., Chen, H. H., and Yang, R. Y. (2016). The study on solitary waves generated by a piston-type wave maker. *Ocean Engineering*, 117:114–129.

Wu, N.-J., Tsay, T.-K., and Chen, Y.-Y. (2014). Generation of stable solitary waves by a piston-type wavemaker. *Wave Motion*, 51:240–255.

Wu, Y.-T., Shih-Chun, H., Zhi-Cheng, H., and Kao-Shu, H. (2012). Propagation of solitary waves over a bottom-mounted barrier. *Coastal Engineering*, 62:31–47.

Xi-zeng, Z., Chang-hong, H., and Zhao-chen, S. (2010). Numerical simulation of extreme wave generation using VOF method. *Journal of Hydrodynamics*, 22:466–477.

Zampogna, G. A., Pluvinage, F., Kourta, A., and Bottaro, A. (2016). Vertical mixing in coastal canopies. *Water Resources Research*.

Zeller, R. B., Zarama, F. J., Weitzman, J. S., and Koseff, J. R. (2015). A simple and practical model for combined wave-current canopy flows. *Journal of Fluid Mechanics*, 767.

Zhang, J., Zheng, J., Jeng, D.-S., and Wang, G. (2012). Numerical Simulation of Solitary Wave Induced Flow Motion around a Permeable Submerged Breakwater. *Journal of Applied Mathematics*, pages 1–14.

Zhang, Y., Tang, C., and Nepf, H. (2018). Turbulent Kinetic Energy in Submerged Model Canopies Under Oscillatory Flow. *Water Resources Research*.

Zhou, Q., Zhang, J.-M., and Li, Y. (2014). Numerical Study of Interaction between Solitary Wave and Two Submerged Obstacles in Tandem. *Journal of Coastal Research*, 30(5):975–992.